CR 137534

AVAILABLE TO THE PUBLIC

D210-10792-1

September 1974

INVESTIGATION OF ROTOR BLADE ELEMENT AIRLOADS FOR A TEETERING ROTOR IN THE BLADE STALL REGIME

By

L. U. Dadone
T. Fukushima

Prepared under Contract NAS2-7229 by
The Boeing Vertol Company
Boeing Center, P.O. Box 16858
Philadelphia, Pennsylvania 19142

for

NATIONAL AERONAUTICS AND SPACE ADMINISTRATION

NASA CR-137534

INVESTIGATION OF ROTOR BLADE ELEMENT AIRLOADS FOR A TEETERING ROTOR IN THE BLADE STALL REGIME

By

L. U. Dadone
T. Fukushima

SEPTEMBER 1974

Prepared under Contract NAS2-7229 by

THE BOEING VERTOL COMPANY

Boeing Center, P.O. Box 16858

Philadelphia, Pennsylvania 19142

For

U.S. ARMY AIR MOBILITY RESEARCH AND DEVELOPMENT LABORATORY

Ames Research Center

Moffett Field, California

and

NATIONAL AERONAUTICS AND SPACE ADMINISTRATION

SUMMARY

A test program has been conducted in the NASA-Ames 7 x 10 ft. low speed Wind Tunnel on a seven foot diameter model of a teetering rotor. Objectives of the test were:

1. To verify the validity of data obtained for a similar full scale rotor model previously tested in the NASA-Ames 40 x 80 ft. Wind Tunnel.

2. Provide a basis for comparison with blade element airloads measured on an articulated model rotor.

3. Provide insight into blade element airloads at flight conditions of particular interest in understanding retreating blade stall.

In addition, a study was conducted to evaluate current rotor performance prediction methodology through the computer simulation of selected teetering rotor test conditions.

The present model rotor test showed that in the full scale Bell test the data was influenced by pressure transducer acceleration loads which could not be separated from the airloads, so that the Bell data is invalid.

The comparison with the articulated rotor data showed the teetering rotor to be subjected to less extensive flow separation, over the 0.75R span station, at similar rotor lift levels. At that station the teetering rotor also experienced considerably reduced excursions in loads and angle of attack.

A review of the detailed events during retreating blade stall showed that stall, under the influence of unsteady aerodynamic effects, can consist of as many as four separate stall events, each associated with a vortex shed from the leading edge and sweeping over the upper surface of the rotor blade.

A detailed study of integrated loads was possible only under a limited number of conditions because instrumentation malfunctions generally precluded the computation on such loads.

A number of test conditions was also simulated by means of current rotor performance prediction methods. The simulation showed that more knowledge is necessary of unsteady aerodynamic effects at model rotor Reynolds Numbers.

TABLE OF CONTENTS

LIST OF ILLUSTRATIONS

LIST OF TABLES

LIST OF SYMBOLS

a	Lift curve slope	Radian $^{-1}$
b	Number of blades	
c	Blade chord	
C_l	Blade element lift coefficient, $\frac{\text{Lift}}{qc}$	
C_m	Blade element pitching moment coefficient about the quarter chord, $\frac{\text{Moment}}{qc^2}$	
C_n	Blade element normal force coefficient, $\frac{\text{Normal Force}}{qc}$	
C_p	Pressure coefficient, p/q	
C_T/σ	Rotor thrust coefficient	
C_T'/σ	Rotor lift coefficient	
D	Rotor diameter	feet
k	Reduced frequency parameter $\frac{c\Omega}{2V}$	
M	Mach Number	
P	Rotor power	HP
p	Measured pressure	lb/in^2
q	Dynamic pressure, $\frac{1}{2}\rho V^2$	lb/ft^2
r	Blade radial station	feet
R	Blade radius	feet
Re	Reynolds Number based on chord $\frac{cV}{\nu}$	

U_p	Total of velocity components perpendicular to rotor disc plane at a blade station	feet/sec
V	Free stream velocity	feet/sec
V_T	Rotor tip speed	feet/sec
x	Blade element chordwise location measured from leading edge	in
X	Rotor propulsive force	pounds
$\overline{X}$	Rotor propulsive force coefficient, $X/qd^2\sigma$	
y	Blade element surface location measured perpendicular to chord line	feet
μ	Advance ratio, V/V_T	
α	Blade element angle of attack	degrees
α_{ME}	Angle of attack calculated from $(C_N-C_{N_O})/d_{C_N}/d\alpha)$	degrees
α_s	Rotor shaft angle	degrees
α_{TPP}	Rotor tip path plane angle $\alpha_s - \beta_{ic}$	degrees
β	Blade flapping angle	degrees
β_{ic}	Cosine component of blade flapping angle	degrees
β_{ic}	Sine component of blade flapping angle	degrees
θ_0	Blade collective pitch at center-line of rotation	degrees
$\theta_{.75R}$	Blade collective pitch at 75 percent radius	degrees

λ	Rotor inflow ratio	
ρ	Density of air	slugs/ft^3
σ	Rotor solidity, $\frac{bc}{\pi R}$	
υ	Kinematic Viscosity	ft^2/sec
Ψ	Blade azimuth angle	degrees
Ω	Rotor Speed	Rad/Sec

INTRODUCTION

The true nature of the dynamic stall over a helicopter rotor blade in forward flight remains, for the time being, one of the least understood subjects in aerodynamics. At present the problem is being approached from many different directions, ranging from theoretical studies to oscillating airfoil tests and rotor tests. In the near future, hopefully, all this work will be combined to generate a complete picture of the role of unsteady aerodynamic effects on helicopter rotor blades, thus providing the designer with a much needed design tool.

The necessity for this test program followed from questions raised as a result of the articulated rotor test in Reference 2 and the full scale teetering rotor test in Reference 3. This test has answered some of those questions and has pointed out areas which should be explored in following investigations.

This test program was conducted under the direction of G. Morehouse, Research Scientist at the Ames Directorate, U.S. Army Air Mobility Research and Development Laboratory. Dr. J. McCroskey, of the Ames Directorate, and F. Harris from the Boeing Vertol Company, provided guidance during the test. R. George, of the Ames Directorate, was responsible for instrumentation and data acquisition. J. McMullen of The Boeing Vertol Company, carried out the bulk of the data reduction and W. Capron, also at Boeing Vertol, conducted the theoretical performance prediction calculations.

1.0 TEST EQUIPMENT

1.1 Wind Tunnel

The test was conducted in the 7 x 10 ft. (2.13 x 3.05 m) low speed wind tunnel at NASA-Ames, Moffett Field, California. This tunnel is of the closed-circuit single return type, with a rectangular test section equipped with solid walls. Maximum wind tunnel speed is approximately 400 fps (122 m/sec).

1.2 Rotor Test Setup

The rotor test stand used in this test consists of a hub and a pylon mounted on a turntable. The turntable itself rests on a six component balance system. Rotor drive and slip ring assembly are located below the turntable floor. The pylon can be inclined from 0° forward to 25° by remote control.

The hub has been simplified by eliminating cyclic pitch controls, but there are provisions for remotely controlling the collective pitch.

The blades are set with a pre-cone angle of 1.5°. Blade flapping is measured at the center of rotation by means of a gear and potentiometer arrangement, and the pitch links are equipped with strain gauges to measure pitch link loads.

The model rotor in the test section is shown in Figure 1. Details of the rotor hub are shown in Figure 2.

1.3 Rotor

The rotor is a reduced scale version of the modified UH-1D rotor tested in the Ames 40 x 80 ft. wind tunnel as described in Reference 3. The basic data for the blades in this test is:

Airfoil designation	NACA 0012
Chord	4.25 in (10.8 cm)
Number of blades	2
Diameter	7.0 ft (2.13 m)
Twist	0°
Pre-cone angle	1.5°
Root cutout, r/R	0.119
Solidity	0.0644
Taper Ratio	1:1
Blade Lock No.(for one blade)	3.3
Location of pressure instrumentation, r/R	0.75

1.4 Surface Static Pressures

One of the rotor blades was equipped with 16 absolute static pressure transducers distributed along the 0.75 R span station. Table I describes the transducer assignment and how the transducers functioned during the test.

The transducers used in this test were KULITE Model LQL4-125-25. Their operating range was 0-20 psi, and their sensitivity was repeatedly checked out in the 0-4 psi range before and during the test. No change in sensitivity was detected. Figures 3 and 4 illustrate transducer installation.

1.5 Data Acquisition System

The data acquisition system at the test site was equipped to handle 28 channels of data, but since the data recording system was limited to one 14-track recorder, data acquisition was broken into two consecutive periods. Table II shows the complete channel assignment and the recording sequence. The data acquisition system is also illustrated in Figure 5.

During a test run one channel of data at a time from each of the two recording sequences could be monitored on oscilloscopes. All channels could also be simultaneously displayed on-line on an oscillograph, but sample oscillograph strip-outs were produced only after each run, or series of runs, by playing back the data tape.

The balance system to measure rotor performance was completely independent of the pressure data acquisition system. Balance data, rotor controls, tunnel conditions, and atmospheric conditions were recorded separately. A direct link between the wind tunnel control room and an IBM 1800 computer provided a rapid evaluation of the rotor performance parameters from the combined balance, rotor, and wind tunnel information.

For each test point, two thirty-second records of data were made, one for each recording phase. Rotor performance data was taken before, during, and after recording to assure stable flight conditions.

1.6 Data Reduction System

The pressure data and other information recorded on the 14-channel analog tapes, as described in the previous section, were transferred to the Boeing Vertol Company for processing

1.6 Data Reduction System (Cont'd)

through a system similar to the Boeing Vertol flight test data reduction system.

From each test point sequence a record of five consecutive cycles was selected for processing. Each record was first digitized with a sampling rate of forty-five (45) points per cycle and then processed through a series of computer programs. The steps involved in this process, ranging from a conversion into engineering units, through harmonic analysis (twelve harmonics), averaging and final processing into non-dimensional parameters, are outlined in Figure 6.

The equations and assumptions used in data reduction are listed in the Appendix.

Finally, reduced data in tabular form and selected systematic plots of final data are presented in Volume II of this report.

TABLE I - TRANSDUCER ASSIGNMENT AND CONDITION DURING TEST

Transducer Number	Chord Station (x/c)	Surface	Recording Phase	Condition
1	.05	Upper	A	Out After T.P. 18.11
2	.10		A	
3	.15		A	
4	.20		A	
5	.30		A	
6	.40		B	
7	.50		A	Very Poor After T.P. 14.13
8	.60		A	
9	.70		B	
10	.80		A	
11	.50	Lower	B	Inoperative at Start of Test
12	.30		B	
13	.20		B	
14	.15		B	Very Poor After T.P. 14.13
15	.10		B	Out After T.P. 14.13
16	.05		B	Inoperative at Start of Test

TABLE II TAPE RECORDER CHANNEL ASSIGNMENT AND RECORDING SEQUENCE

CHANNEL NO.	RECORDING PHASE A	RECORDING PHASE B
1	TR 1	TR 9
2	TR 2	TR 11
3	TR 3	TR 6
4	TR 4	TR 12
5	TR 5	TR 13
6	TR 7	TR 14
7	TR 8	TR 15
8	TIME CODE	
9	TR 10	TR 16
10	ROOT FLAPPING ANGLE	
11	PITCH LINK LOADS	
12	RPM	
13	TIME CODE-FM	
14	VOICE ID	+1 VOLT D.C.
EDGE	VOICE ID	

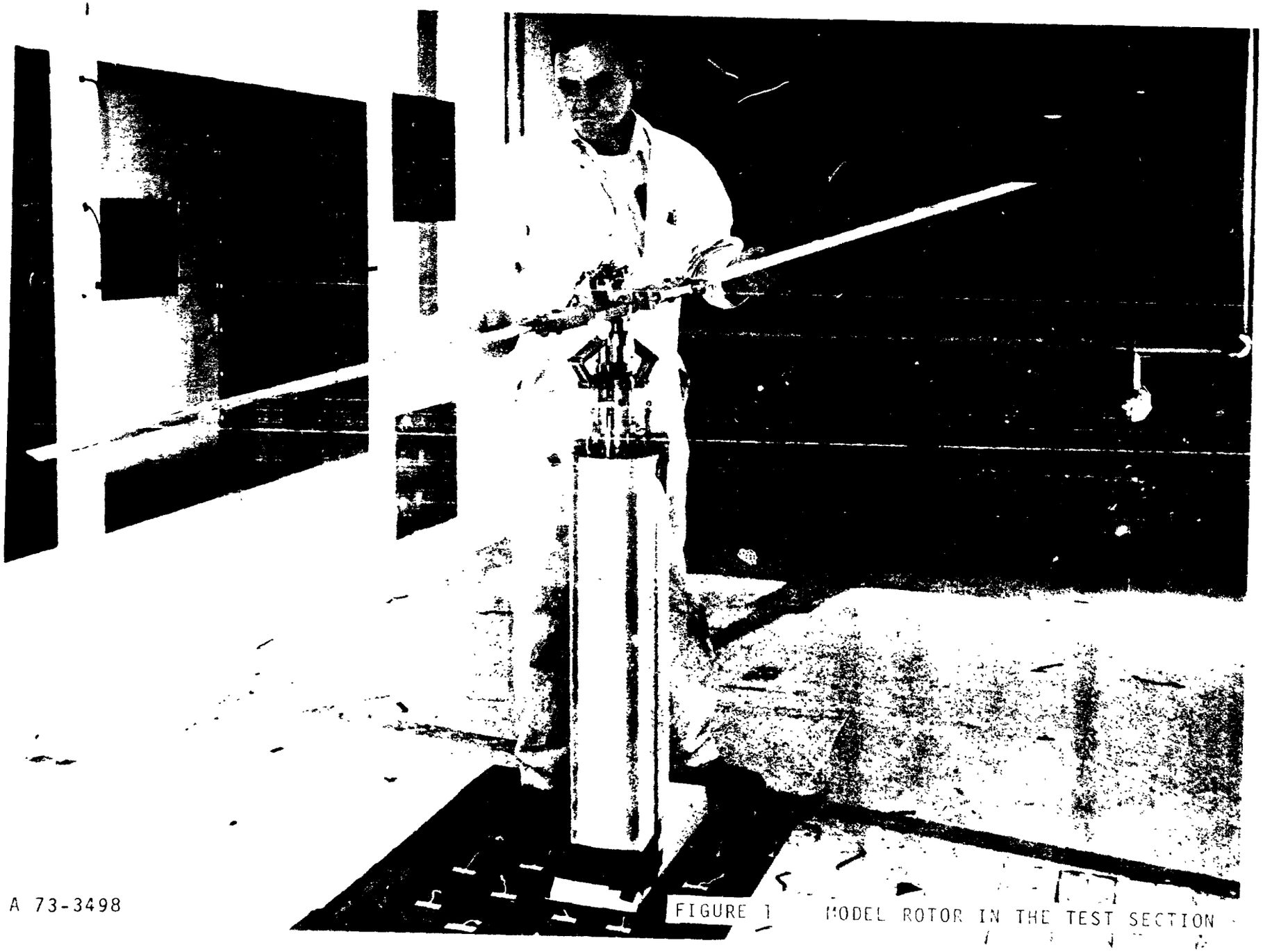

A 73-3498

FIGURE 1 MODEL ROTOR IN THE TEST SECTION

SPAN STATION: .75R
PROFILE: NACA 0012
TRANSDUCERS: KULITE LQL4-125-25

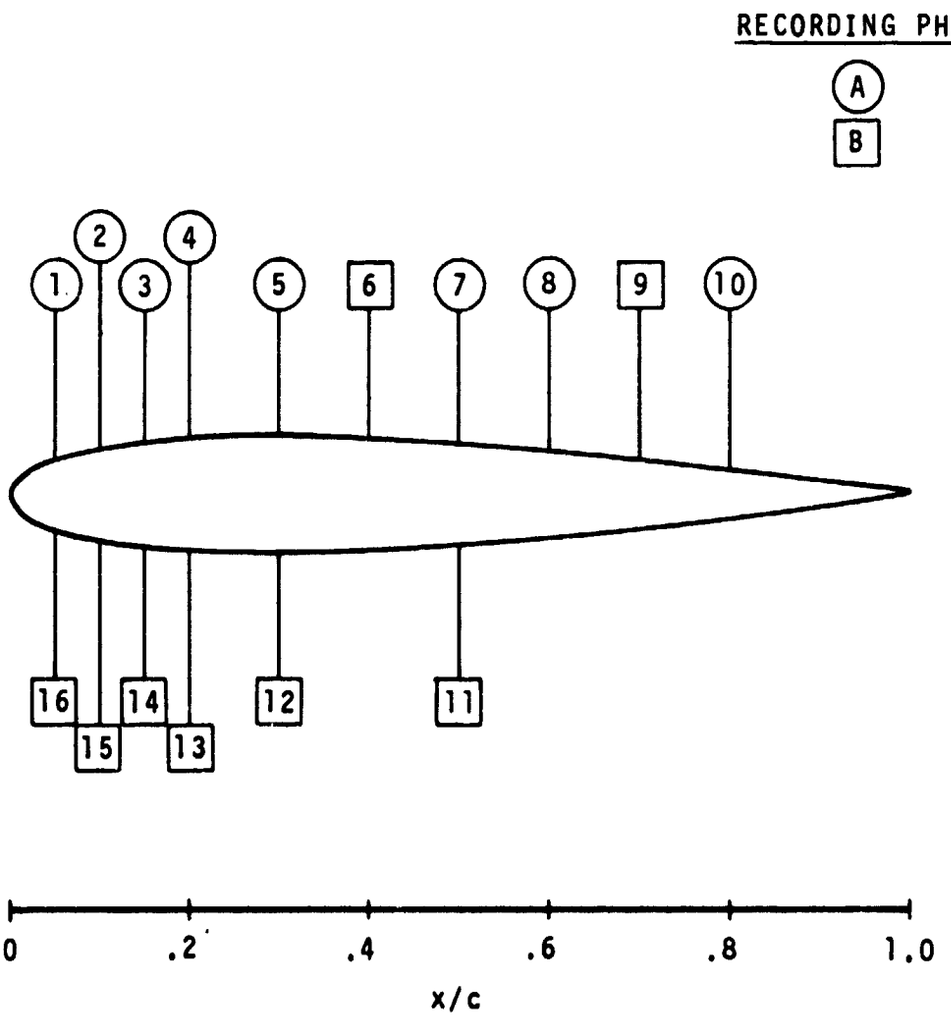

NOTE: TRANSDUCERS 11 AND 16 INOPERATIVE AT START OF TEST.

FIGURE 3 PRESSURE TRANSDUCER DISTRIBUTION

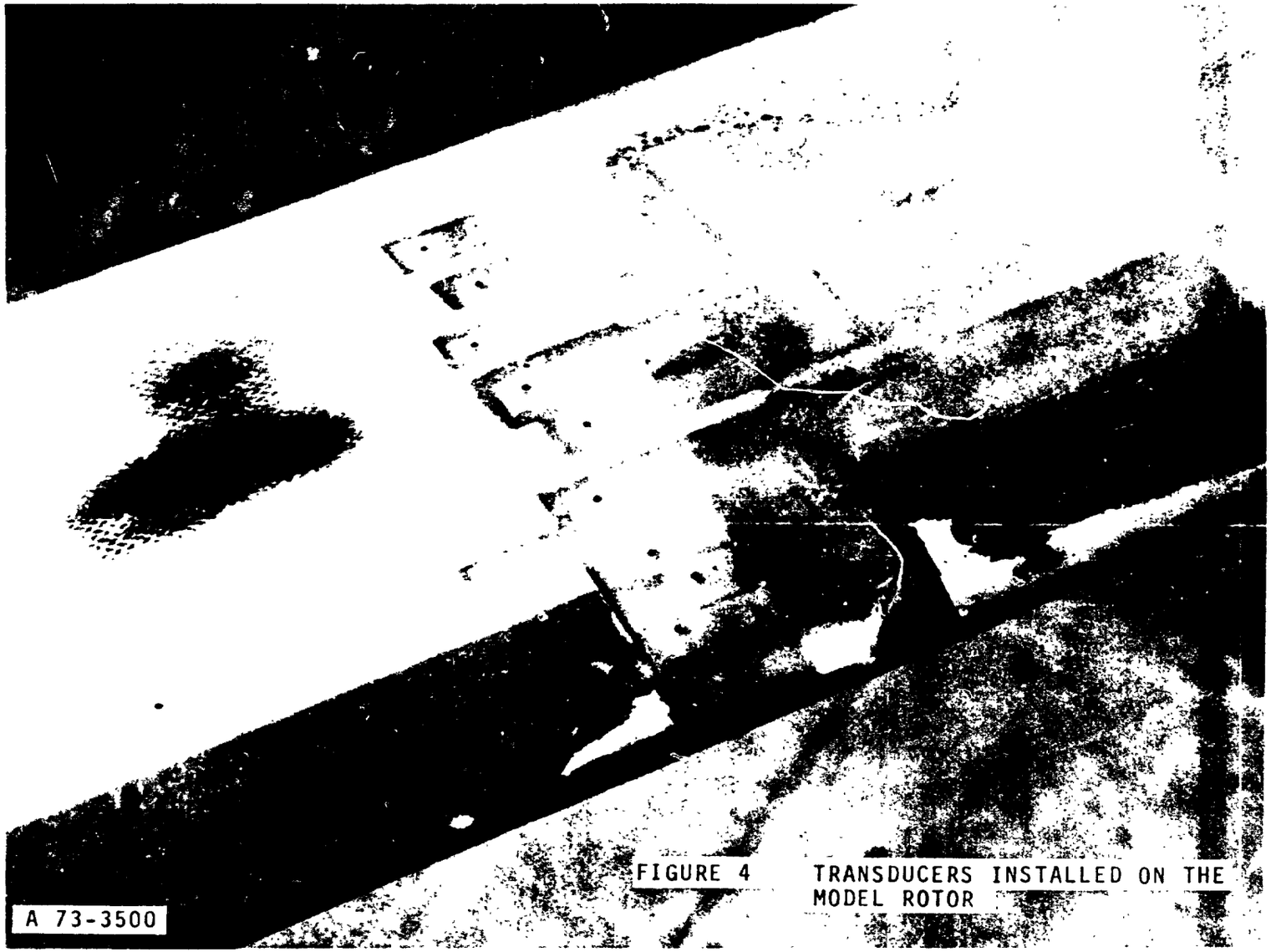

FIGURE 4 TRANSDUCERS INSTALLED ON THE MODEL ROTOR

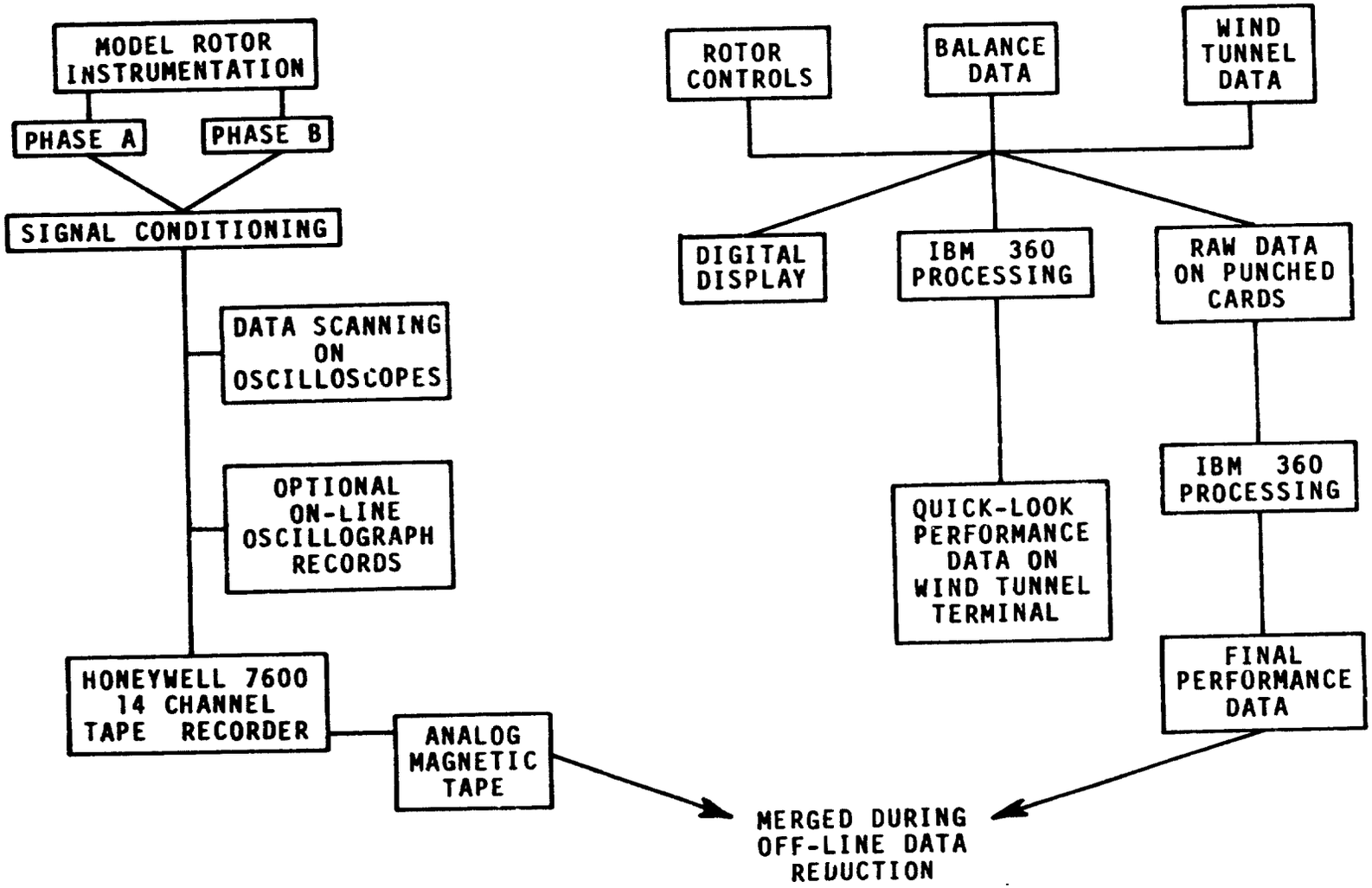

FIGURE 5 DATA ACQUISITION SYSTEM

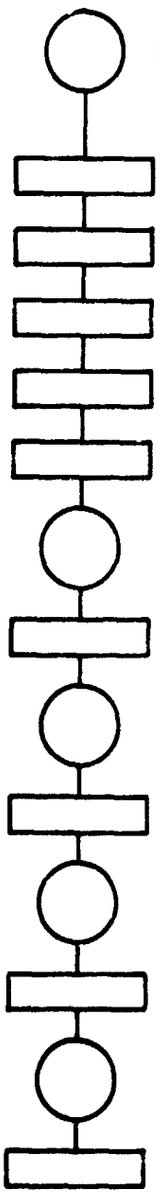

DIGITIZED TAPE FROM FLIGHT TEST

M40 DLM PATH

M40 - CALIBRATION PROGRAM

SORT ROUTINE - IN DATA CODE, TEST POINT, CYCLE ORDER

T43JM - HARMONIC ANALYSIS PROGRAM

AVERAGING PROGRAM - HARMONIC DATA

M44 - LISTING PROGRAM

HARMONIC ANALYSIS TAPE

M05 - EDITING PROGRAM

EDITED TAPE

T33 - HEADER PROGRAM

HEADER INFORMATION ON TAPE

T23 - LISTING PROGRAM

HARMONIC ANALYSIS + EDIT + HEADER ON TAPE

Y54AMES - PRESSURE BLADE ANALYSIS PROGRAM

FIGURE 6 - DATA REDUCTION SYSTEM

2.0 TEST PROGRAM

2.1 Summary of Test Conditions

Objective of this test was the acquisition of the following data:

(a) Sectional data at the 75% span station for the rotor in forward flight.

(b) Pressure transducer acceleration tares.

(c) Quasi-steady two-dimensional sectional data.

The test conditions at which the data was finally reduced and analyzed are shown in Table III. A more detailed summary of the performance data is shown in Table IV, in the Appendix. Some systematic plots and microfiche listings of tabulated data are included in Volume II of this report.

A substantial portion of the test was devoted to the acquisition of data on the sensitivity of the pressure transducers to acceleration loads. A number of different schemes was tried, but no method was found to successfully shield the transducers from the flow environment. The original test plan called for acceleration tare measurements at the same conditions for which forward flight data was obtained. If obtained, such data would have been applied to the data during final data reduction.

The forward flight data can be categorized as follows:

(a) Performance runs to define overall rotor characteristics (no pressure data).

(b) Matching of selected conditions from the full scale test described in Reference 3.

(c) Comparison with articulated rotor test conditions from the test described in Reference 2.

(d) Variation in tip path plane angle (i.e., propulsive force) at constant rotor lift to observe the effect of variations in the rate of change of angle of attack ($d\alpha/dt$) in absence of stall.

(e) Variation in shaft angle at constant collective pitch, for comparison with data in Reference 6.

TABLE III SUMMARY OF WIND TUNNEL TEST CONDITIONS

TEST POINT	C_T'/σ	μ	V_{TIP} (fps)	DESCRIPTION OF RUN	OBJECTIVE
14.03	.0469	.195	285	MATCH ROTOR CONTROLS FOR SELECTED POINTS FROM REF. 3	REPEAT TEST POINTS FROM BELL TEST IN REF. 3 TO VERIFY PRESSURE COEFFICIENT LEVELS
04	.1377				
06	.0570	.405			
07	.0546	.38			
08	.1234				
11	.0519	.189			
13	.1396				
17.03	.0675	.335	500	SHAFT ANGLE SWEEP AT CONSTANT COLLECTIVE (12.75°)	MATCH CONDITIONS FROM ARTICULATED ROTOR TEST BVWT 054, RUN 28 (REF. 2)
04	.0878				
05	.1023				
06	.1119				
07	.1278				
08	.0977				
09	.1084				
15	.1225				
16	.0976				
17	.0755	.335	500	VARIATION IN TIP PATH PLANE ANGLE AT CONSTANT LIFT (C_T'/σ=0.075)	STUDY PHENOMENA ASSOCIATED WITH CHANGES IN PROPULSIVE FORCE
18	.0747				
19	.0750				
20	.0757				
18.04	.0977	.335	500	REPEAT OF RUN 17.16	OBTAIN ADDITIONAL DATA, BECAUSE OF INSTRUMENTATION PROBLEMS WITH ORIGINAL RUNS
05	.0754			REPEAT OF RUN 17.18	
06	.0760			REPEAT OF RUN 17.19	
07	.1014	.143	285	VARIATION IN COLLECTIVE PITCH AT CONSTANT SHAFT ANGLE (α_s=-10.1°)	STUDY HIGH LOADING AT LOW ADVANCE RATIO. COMPARE TO DATA FROM REF. 6
08	.1116				
09	.1301				
10	.1407				
11	.1625				
12	.0643	.288	284	SHAFT ANGLE SWEEP AT CONSTANT COLLECTIVE PITCH ($\theta_{.75R}$=9°)	
13	.0751				
14	.0859				
15	.1241				
16	.1401				

2.1 Summary of Test Conditions (Cont'd)

(f) Variation in collective pitch at constant shaft angle, again for comparison with data from Reference 6.

Static two-dimensional data was acquired at the end of the test by mounting the instrumented blade on the turntable between the turntable surface (flush with the tunnel floor) and an end plate. The pressure data was obtained at several angles of attack for two tunnel velocities, V = 145 ft/sec (44.2 m/sec) and V = 225 ft/sec (68.6 m/sec). The two-dimensional data provided an estimate of transducer resolution capability at low speed conditions typical of the environment over a retreating rotor blade during forward flight.

Hover tests were conducted outside of the Wind Tunnel before the rotor was installed in the test section. The hover tests were run only as an initial check of transducer installation and the data was acquired by direct measurement of transducer output on a voltmeter. Manual records were made of several pressure distributions and it was concluded that the transducers were functioning normally.

2.2 Test Procedure

(a) Systematic Variation in Blade Controls. Test runs involving simple variation in controls were carried out by changing the controls to the desired values and then acquiring the pressure data. Balance and tunnel data records were made immediately before and after tape recorder operation.

(b) Matching Pre-determined Flight Conditions. Test runs involving the match of performance parameters were conducted through the following steps:

- Set the controls to an estimated value.
- Acquire balance and tunnel data.
- Process data through direct link with computer facility.
- Compare calculated performance data to desired value.
- If the conditions are sufficiently close to the conditions to be matched, proceed with pressure data acquisition. Otherwise, estimate new control values and repeat starting from the first step.

2.2 Test Procedure (Cont'd)

When the performance parameters to be matched included blade flapping or tip path plane angle, such angle was estimated from an on-line oscillograph strip-out of the measured root flapping angle.

2.3 Instrumentation Problems

Since the transducers appeared to be quite insensitive to acceleration loads, the problems encountered can be attributed entirely to malfunctions within the transducer circuits.

Two areas were clearly identified:

(a) The Slip Ring Assembly. The wire brushes were repeatedly damaged by the intense vibratory loads present when the rotor was flown through stall.

(b) A Faulty Relay. The relay circuit switching the transducer lines from recording Phase A to recording Phase B was also damaged by the vibratory loads, and eventually it started operating intermittently.

From the beginning of the test, transducers No. 11 and 16 were completely inoperative. The other transducers held well through the runs in which the Bell test data was repeated (tape 14) because of the low loads involved. When the tip speed was increased to 500 fps (152.4 m/sec) to match the conditions from the Vertol test, the resulting vibratory loads became considerably larger and several of the transducer output signals started degenerating rapidly. By the end of the runs at a tip speed of 500 fps (T.P. 17.17 to 17.19) several of the upper surface transducers and all but one of the lower surface transducers began to operate intermittently.

Some of the connections were then restored, but within a few runs all the lower surface transducers were again inoperative. This affects all the data taken to match the Landgrebe data from Reference 6. (T.P. 18.07 to 18.16)

As a result of these malfunctions the usefulness of the data was somewhat reduced. Whenever a transducer signal started drifting, the drift would produce large fluctuations in the computed pressure coefficients, which then contributed to erroneous integrated normal force and pitching moment coefficients. In some cases the number of malfunctioning transducers was sufficiently small to allow deleting them from the

2.3 Instrumentation Problems (Cont'd)

final integration, but for most of the test all but one of the lower surface transducers were inoperative and a reasonable approximation of lower surface pressures was very difficult to produce.

2.4 Data Reduction

The analog tapes containing the pressure, flapping, and pitch link load information were transferred to Boeing Vertol. At Vertol the data was scrutinized for bad data samples, digitized, converted to engineering units, harmonically analyzed over twelve harmonics, and finally processed through a data reduction program which combined the pressure data with other test information and computed all the necessary non-dimensional parameters. The data reduction path is illustrated in Figure 6.

Because of the problems outlined in the previous section the final data reduction program had to be re-run a number of times to delete those pressure values which were clearly erroneous.

2.5 Data Analysis

Data analysis was carried out after the test information was processed through the same final data reduction program used for the test data of Reference 2. Because of differences in rotor instrumentation the computer program was considerably simplified. Specifically, the present test did not have provisions for root-torsion, angle of attack, and skin-friction gage measurements, all of which played an important role in the articulated rotor test of Reference 2.

In the present test, one of the two blades was instrumented with pressure transducers as described in section 1.4. Since the pressure instrumentation did not extend to the trailing edge, an engineering approximation similar to the one used in Reference 2 was used to simulate the pressures all the way to the trailing edge. Near the end of the test, when the lower surface instrumentation started malfunctioning, an additional approximation was tried by fixing the stagnation point on the lower surface at the 0.05c station, but this was not always enough to allow the integration of reasonable normal force and pitching moment coefficients.

It should be pointed out that even when all the transducers functioned well, the lack of lower surface pressure ports

2.5 Data Analysis (Cont'd)

over the aft 50% of chord caused the integrated forces and moments to be somewhat underestimated, because some unsteady aerodynamic effects could not be accounted for. This is due to the fact that the differential pressure across the aft portion of an airfoil in an unsteady environment will exceed, at times, the corresponding quasi-steady differential pressure level. If this increase in loading was due entirely to an increase in upper surface velocities, than, to a first order of approximation, upper surface measurements alone would be sufficient. But from all indications, the increased loading is shared by both surfaces. This could be deduced from the fact that the pitching moment integration was consistently missing nose-down components which could only be contributed by the lower surface. As a result, the calculated pitching moments are generally in the nose-up direction.

A further verification of this will be discussed later in the comparison with the Bell data.

The engineering approximation used to reduce the data was the same used in the articulated rotor test in Reference 2. In such approximation the missing pressures are simulated with a parabolic distribution which passes through the furthest aft measured pressure on each surface and has an infinite slope at the trailing edge, i.e., $dC_p/d(X/C) = \infty$ at x/c = 1.0 where C_p is defined as zero. The equations for these parabolic distributions are as follows:

UPPER SURFACE

$$C_p = C_p(X/C=.8)\sqrt{\frac{1-X/C}{.2}} \qquad \text{for } x/c > 0.8$$

LOWER SURFACE

$$C_p = C_p(X/C=.3)\sqrt{\frac{1-X/C}{.7}} \qquad \text{for } x/c > 0.3$$

Such approximation would have been more successful if the pressure transducers at x/c = 0.8 on the upper surface and at x/c = .3 on the lower surface had functioned normally.

Pressure data was reconstituted at 5-degree increments of azimuth from the averaged harmonic data. The computation of the aerodynamic coefficients from the measured pressures was carried out in two different ways. The first way involved the

2.5 Data Analysis (Cont'd)

integration of just the measured pressures, without the engineering approximation discussed above. In this case the pressure coefficient was assumed to be zero aft of the 80% chord station on the upper surface and aft of the 30% chord station on the lower surface. The second way utilized the engineering approximation to simulate the pressures over the portions of the airfoil which were not instrumented.

The trapezoidal technique was used for the integration of the pressure data. All aerodynamic coefficients presented in this report were computed using the engineering approximation. A complete listing, in microfiche form, of the blade element aerodynamic coefficients every five degrees of azimuth position for every test point listed in Table IV, with and without the approximation applied, can be found in Volume II of this report. Volume II can be obtained by contacting G. Morehouse, Research Scientist, of the U.S. Army Air Mobility R&D Laboratory at Moffett Field, California.

Calculations based on classical rotor theory, Reference 4, using the measured blade flapping were made to determine the blade velocity environment and the local dynamic pressure at the 3/4 span station. This quantity was then used to non-dimensionalize the measured pressures. The non-dimensional pressure coefficients were then integrated to produce the necessary aerodynamic coefficients.

Approximate angles of attack were also calculated from the static airfoil characteristics by means of the following expression:

$$\alpha = \frac{C_{N_{DYNAMIC}} - C_{N(\alpha=0^\circ)STATIC}}{(dC_N/d\alpha)_{STATIC}}$$

but such angle of attack values are of very limited usefulness and they cannot replace angle of attack estimates obtained from direct flow measurements.

Other blade environment quantities were also calculated. A complete description of these quantities, as well as details of their calculations, is enclosed in the Appendix.

3.0 TEST RESULTS AND DISCUSSION

3.1 Non-Rotating (Static) Tests

Airfoil characteristics at angles of attack through stall at static conditions were obtained by mounting the instrumented blade in a two dimensional rig. The static data was acquired at two velocities, V = 145 ft/sec (44.2 m/sec) and V = 225 ft/sec (68.6 m/sec), to determine how well the instrumentation could measure pressures at low velocities representative of the flow environment of the retreating blade.

Pressure data was acquired at selected angles of attack between -20° and +20°. Data repeatability was influenced by the difficulty in setting an angle of attack to exactly the same value again.

Since the airfoil section is symmetrical, complete pressure distributions were obtained by superposing data at angles of attack of 6° with -6°, and 12° with -12°. Such superposition is illustrated in Figures 7 and 8 for V = 145 ft/sec (44.2 m/sec) and V = 225 ft/sec (68.6 m/sec) respectively.

Pressure distributions at and beyond stall at V = 225 ft/sec (68.6 m/sec) are shown in Figure 9.

At V = 225 ft/sec (68.6 m/sec) corresponding to a Reynolds Number Re = 4.75×10^5 and a Mach Number M = 0.2, the available pressure distributions show that the maximum normal force occurs at an angle of attack between 11° and 12° with a value of $C_{N_{MAX}} \approx 0.93$. The lift curve slope at low lift levels was estimated to be $dC_l/d\alpha = 0.095\ Deg^{-1}$.

The maximum normal force measured in this test agrees remarkably well with other measurements on the NACA 0012 summarized in Reference 7.

For comparison, the two-dimensional tests of the cambered section used on the articulated rotor test of Reference 2 showed that the V23010-1.58 at a Reynolds Number Re = 3×10^5 has a lift curve slope $dC_l/d\alpha \approx 0.10\ Deg^{-1}$, a maximum normal force $C_{N_{MAX}} = 0.92$, and a stall angle of 11°, measured from the zero lift value.

3.2 Hover Test

A number of hover conditions was run in a laboratory area prior to installation into the test section of the 7 x 10 ft

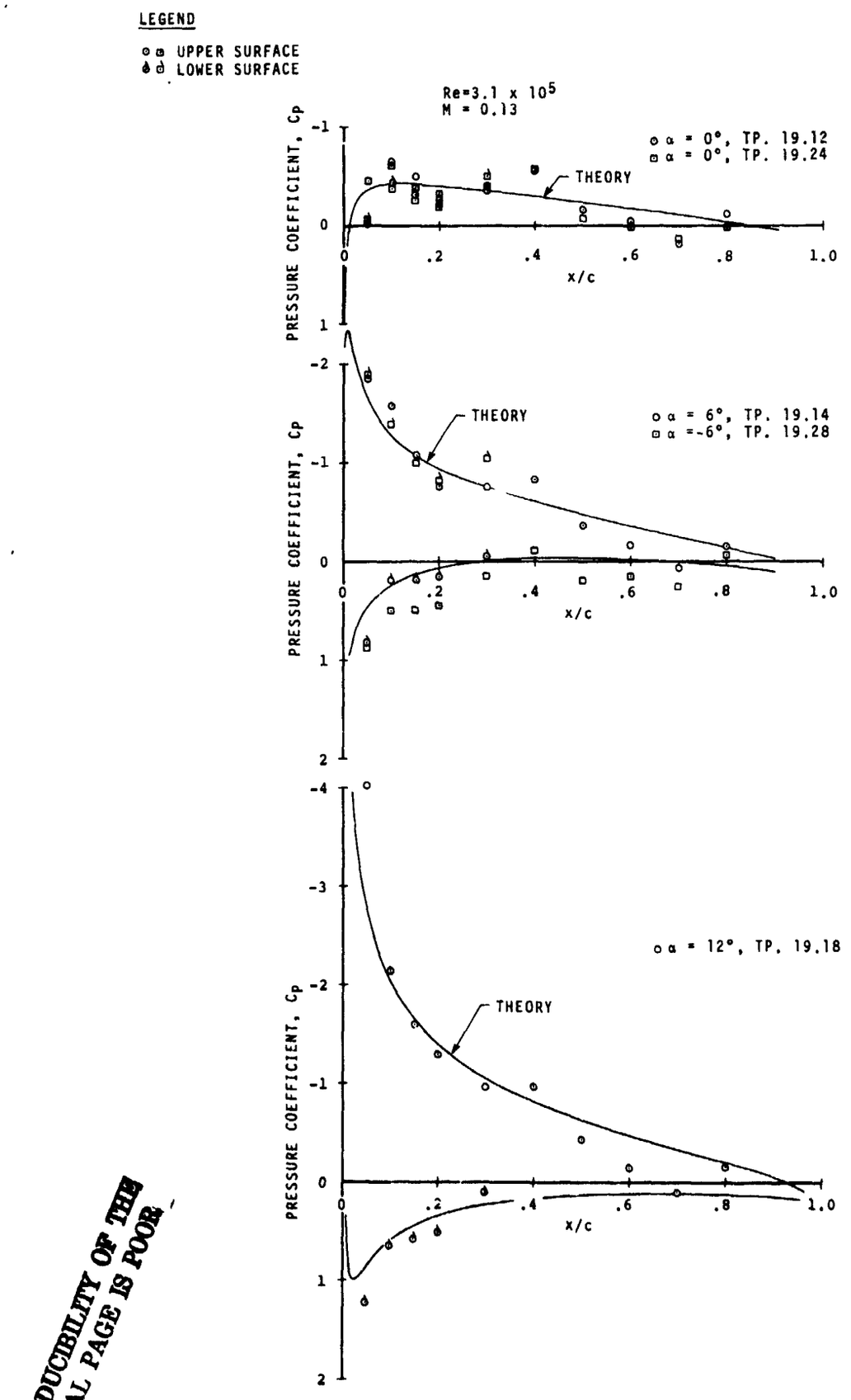

FIGURE 7 STATIC PRESSURE DISTRIBUTIONS OVER THE NACA 0012 AIRFOIL AT V = 145 fps

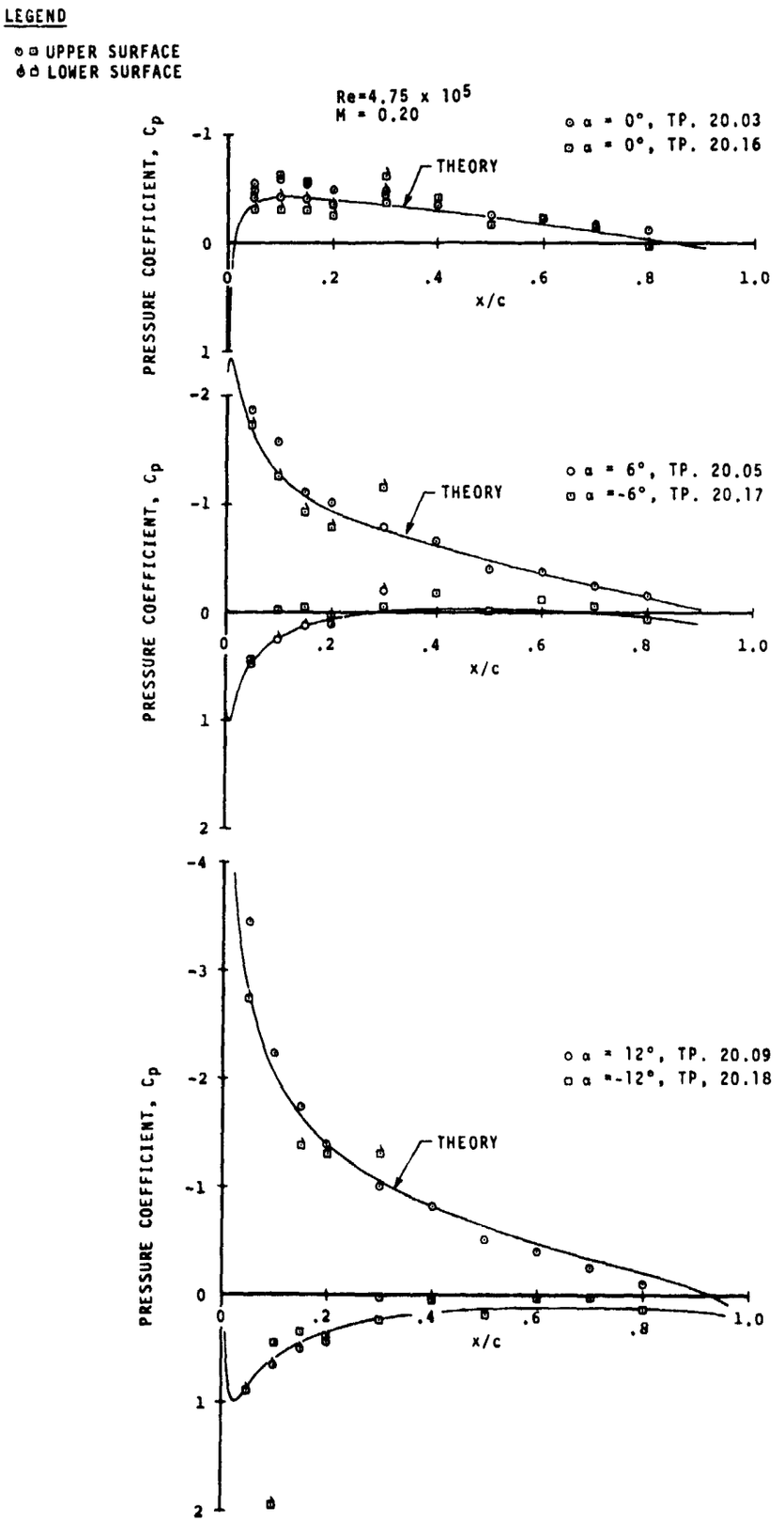

FIGURE 8 STATIC PRESSURE DISTRIBUTIONS OVER THE NACA 0012 AIRFOIL AT V = 225 fps

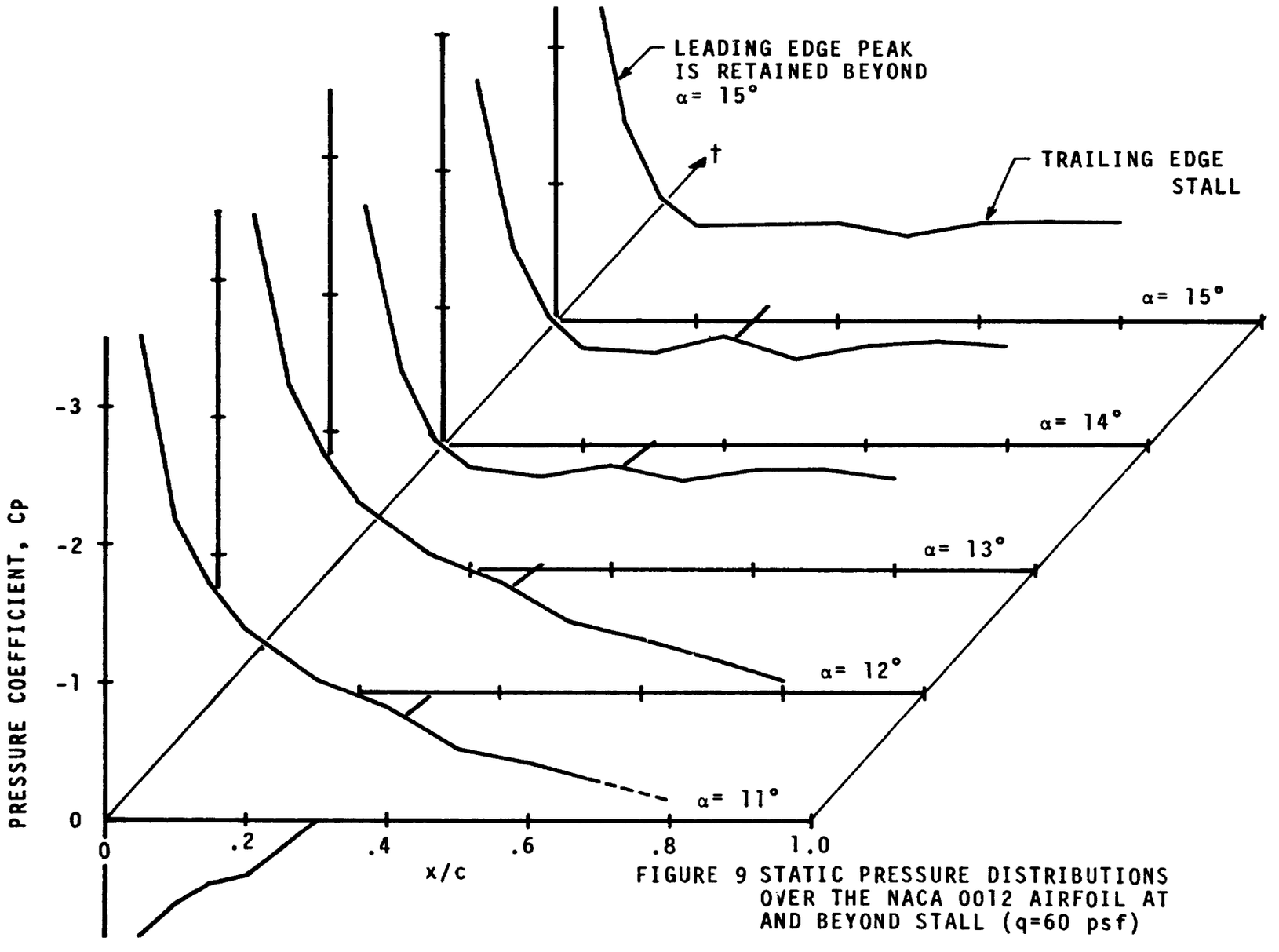

FIGURE 9 STATIC PRESSURE DISTRIBUTIONS OVER THE NACA 0012 AIRFOIL AT AND BEYOND STALL (q=60 psf)

3.2 Hover Test (Cont'd)

wind tunnel. The hover test was run to check out the transducer installation and to determine transducer sensitivity to centrifugal loads.

The part of the test devoted to isolating centrifugal loads gave inconclusive results because of the difficulty in sealing the transducers. It can be assumed, however, that centrifugal accelerations had negligible effect if we compare the measured pressure distributions with theoretical quasi-steady pressure distributions, as illustrated in Figure 10 for one condition.

During the hover test a limited amount of data was obtained by reading transducer output voltages directly on a voltmeter.

No hover performance data was taken in the laboratory area because the balance system is part of the Wind Tunnel. After the rotor was installed in the test section, hover data was not acquired because of wall proximity and recirculation effects.

3.3 Forward Flight Acceleration Tares

After the rotor was installed in the test section a substantial amount of testing was set aside to determine the best way of sealing the transducers and acquiring acceleration tares.

A number of unsuccessful schemes was tried.

(a) Sealing the pressure ports with single and double layers of tape.

(b) Laying down small discs of metal over the pressure ports before applying layers of tape. This was done to avoid any tape deflections ("oil-canning") caused by the varying pressure in the flow environment.

(c) Applying a sealing compound around the edge of small metal discs, and then applying layers of tape.

(d) Applying various arrangements of fiberglass sleeves over the layers of tape covering the transducers. Both sealed and ventilated sleeves were used.

No matter what sealing method was used, the transducers did not show any measurable response at the lower rotational

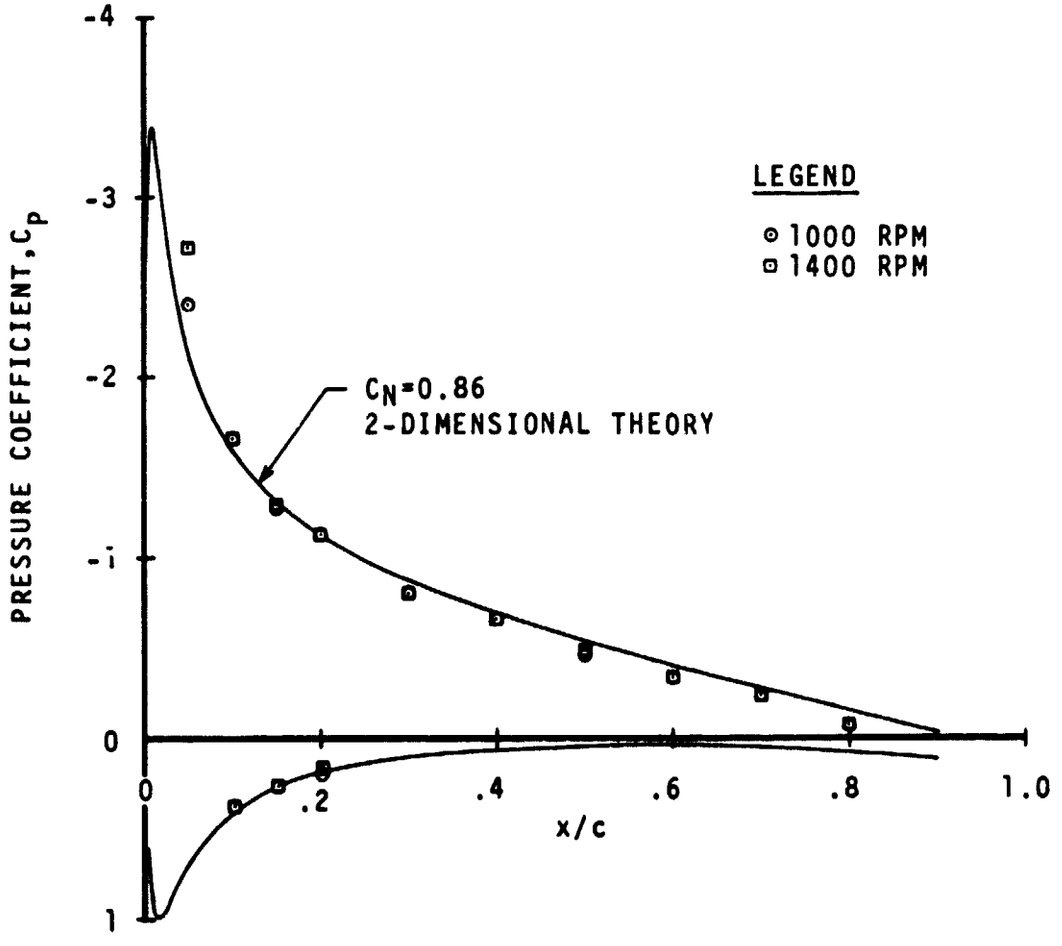

FIGURE 10 PRESSURE DISTRIBUTIONS AT THE 75% SPAN STATION IN HOVER

3.3 Forward Flight Acceleration Tares (Cont'd)

velocities (400 to 700 RPM). At rotational velocities above 1000 RPM the transducers started to pick up what appeared to be dynamic pressure fluctuations and finally, with increasing rotational velocity, the seal would either start leaking very significantly or it would break off entirely. The whole effort of obtaining acceleration tares was stopped after a few data points were taken to match the full scale data of Reference 3.

3.4 Comparison with Bell Data

The first objective of this test program was to determine the validity of the unexpected shifts in pressure coefficients measured over a set of full scale Bell blades, as reported in Reference 3. The results of the present test indicate that such shifts were not correct, and that the transducers employed on the full scale rotor were very sensitive to acceleration loads.

Figure 11 illustrates the difference between the full scale data from Reference 3 and the data from this test at a condition for which the shift in the full scale data was very significant. Figure 12 shows another comparison for a case in which the levels of the measured pressures are much closer. Although there is a discrepancy in the pressure levels, in both cases the differential pressures across the section appear consistent.

The comparison of Figures 11 and 12 also explains why in the present test the integrated loads are somewhat low. This is especially significant for the pitching moment coefficients which appear shifted in the nose-up direction because of the lack in lower surface instrumentation. The engineering approximation used to simulate the lower surface pressures does not account for the additional loading associated with unsteady aerodynamic effects, and for this reason, the calculated pitching moments, particularly before and after stall, are generally inaccurate.

Figures 13, 14, 15 and 16 compare the integrated normal force and pitching moment coefficients from this test and the full scale test of Reference 3. Since in the present test there was no provision for cyclic pitch control, test points from Reference 3 requiring lateral cyclic could not be repeated. However, the test conditions requiring only longitudinal cyclic were matched by replacing it with an increment in shaft angle.

3.4 Comparison with Bell Data (Cont'd)

The nominal test conditions for the data shown in Figures 13 through 16 are summarized below:

				7 Ft. Rotor			Full Scale Bell Rotor		
Fig	μ	V_T fps	$\theta_{.75R}$	T.P.	C_T'/σ	$\bar{X}$	T.P.	C_T'/σ	$\bar{X}$
13	.2	285	3.13°	14.03	.047	-.065	2.02	.051	-.093
14	.2	↓	11.08°	14.04	.138	-.425	2.04	.144	-.389
15	.4		3.03°	14.07	.055	-.029	2.10	.062	-.054
16	.4		8.15°	14.08	.123	-.150	2.12	.128	-.164

where the data for the full scale Bell rotor has been taken from Reference 9.

The integrated loads confirm the trends already pointed out in comparing individual pressure distributions:

(a) The normal force levels in the present test are generally lower than the levels measured in the full scale tests of Reference 3. Most of the difference must be due to incomplete integration caused by the absence of lower surface pressure instrumentation.

(b) That compared to the full scale data the pitching moments in this test are always off in the nose-up direction.

A comparison of pitching moments from the two tests, however, reveals also substantial differences in stall behavior which cannot be attributed entirely to the lack of lower surface instrumentation. Particularly significant are the differences in the stall events illustrated in Figures 14, 15 and 16.

In Figure 14, the model rotor of this test is shown to undergo a double stall, clearly visible in both normal force and pitching moment, which is not present at all in the full scale data. The full scale data shows a moderate lift stall event but, except for a gradual shift of the pitching moment coefficient in the nose-down direction, there is no sign of an abrupt pitching moment stall.

3.4 Comparison with Bell Data (Cont'd)

Figure 15 shows another discrepancy between model scale and full scale data, except that in this case it is only the full scale data that shows evidence of stall. The pressure distributions at the $\Psi = 270°$ azimuth location for this particular condition are compared in Figure 11. From Figure 11 it is quite clear that the lack in lower surface instrumentation on the model blade is the reason why the loading across the aft portion of the blade section was underestimated, resulting in a large error in the calculated pitching moment coefficients.

Finally, Figure 16 shows agreement between the model rotor and the full scale rotor at least to the extent that both rotors stall. However, the model scale rotor displays a clear double-stall event which is completely absent in the full scale data.

The azimuthal variation in pressure distributions for a test condition in which stall was observed is shown in Figure 17. At this particular condition (T.P. 14.04) full stall recovery does not take place until the blade has returned to $\Psi = 20°$ in the first quadrant.

3.5 Comparison with Articulated Rotor Data

(Test Points 17.03 to 17.07, M = .34, V_T = 500 fps (152.4 m/sec), $\theta_{0.75R} = 12.75°$)

This portion of the test was run at conditions selected to allow a meaningful comparison between teetering and articulated rotors.

The articulated rotor test, documented in Reference 2, was conducted with geometrically scaled models of production CH-47B blades. Such blades were tested on a three-bladed rotor system configuration with constant chord and a linear twist variation along the span. The airfoil used on the CH-47B is the V23010-1.58, a cambered airfoil similar to the NACA 23010 with the leading edge radius of the NACA 23012. The basic data for the two rotors is:

	Teetering Rotor	Articulated Rotor
Airfoil Designation	NACA 0012	V23010-1.58
Chord	4.25 in. (10.79 cm)	3.367 in. (8.55 cm)

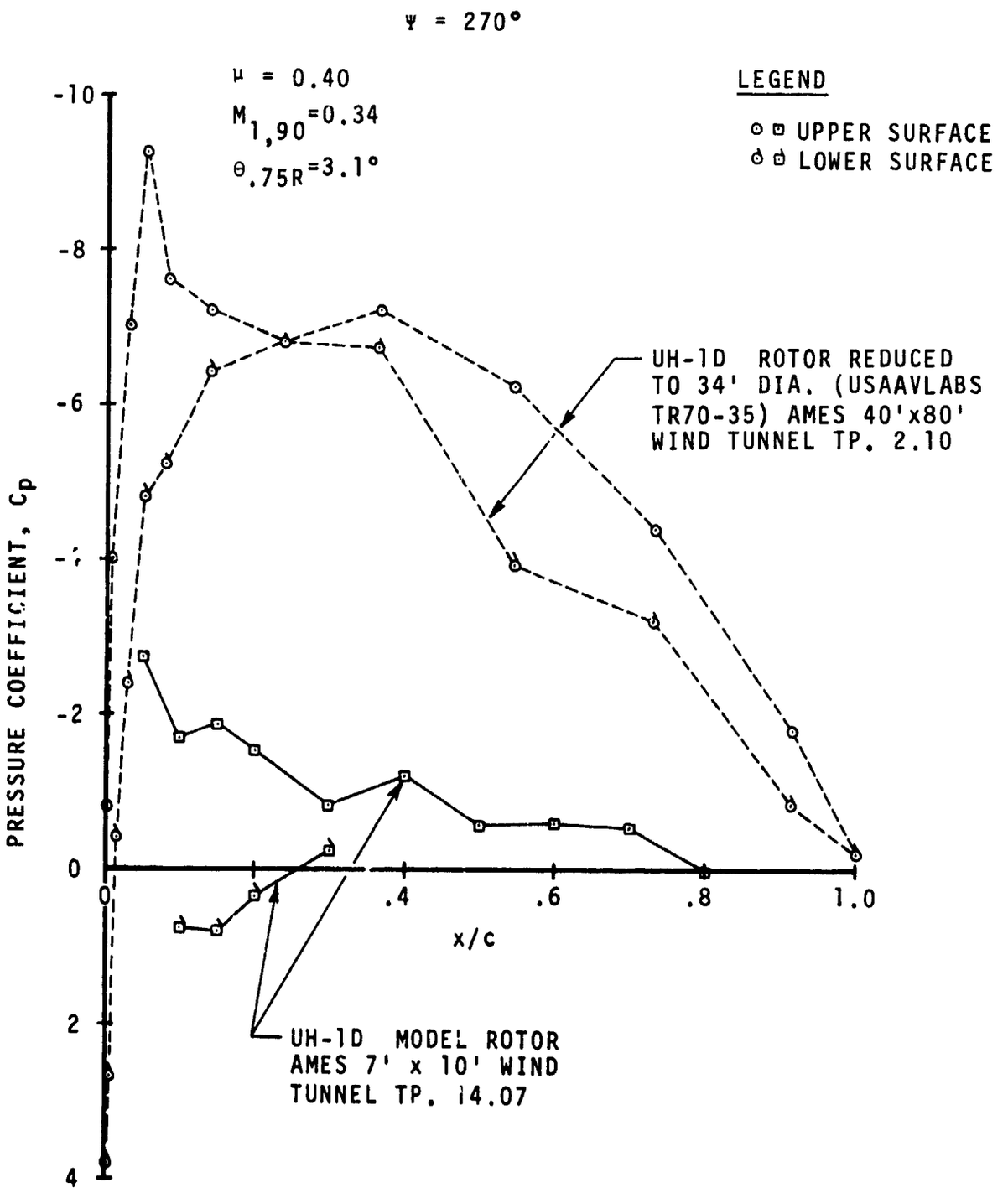

FIGURE 11 COMPARISON BETWEEN FULL SCALE AND MODEL SCALE PRESSURE DISTRIBUTIONS

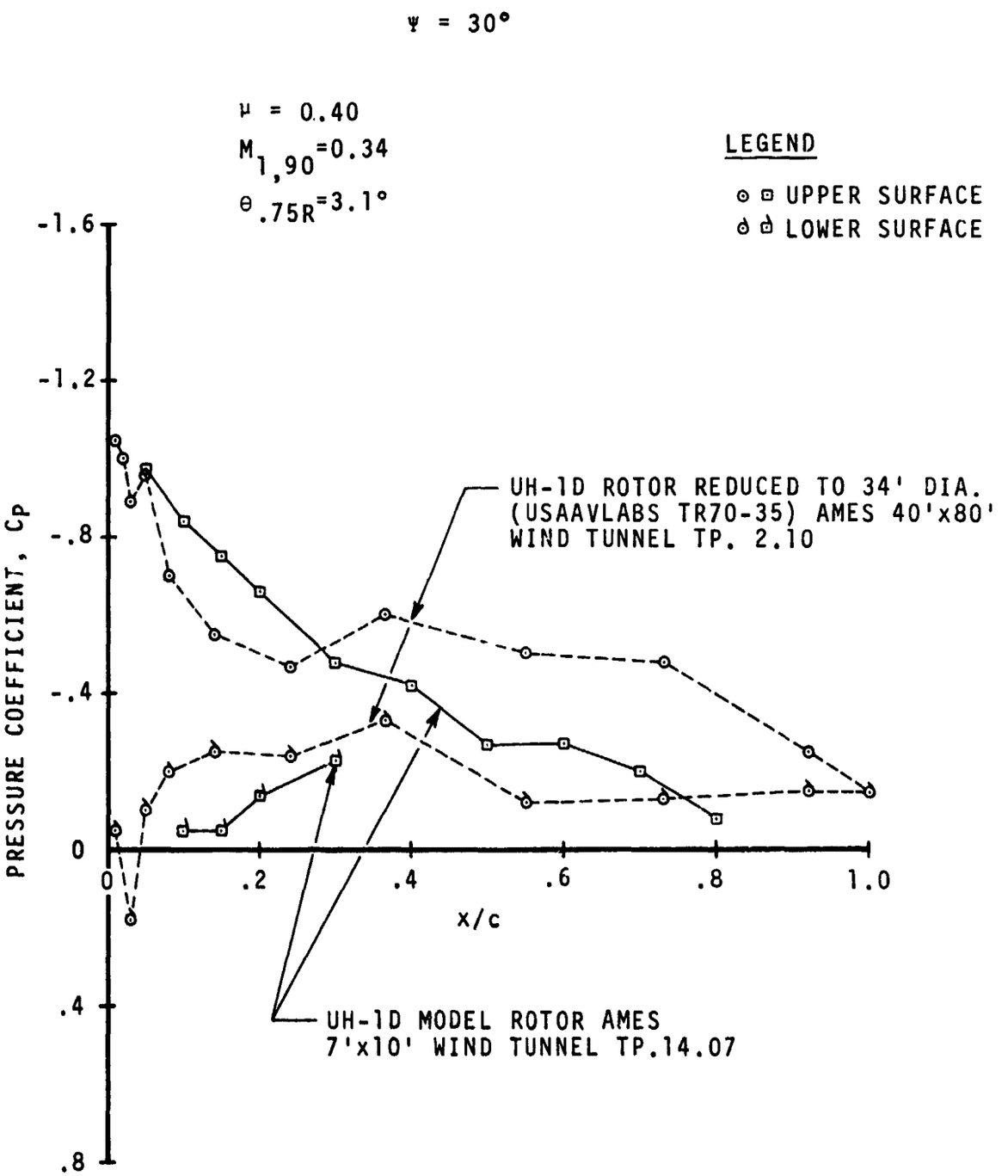

FIGURE 12 COMPARISON BETWEEN FULL SCALE AND MODEL SCALE PRESSURE DISTRIBUTIONS

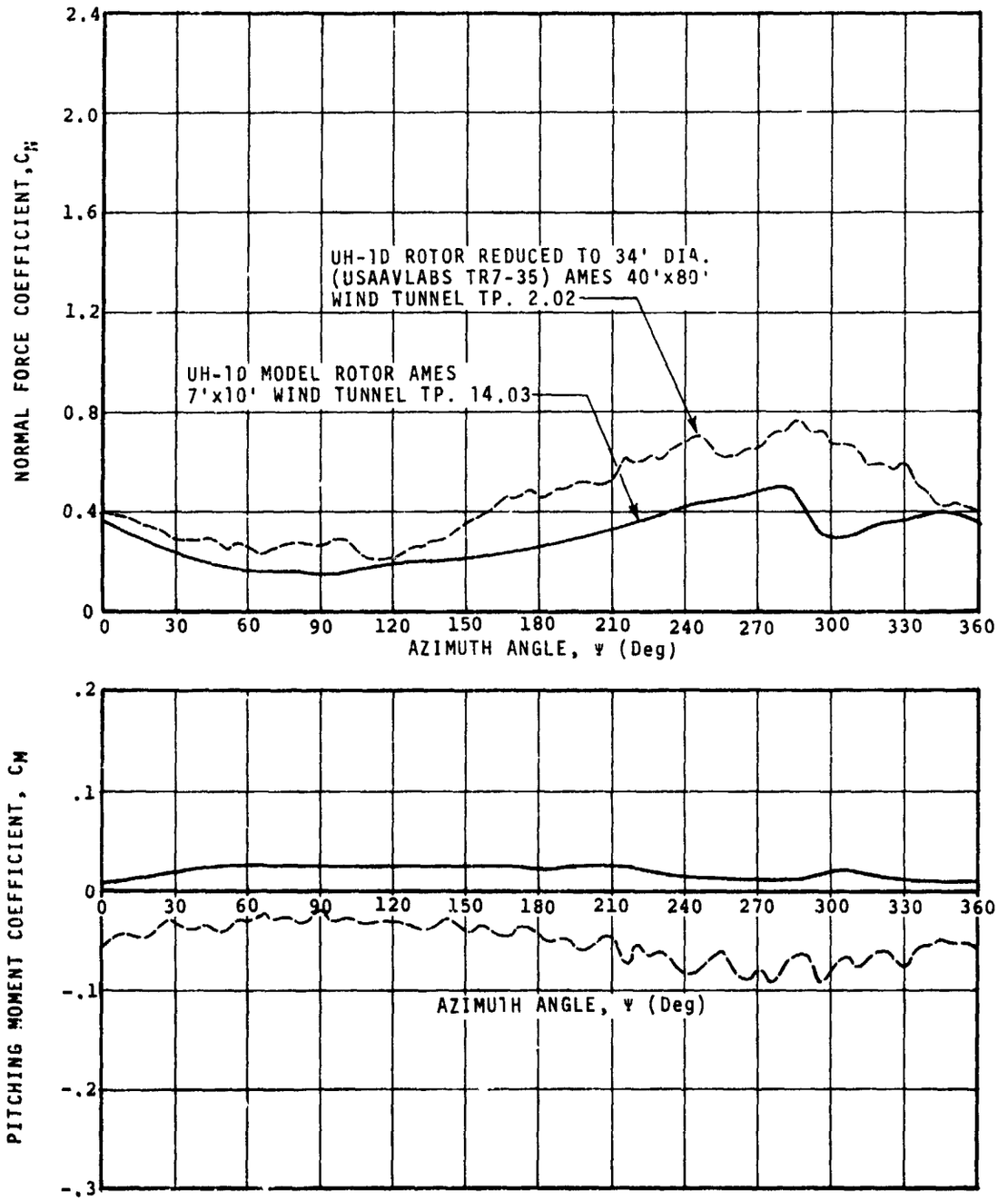

FIGURE 13 INTEGRATED LOADS FOR TEST POINT 14.03,
μ=0.195, $M_{1,90}$=0.296, $\theta_{.75R}$=3.1°
COMPARISON WITH FULL SCALE DATA

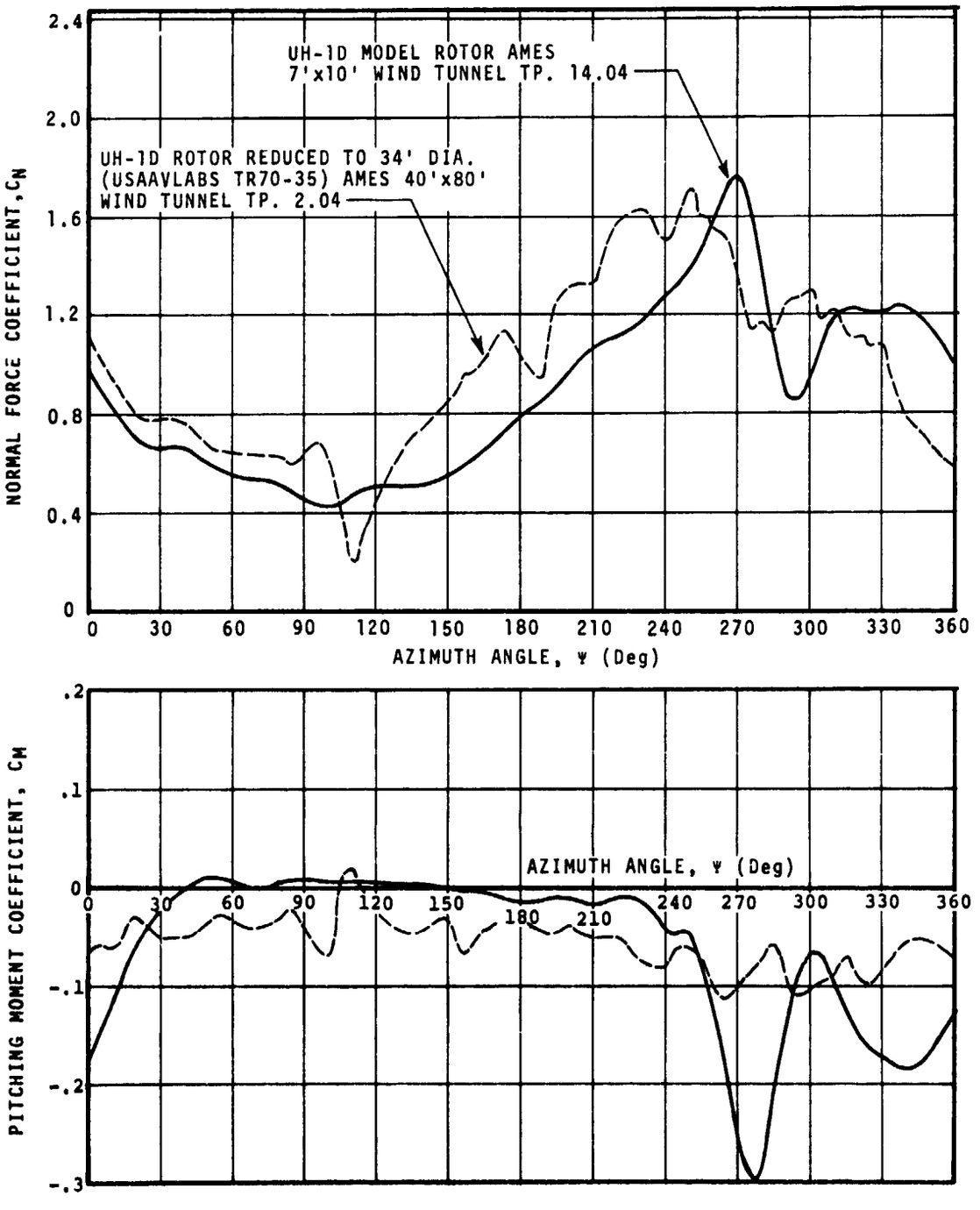

FIGURE 14 INTEGRATED LOADS FOR TEST POINT 14.04
μ=0.194, $M_{1,90}$=0.297, $\theta_{.75R}$=11.1°
COMPARISON WITH FULL SCALE DATA

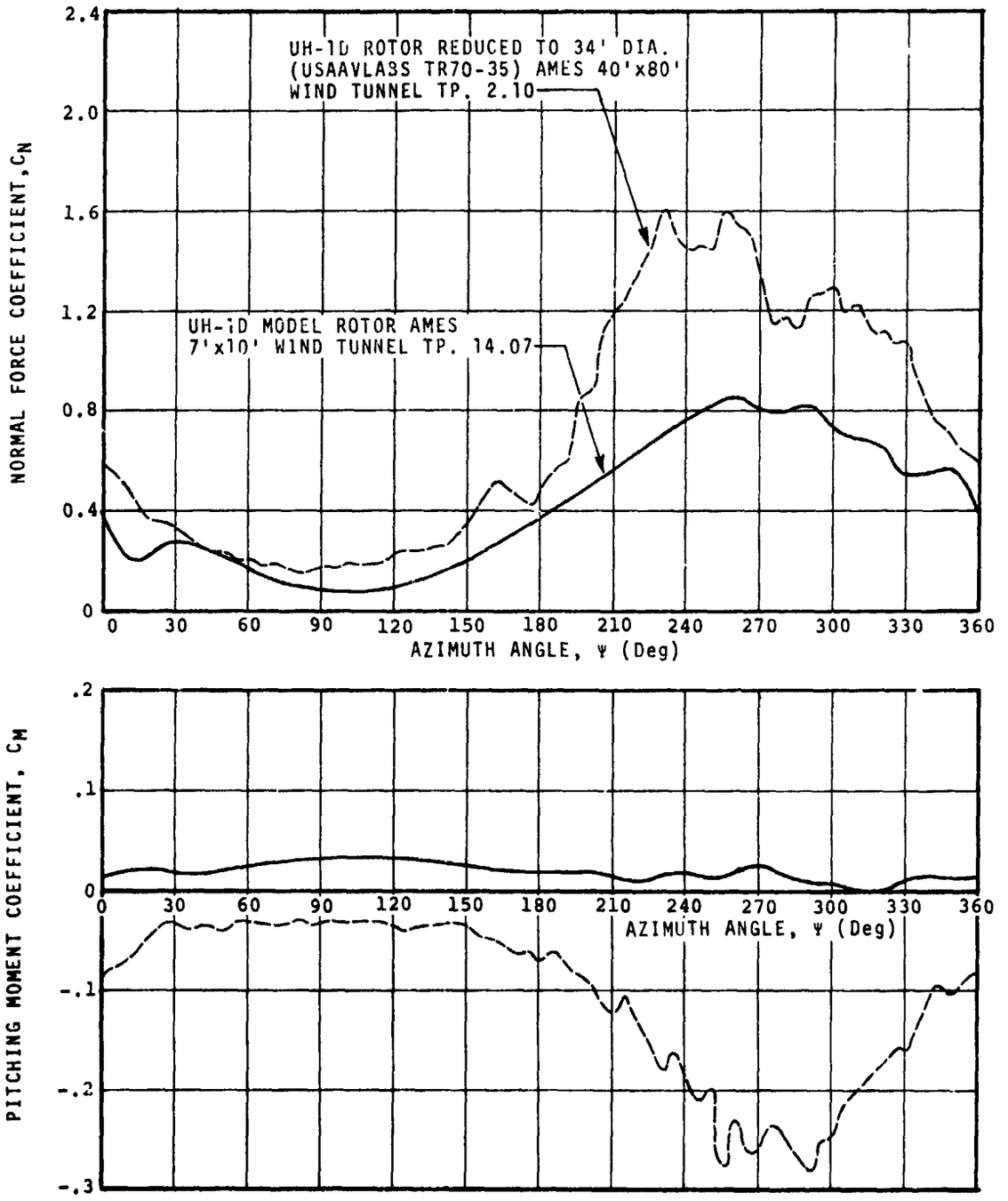

FIGURE 15 INTEGRATED LOADS FOR TEST POINT 14.07,
μ=0.381, $M_{1,90}$=0.347, $\theta_{.75R}$=3.03°
COMPARISON WITH FULL SCALE DATA

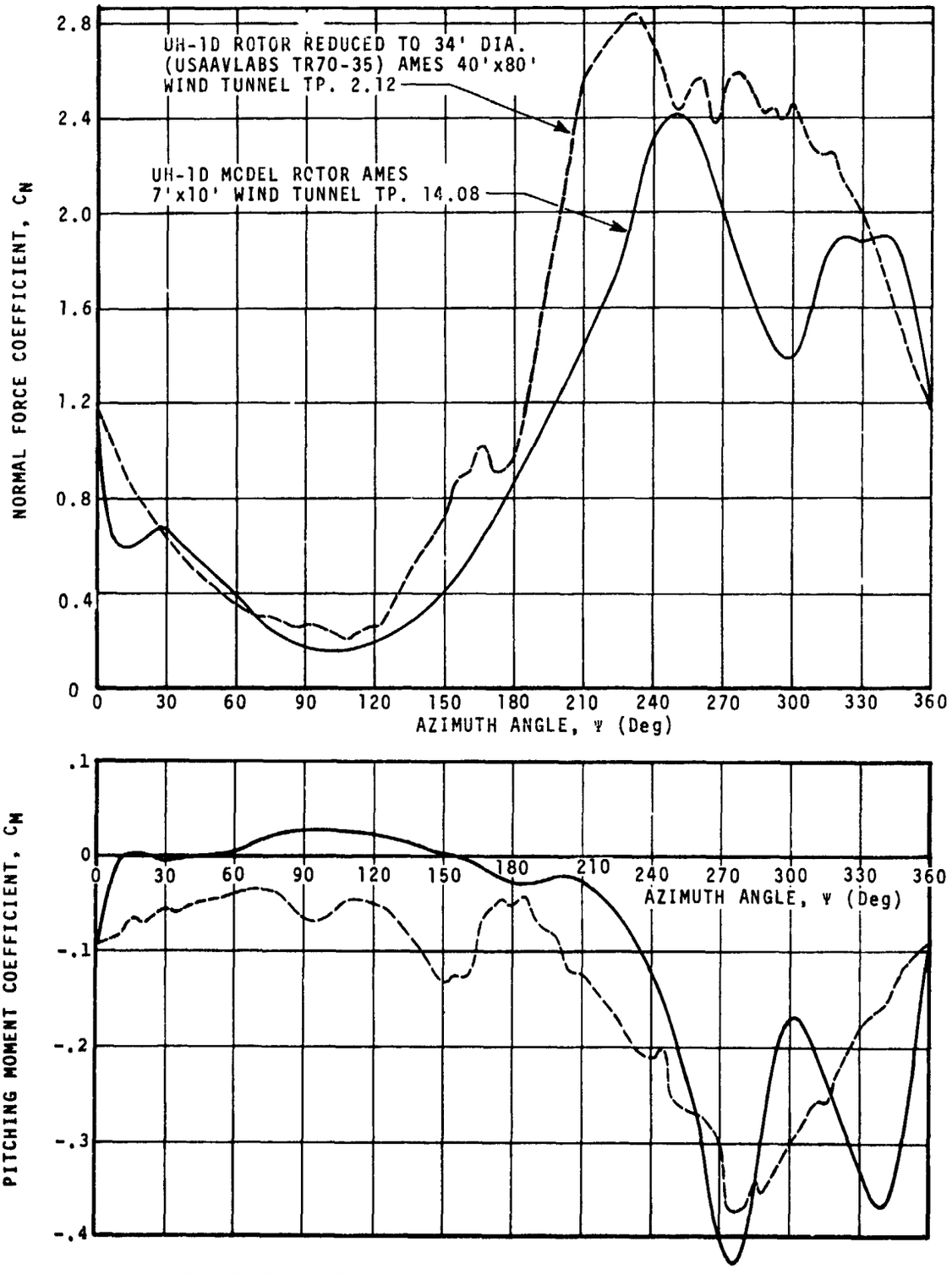

FIGURE 16 INTEGRATED LOADS FOR TEST POINT 14.08,
μ=0.384, $M_{1,90}$=0.347, $\theta_{.75R}$=8.15°
COMPARISON WITH FULL SCALE DATA

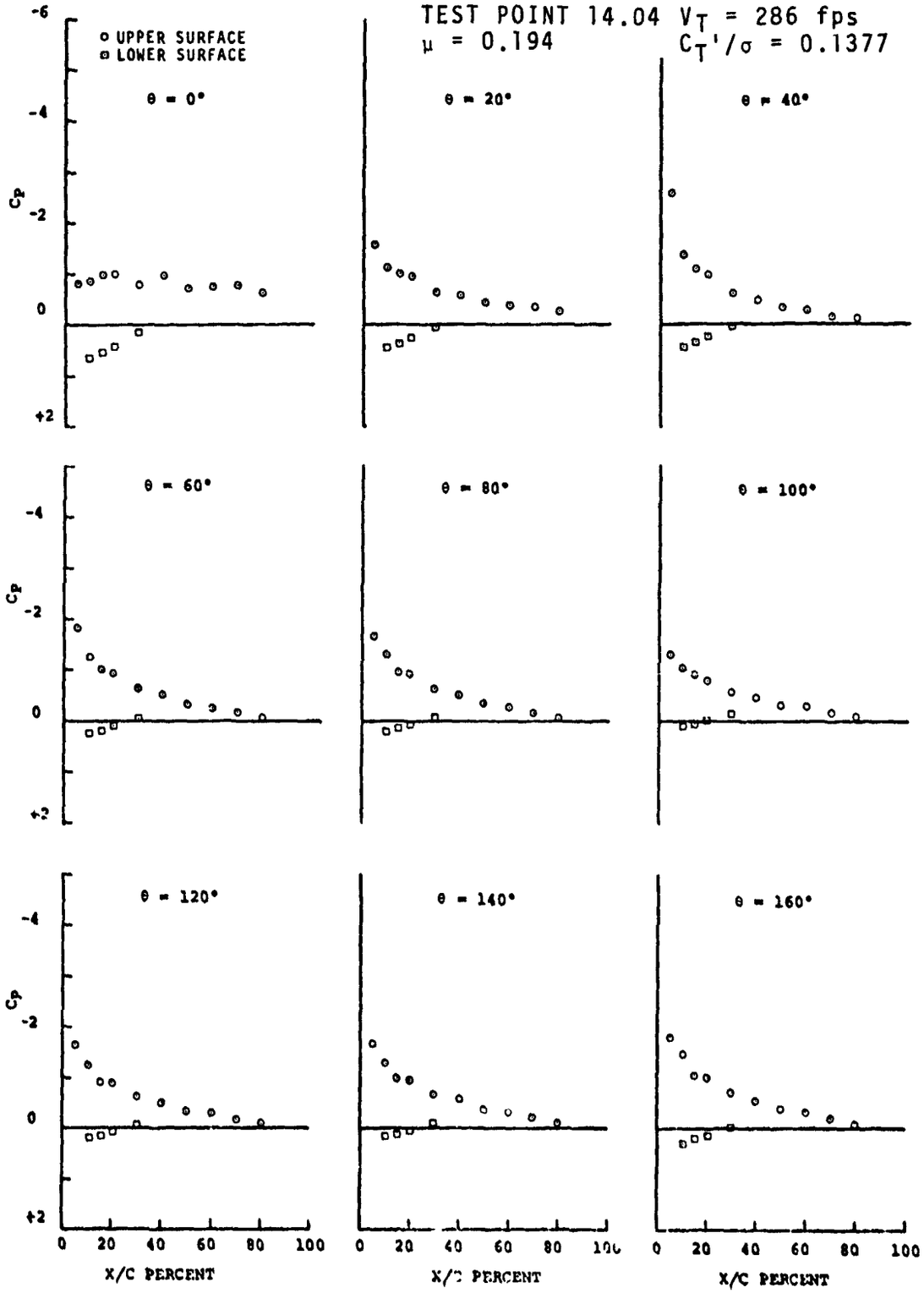

FIGURE 17 PRESSURE DISTRIBUTIONS MEASURED AT 0.75R

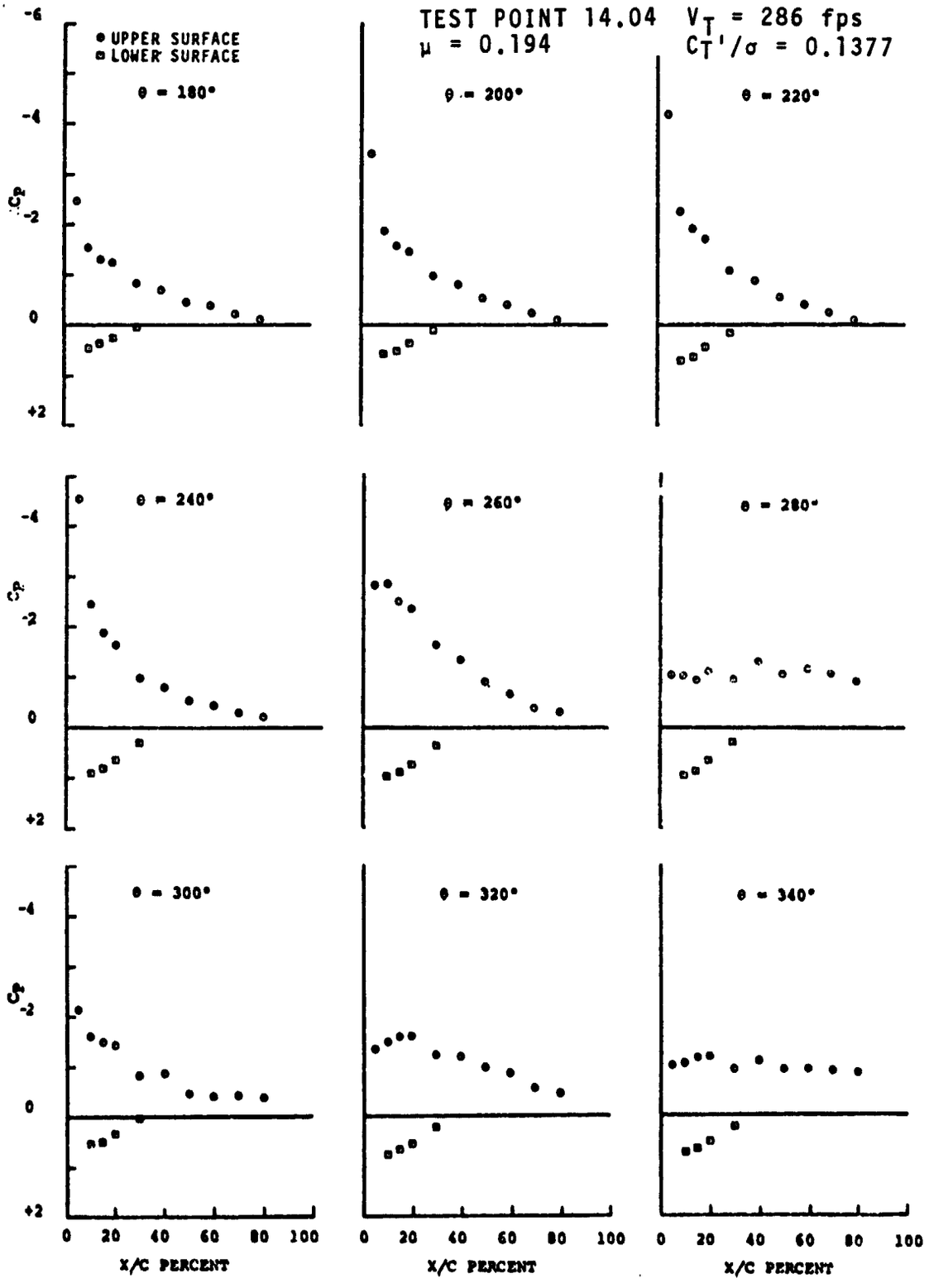

FIGURE 17 PRESSURE DISTRIBUTIONS MEASURED AT 0.75R

(CONCLUDED)

3.5 Comparison with Articulated Rotor Data (Cont'd)

	Teetering Rotor	Articulated Rotor
Radius	3.5 ft. (106.7 cm)	4.0 ft (121.9 cm)
No. of Blades	2	3
Twist	0°	-10.8°
Root Cutout	.119R	.192R
Solidity	.0644	.067

In addition to absolute pressure transducers at the 0.75R station, the articulated rotor model included skin friction gages to study boundary layer separation effects, differential pressure transducers calibrated to measure the instantaneous angle of attack, and strain gages to measure root torsion.

Because of the reduced amount of instrumentation in the present test, the two rotors can be compared only on the basis of integrated pressures as measured at the 0.75R station.

The basic performance data for the two rotors is compared in Figure 18. Both rotors were tested by varying the shaft angle at constant collective pitch. The top portion of Figure 18 compares the two rotors on the basis of rotor lift, C_T'/σ, and tip path plane angle. The teetering rotor did not achieve as high a lift level as the articulated rotor because beyond $C_T'/\sigma = 0.128$ the teetering rotor vibrated so violently that without any instrumentation to monitor blade loads, it was considered unadvisable to further increase the lift.

Rotor lift and power data is compared in the bottom part of Figure 18. However, a comparison of actual power levels between the two rotors is not possible with the data presently available because, for the teetering rotor model, the frictional losses in the drive mechanism have been estimated only approximately.(1) The power measurements,

(1) A comparison with theoretical performance predictions indictes that the power measured is low.

3.5 Comparison with Articulated Rotor Data (Cont'd)

qualitative as they were, indicate that the teetering rotor encountered significant amounts of separated flow at lift levels about $C_T'/\sigma = 0.08$. The power requirements for the articulated rotor increase at about the same lift level, but at a significantly reduced rate. This difference could be attributed to the combined effects of blade twist and sectional characteristics.

Root flapping angles for the two rotors are compared in Figure 19. The top portion of Figure 19 shows the flapping angles for the teetering rotor, including the pre-cone angle of 1.5°, and the bottom half shows the flapping angles for the articulated rotor, significantly reduced in amplitude at comparable lift levels because the articulated rotor operated with almost 5° of longitudinal cyclic, which reduced the flapping amplitude necessary to match the tip path plane angle.

Integrated normal force time histories are compared in Figure 20. At high lift levels both rotors display the "double stall" behavior observed in the previous section with the data matching the Bell test conditions. Such effect is more pronounced on the teetering rotor at lift levels above $C_T'/\sigma = 0.11$, although the articulated rotor displays a large number of small fluctuations at azimuth angles beyond $\Psi = 300°$.

There are also significant differences in the maximum attained value of the normal force. On the articulated rotor the maximum normal force coefficient is about $C_N = 2.9$, and all C_N peaks occur at $230° < \Psi < 250°$. On the teetering rotor maximum normal forces occur at $230° < \Psi < 285°$ ($C_T'/\sigma = 0.10$) after which it occurs progressively sooner with increasing lift ($\Psi = 255°$ for $C_T'/\sigma = 0.128$). The maximum normal force measured on the teetering rotor in this run sequence is $C_N = 2.05$. With increasing lift the secondary C_N peak also grows in magnitude and occurs earlier.

The difference in the maximum attained normal force coefficient could be attributed to any of the following causes:

(a) Differences in the maximum lift capability between the NACA 0012 and the V23010-1.58 airfoil sections.

(b) Incomplete normal force integration.

(c) Unsteady aerodynamic effects.

3.5 Comparison with Articulated Rotor Data (Cont'd)

(d) Differences in angle of attack environment.

At full scale Reynolds Numbers (i.e., with a 25.25 inch chord on the CH-47B rotor) the difference in maximum lift capability between the V23010-1.58 and the NACA 0012 is $\Delta C_{N_{MAX}} = 0.5$, at M = 0.2. At the reduced Reynolds Numbers of these tests the static data show no difference in the low Mach Number maximum lift capability of the two sections. Specifically, at M = 0.2 the Reynolds Number and maximum normal force coefficient for the NACA 0012 were $Re = 4.75 \times 10^5$ and $C_{N_{MAX}} = 0.93$, and for the V23010-1.58 $Re = 3.75 \times 10^5$ and $C_{N_{MAX}} = 0.92$. At Mach numbers about M = 0.4 the V23010-1.58 would benefit of camber effects over the NACA 0012, but the Mach Number environment at the 0.75R span station over the retreating blade is too low to justify any significant differences in the static maximum lift capability (at $\Psi = 225°$ the local Mach Number is just M = 0.24, and at $\Psi = 270°$ it is M = 0.19).

The incomplete integration due to the lack in lower surface instrumentation will vary azimuthally as a function of chordwise loading, but it probably amounts to an error in normal force $-0.2 < \Delta C_N < -0.1$.

Since items (a) and (b) above do not contribute significantly to the observed differences in the maximum normal force coefficients, these differences may be due to some combination of flow environment and unsteady aerodynamic effects. The single most significant difference in rotor environments is an increment of about 4.0° in first harmonic flapping, with the teetering rotor undergoing the larger flapping excursions (Figure 19).

Without taking into account any differences in elastic deflections (both in torsion and flap bending) between rotor blades, it is obvious that the blade undergoing larger flapping excursions will expereience a larger reduction in local angle of attack as the blade moves up with respect to the disc plane, such as is the case for the teetering rotor.

Since the teetering and articulated rotors were considerably different in controls as well as blade stiffness and airfoil sections, it is not feasible to separate the combined effect of pitching and plunging motions on the sectional dynamic stall characteristics.

3.5 Comparison with Articulated Rotor Data (Cont'd)

Pitching moment coefficients are compared in Figure 21. The integrated values for the teetering rotor display a nose up shift of approximately $\Delta C_m = +0.05$ due to the lack of lower surface instrumentation aft of the 0.30c station, but the pitching moment data is generally consistent with the normal force data.

First of all the pitching moment displays the same "double stall" character as the normal force. This is not surprising, since partial flow reattachment implies that the center of pressure has moved forward and so the pitching moments about the quarter chord will be reduced.

Quite predictable is also the fact that pitching moment stall precedes the normal force stall. This stall character is well known and consistently displayed by two-dimensional airfoil data. What is somewhat surprising is that on the articulated rotor the maximum pitching moment after stall is attained almost concurrently with the maximum normal force, while on the teetering rotor the maximum pitching moment lags the maximum normal force by $\Delta\Psi = 20°$ to $30°$. On the teetering rotor such shift is less evident for the "second stall", although then C_N lags $C_{M_{MAX}}$ by $\Delta\Psi = 10°$ at the highest rotor lift ($C_T'/\sigma = 0.128$). It could be, of course, that such apparent lag is due to incomplete integration.

Another phenomenon which cannot be entirely attributed to incomplete integration is the magnitude of the largest pitching moment after stall. Such pitching moment levels are substantially reduced on the teetering rotor when compared to the articulated rotor, but we can justify such changes from unsteady aerodynamic considerations. The oscillating airfoil data from several sources (e.g., Reference 1) show that at a fixed reduced frequency of oscillation (sinusoidal forced pitch oscillation for the test in Reference 1) the maximum pitching moment after stall will increase with increasing amplitude of oscillation. If we assume again that the two rotors have sections with approximately the same lift curve slope, then we can see from Figure 20 that the articulated rotor was subjected to greater excursions in angle of attack than the teetering rotor, and this, translated into a larger effective amplitude of oscillation, would justify the increase in maximum pitching moment.

A rough estimate of the angle of attack excursions, obtained by dividing maximum normal force values by a nominal lift curve slope, is sketched below:

3.5 Comparison with Articulated Rotor Data (Cont'd)

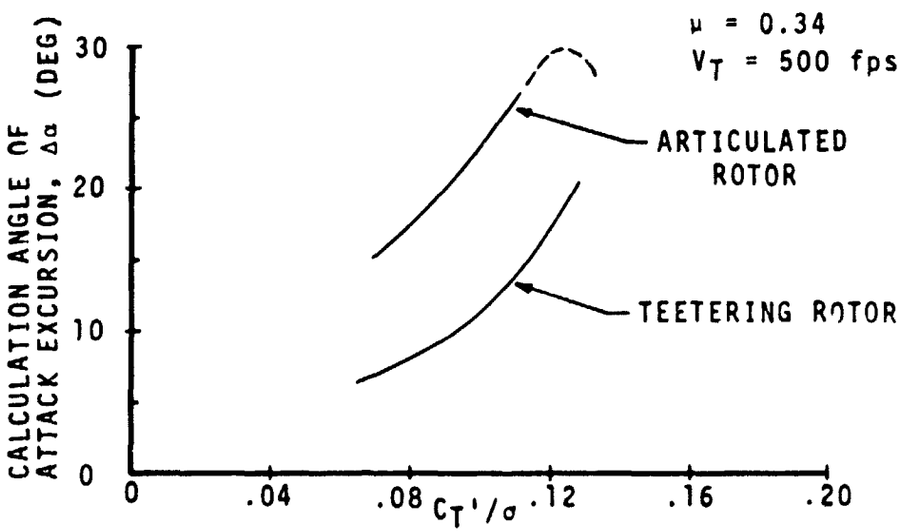

Finally, Figure 22 compares the stall events for the two rotors by comparing loops of the pitching moment coefficient plotted against the normal force coefficient over a complete cycle. This kind of data presentation offers some additional insight into the relationship between normal force and pitching moment stall, and it also shows very strikingly the "double stall" behavior already discussed in conjunction with the normal force and pitching moment time histories. An example of such double stall has been observed on two-dimensional oscillating airfoil data and it is reported in Reference 5. Comments pertaining to the various aspects of the stall events have been already made. This kind of plot illustrates well the fact that in this teetering rotor test the maximum negative pitching moment was attained after a considerable amount of normal force had already been lost, while on the articulated rotor the maximum normal force and the maximum lift occurred almost simultaneously.

Time histories of upper surface pressures for test points 17.03 through 17.07 are shown in Figures 23 to 27. The pressures shown were measured at the 0.05c, 0.10c, 0.30c, and 0.80c stations. Of greater interest of course are the conditions in which stall is present, i.e., test points 17.05, 17.06, and 17.07.

In general, the pressure data confirms the trend, observed in Reference 2, that the first event in stall is the collapse of the leading edge pressure peak, followed by the attainment

3.5 Comparison with Articulated Rotor Data (Cont'd)

of $C_{N_{MAX}}$, and then followed by $C_{M_{MAX}}$. The leading edge pressures also show the partial reattachment and secondary stall events displayed by the normal force and pitching moment time histories, although they also reveal secondary stall events not readily visible in the integrated loads. Such events will be discussed shortly, after completing the comparison with the articulated rotor data.

Figure 28 compares some of the stall events on the teetering rotor to stall events from the articulated rotor test. The overall stall boundaries were obtained qualitatively from the pressure distributions presented in Volume II. The two rotor systems present two main differences at the 0.75R station:

(a) The teetering rotor stalls later and possibly at a higher rotor lift level than the articulated rotor. The teetering rotor also appears to reattach sooner, but that is not a clear-cut judgement because of the lack of skin friction gages.

(b) The phase shift between the collapse in leading edge pressure and the attainment of $C_{N_{MAX}}$ is comparable on the two rotors. However, as already mentioned, the lag between maximum attained pitching moment and maximum normal force varies substantially: such lag is about $\Delta\Psi = 20°$ for the teetering rotor and less than $\Delta\Psi = 10°$ for the articulated rotor.

Such difference could be attributed to two causes:

- A difference in the type of stall, since the V23010-1.58 can stall from the leading edge more abruptly than the NACA 0012. (Although at the low Reynolds Number environment of the model rotors very abrupt leading edge stall is not likely to occur. The static data is not sufficiently complete to resolve this question.)

- We have already observed that the articulated rotor undergoes larger excursions in angle of attack than the teetering rotor. Since the time span over which such angle of attack excursions occur is the same, this simply means that stall events on the articulated rotor occur at faster rate than on the teetering rotor.

Unfortunately a true angle of attack comparison cannot be made with the data available.

3.5 Comparison with Articulated Rotor Data (Cont'd)

The time histories of pressure distributions can also be used to visualize how the vortices, generated when the leading edge velocity collapes, sweep over the upper surface from the leading edge to the trailing edge.

Flow visualization studies, such as reported in Reference 5, for sections in sinusoidal pitch oscillation, show that as the lift is lost because of leading edge separation, the circulation around the airfoil is adjusted by shedding a vortex. Such vortex travels along the airfoil at a velocity which is a function of airfoil reduced frequency. On the surface of the airfoil the passing of such vortices will cause a measurable variation in velocity sweeping along the chord. Figure 29 illustrates the propagation of the velocity peak due to the vortex associated with the main stall event. It can be seen that the velocity of propagation, i.e., the slope of the curves, does not vary much with rotor lift, and that the most significant lift effect is the azimuth angle at which the vortex is shed.

Going back to the pressure time histories, it is worth making one more observation. The pressure data reveal a much more complex series of events than could be seen from the integrated normal force and pitching moment time histories. Essentially, the integraced loads show two stall events, referred to so far as "double stall." However, Figures 25, 26 and 27 show that there is a partial collapse in the leading edge pressure anywhere from 30 to 50 degrees in azimuth before reaching $C_{N_{MAX}}$. Even such incomplete stall, occurring at $\dot{\alpha} > 0$, sheds a vortex causing a detectable pressure fluctuation over the airfoil surface.

Figure 27, showing the pressure time histories for the highest rotor lift level in this run, reveals that there are additional secondary fluctuations which could be associated to vortex shedding before flow reattachment. (On the articulated rotor such secondary fluctuations were observable from the integrated loads time histories.)

Now we have four clearly identifiable stall events, two of which are clearly visible from the integrated loads.

(a) A temporary loss in lift, occurring at $190° < \psi < 220°$ while the angle of attack is changing at a positive rate of change ($\dot{\alpha} > 0$).

3.5 Comparison with Articulated Rotor Data (Cont'd)

(b) The main stall event, in the course of which the normal force attains the largest value. In all probability this stall also occurs at $\dot{\alpha} > 0$. In this sequence of test points $C_{N_{MAX}}$ was always reached at $\Psi < 270°$

(c) A secondary stall clearly detectable from the integrated loads occurring at $\dot{\alpha} < 0$. This stall follows the same sequence of events as the main stall. For instance, at the highest rotor lift (test point 17.07) this stall still follows the same sequence illustrated in Figure 28, i.e., first the collapse in leading edge suction (Ψ = 310°), then the attainment of a secondary $C_{N_{MAX}}$ (Ψ = 325°), and finally the attainment of the second maximum pitching moment coefficient, (Ψ = 335°).

(d) A fourth stall fluctuation, at $\dot{\alpha} < 0$, evident only at the highest rotor lift (Test Point 17.07). This last event (at Ψ = 345°) is followed very closely by complete reattachment in the first quadrant.

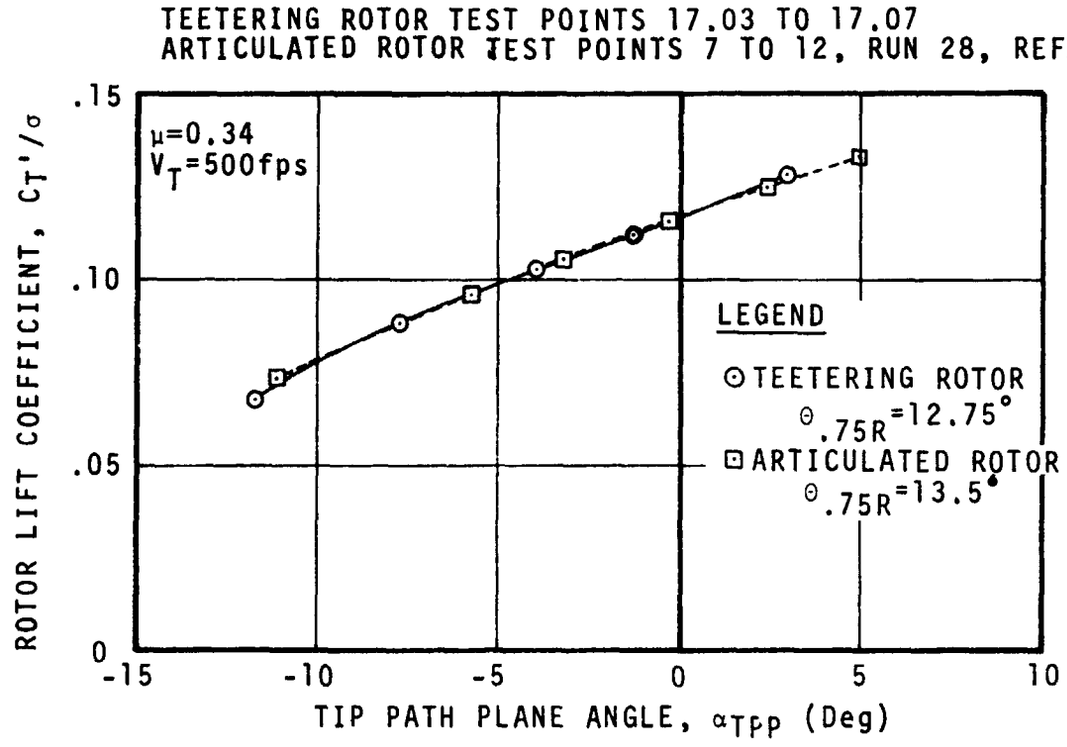

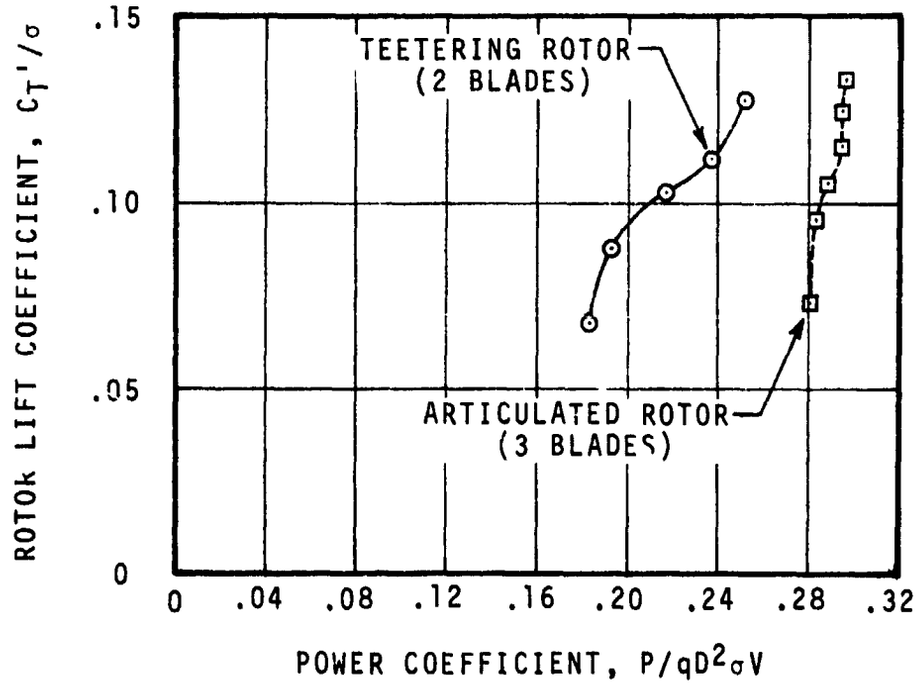

FIGURE 18 MODEL ROTOR PERFORMANCE DATA IN FORWARD FLIGHT. COMPARISON BETWEEN TEETERING AND ARTICULATED ROTOR.

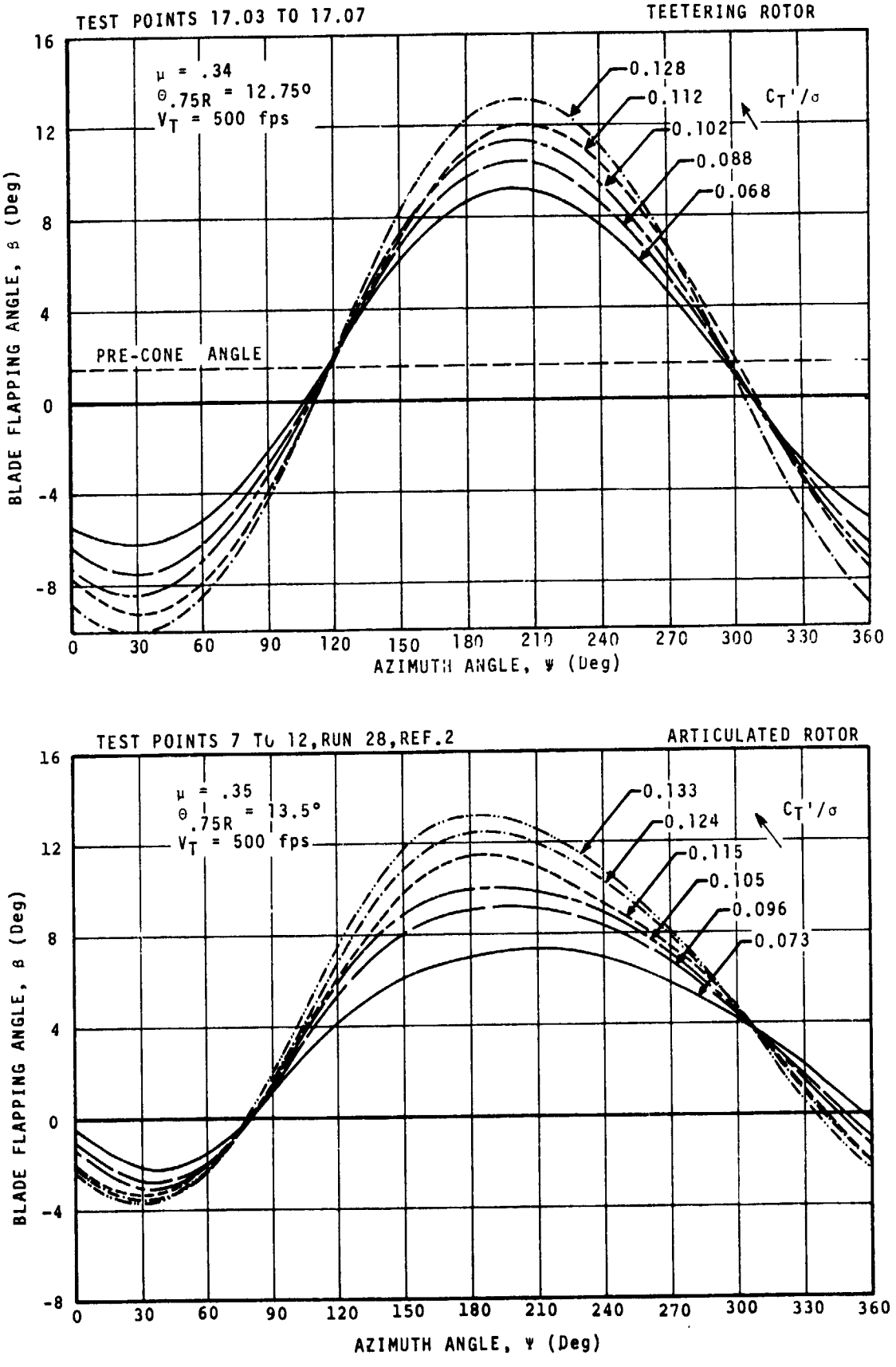

FIGURE 19 MEASURED ROOT FLAPPING ANGLE. COMPARISON BETWEEN TEETERING AND ARTICULATED ROTORS

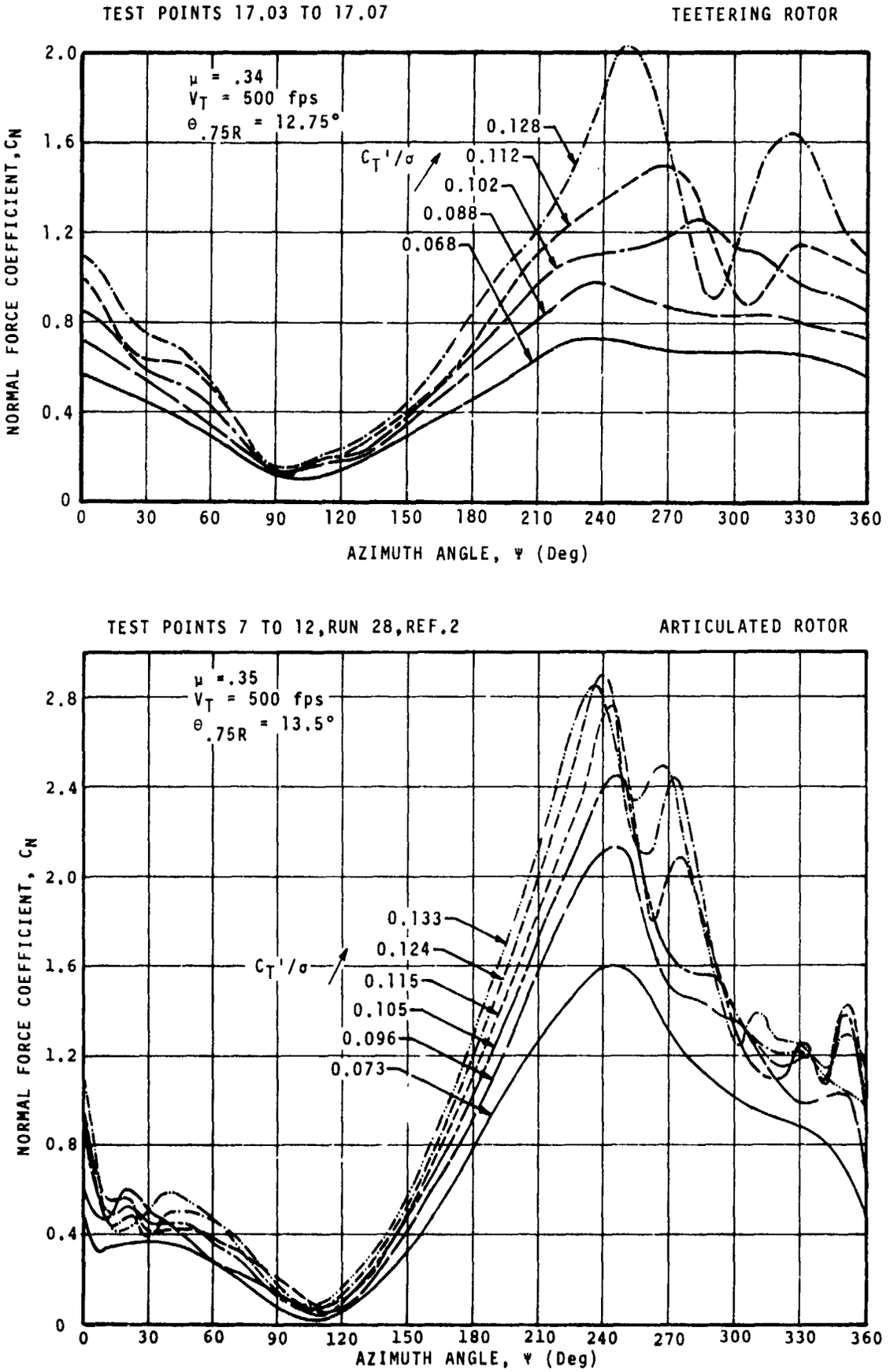

FIGURE 20 NORMAL FORCE COEFFICIENTS OBTAINED FROM INTEGRATED PRESSURES AT r/R=0.75. COMPARISON BETWEEN TEETERING AND ARTICULATED ROTORS

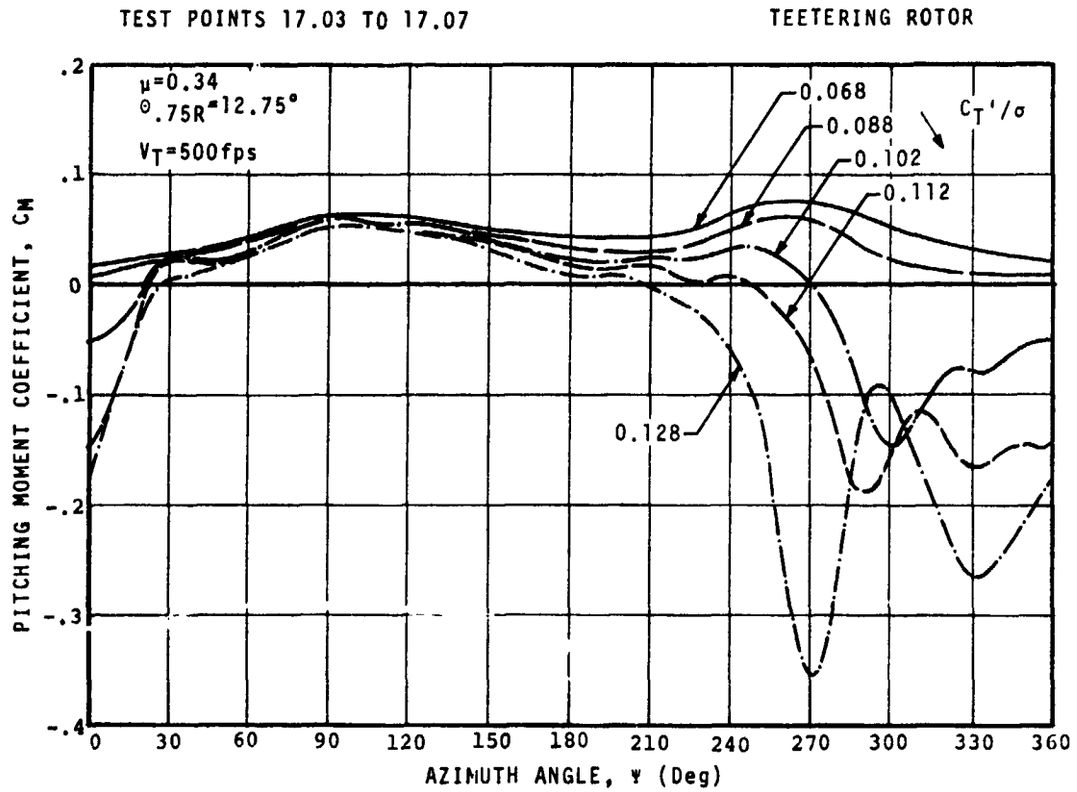

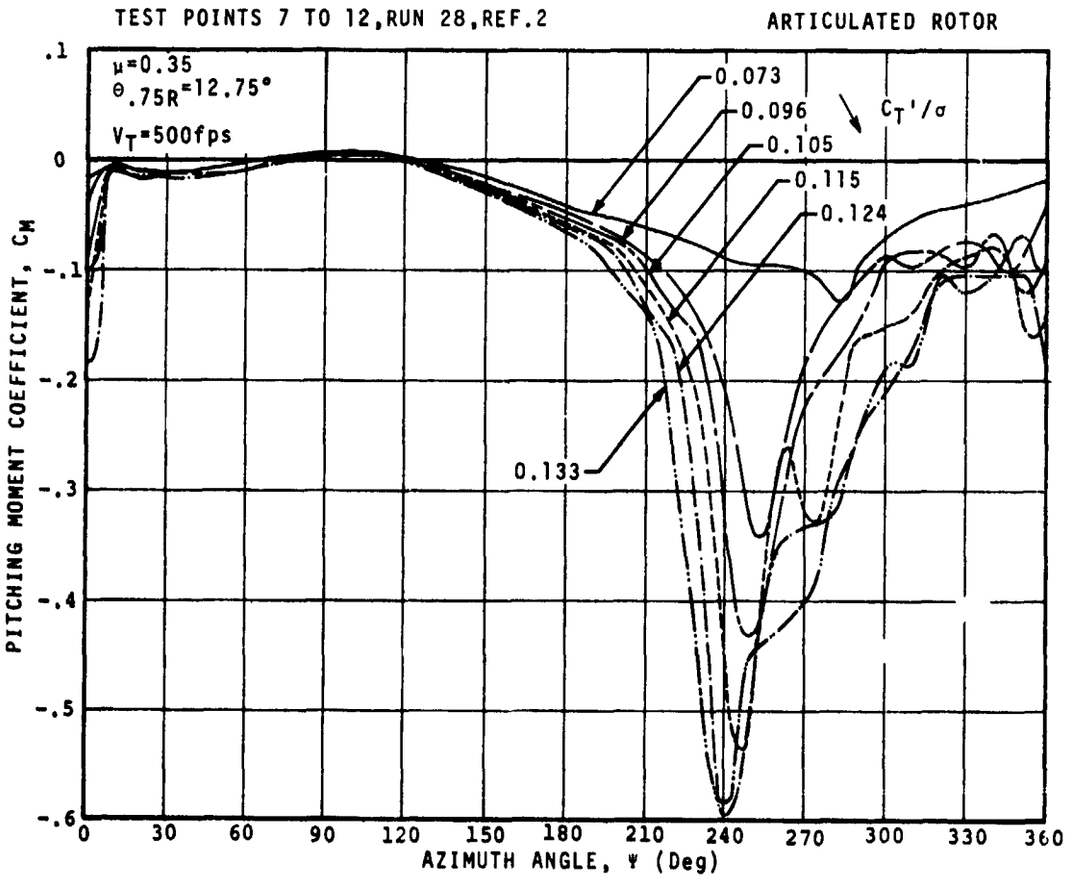

FIGURE 21 PITCHING MOMENT COEFFICIENTS OBTAINED FROM INTEGRATED PRESSURES AT r/R=0.75. COMPARISON BETWEEN TEETERING AND ARTICULATED ROTORS

SPAN STATION: 0.75R

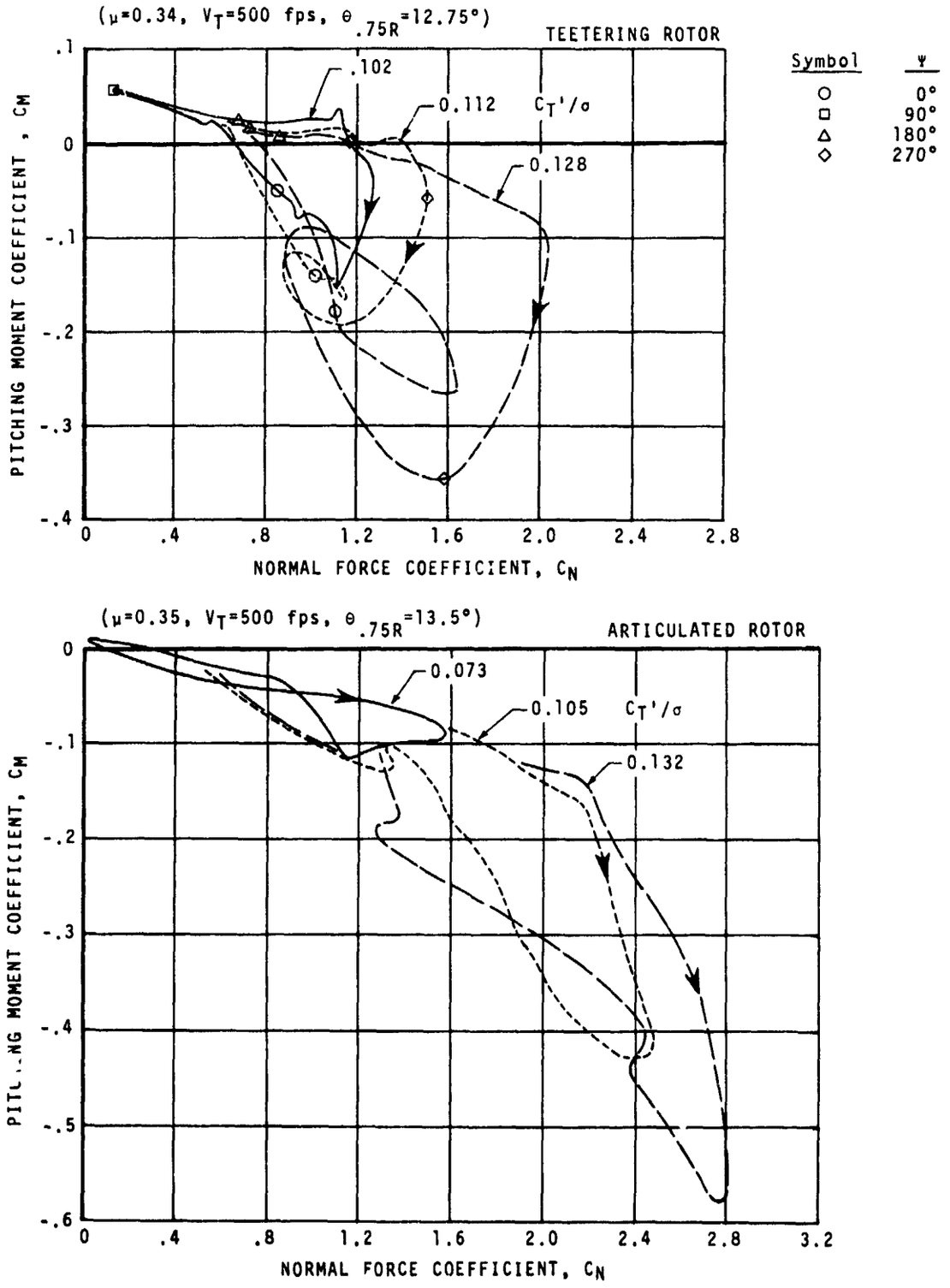

FIGURE 22 COMPARISON BETWEEN TEETERING AND ARTICULATED ROTOR LOADS DURING STALL

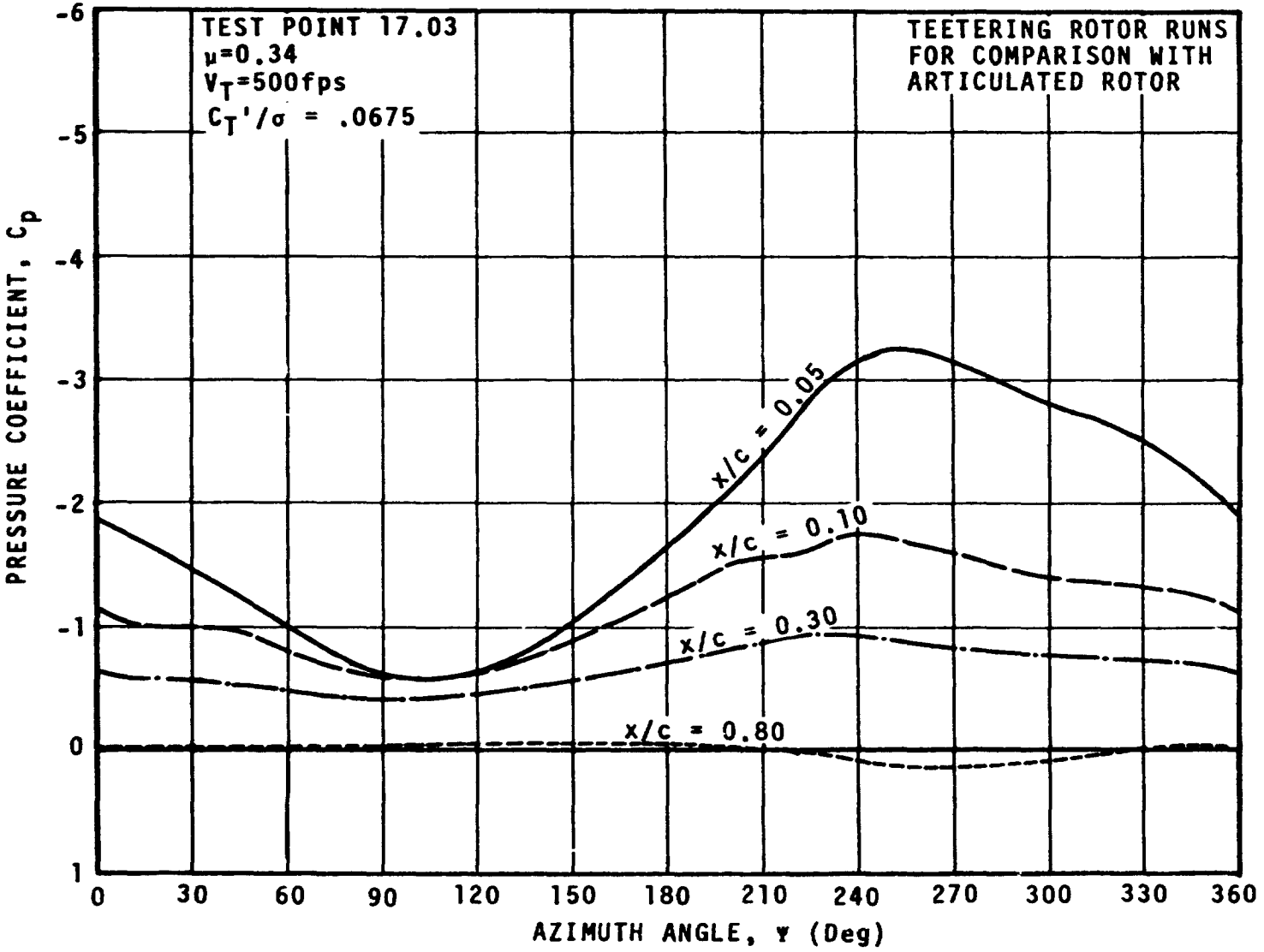

FIGURE 23 TIME HISTORIES OF UPPER SURFACE PRESSURES MEASURED AT r/R=0.75

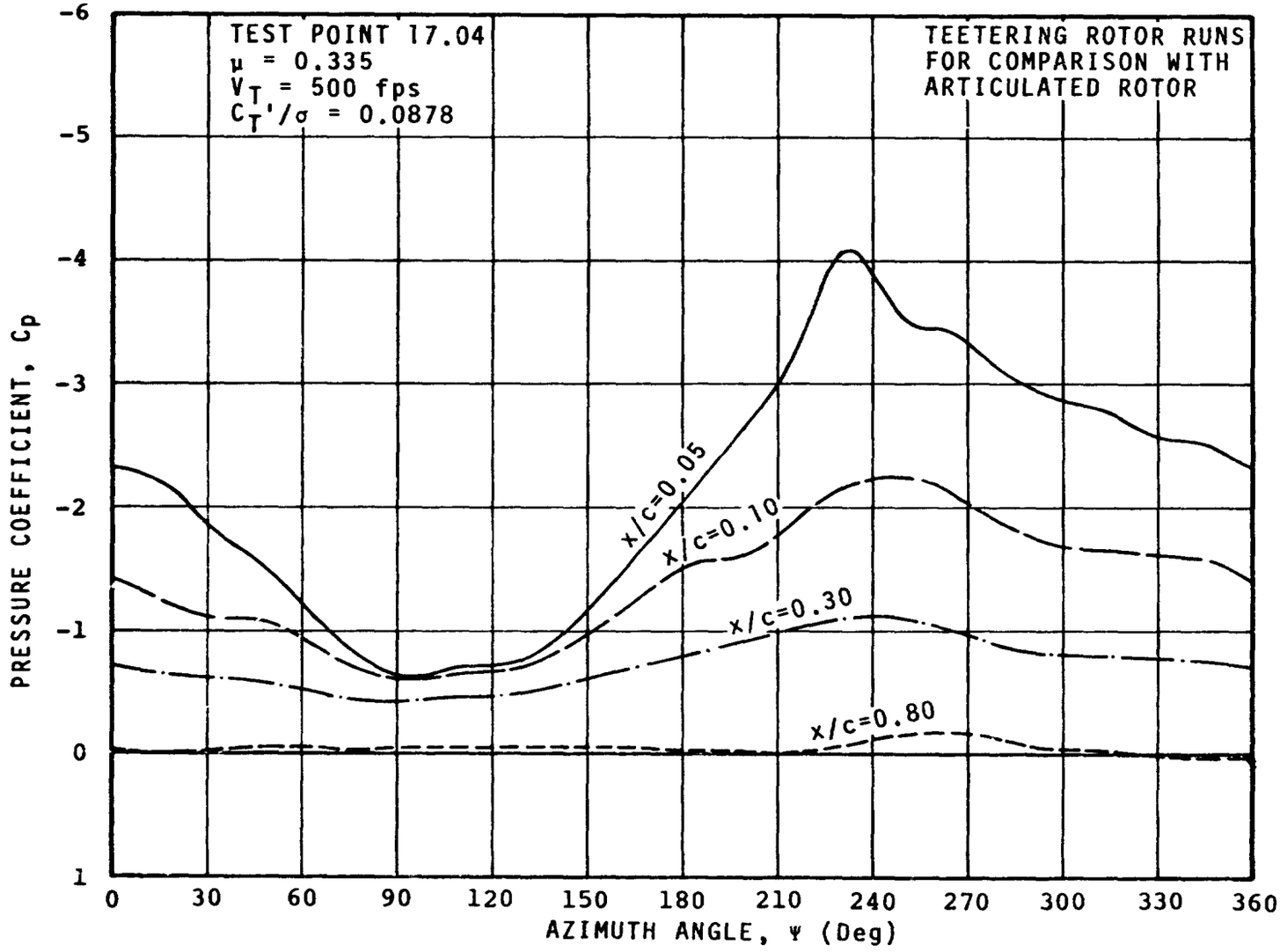

FIGURE 24 TIME HISTORIES OF UPPER SURFACE PRESSURES MEASURED AT r/R=0.75

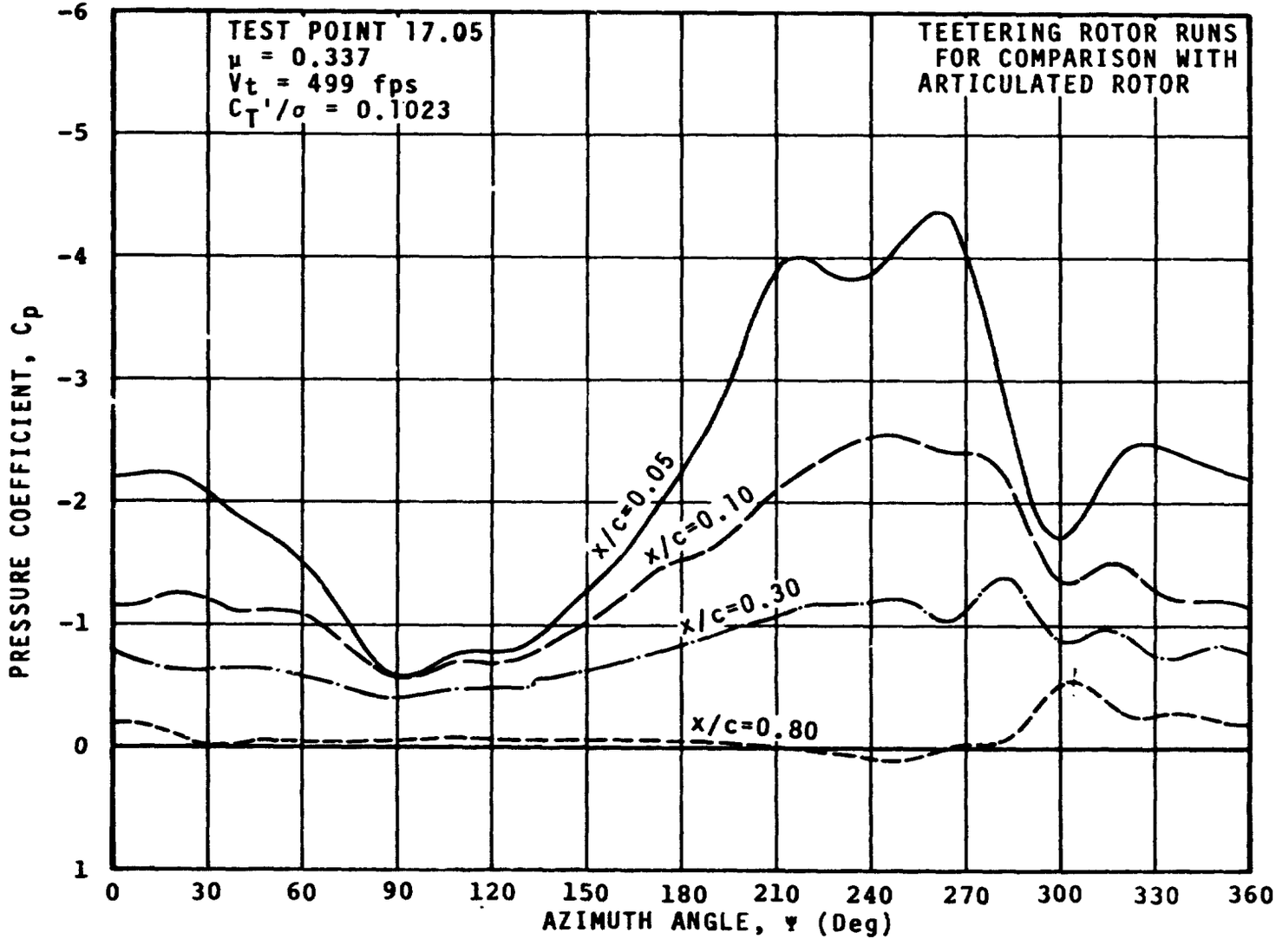

FIGURE 25 TIME HISTORIES OF UPPER SURFACE PRESSURES MEASURED AT r/R=0.75

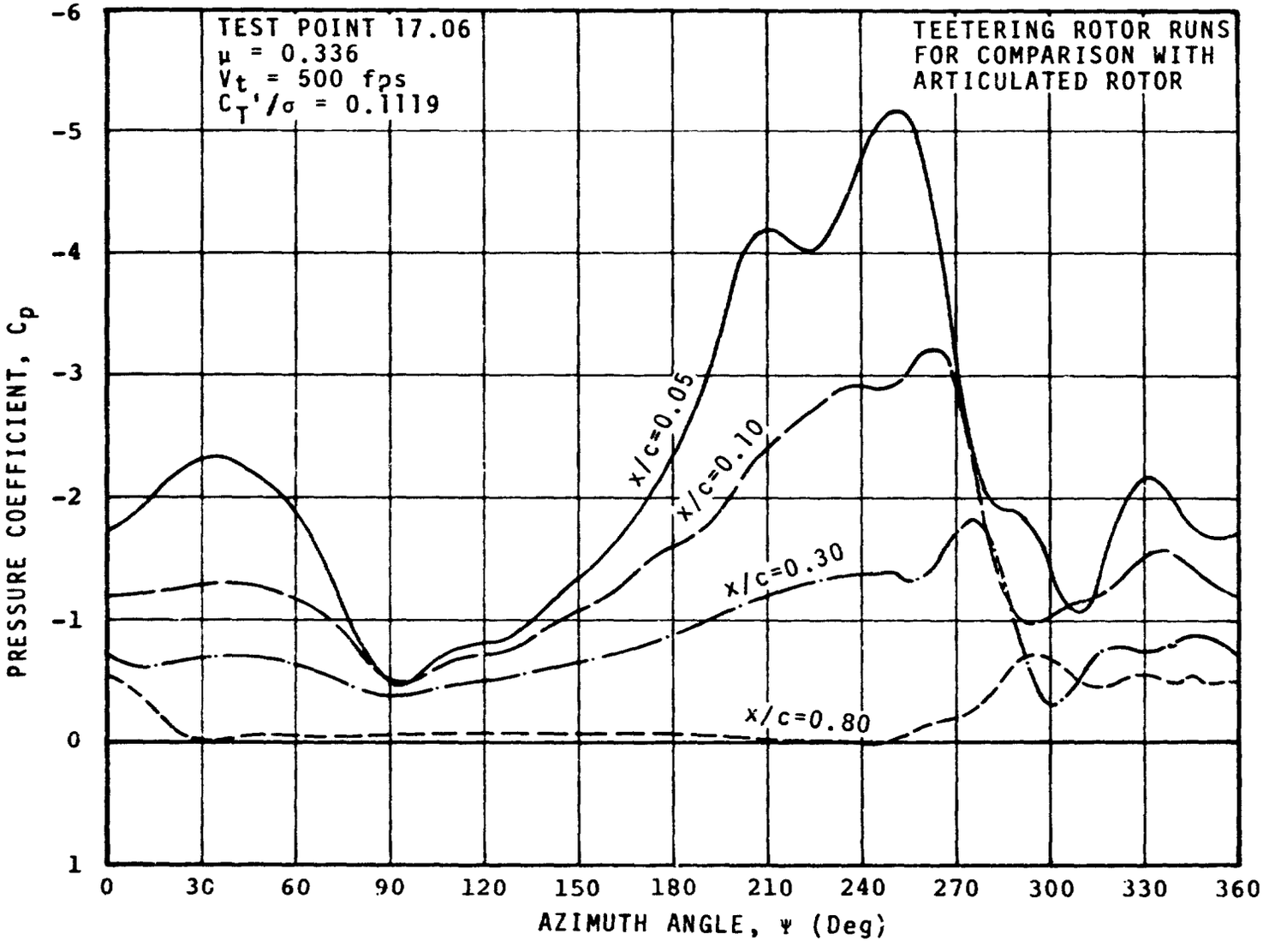

FIGURE 26 TIME HISTORIES OF UPPER SURFACE PRESSURES MEASURED AT r/R=0.75

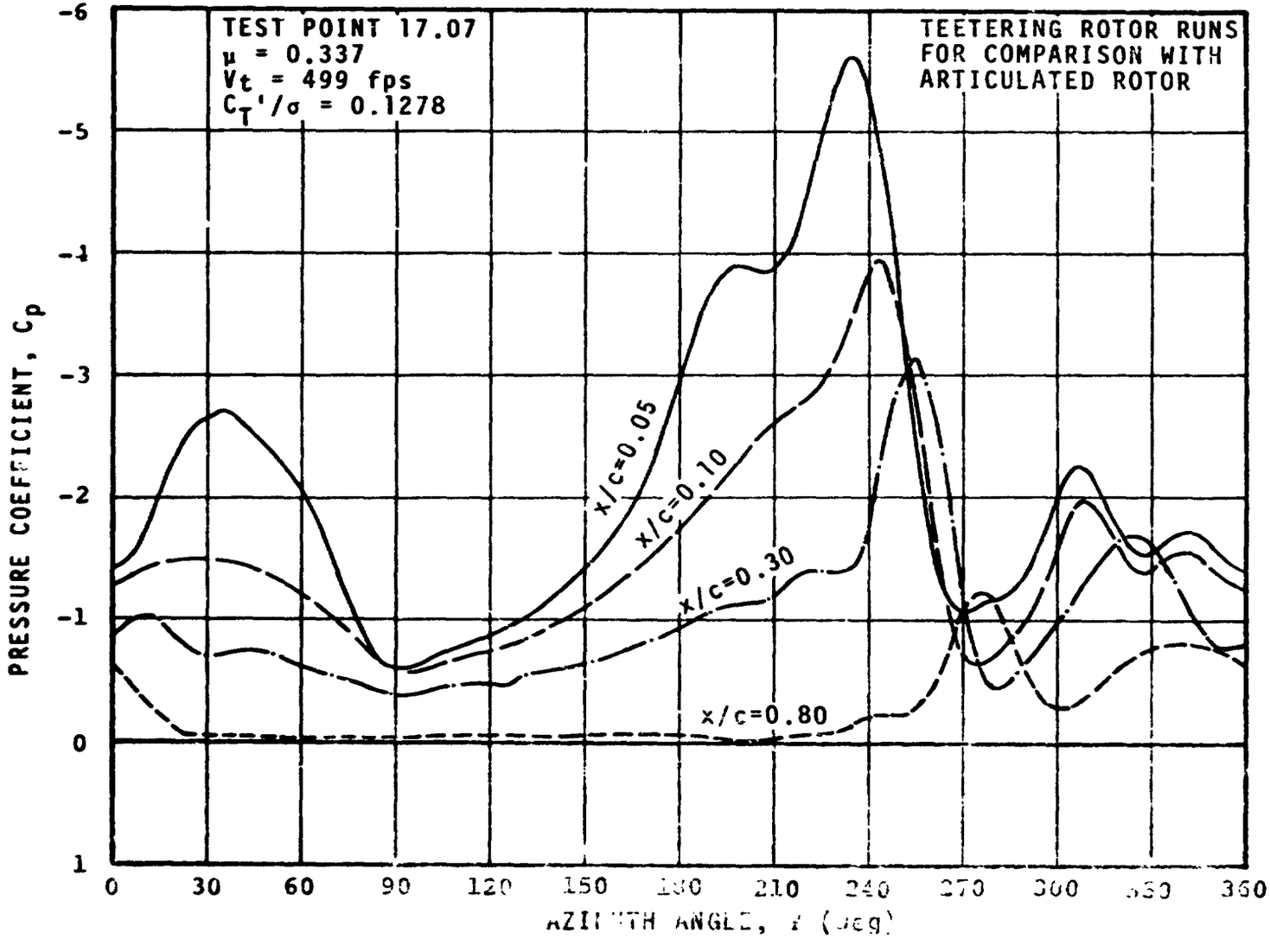

FIGURE 27 TIME HISTORIES OF UPPER SURFACE PRESSURES MEASURED AT r/R=0.75

μ=0.34, V_T=500 FPS, $\theta_{.75R}$=12.75° (TEETERING ROTOR)
$\theta_{.75R}$=13.5° (ARTICULATED ROTOR)

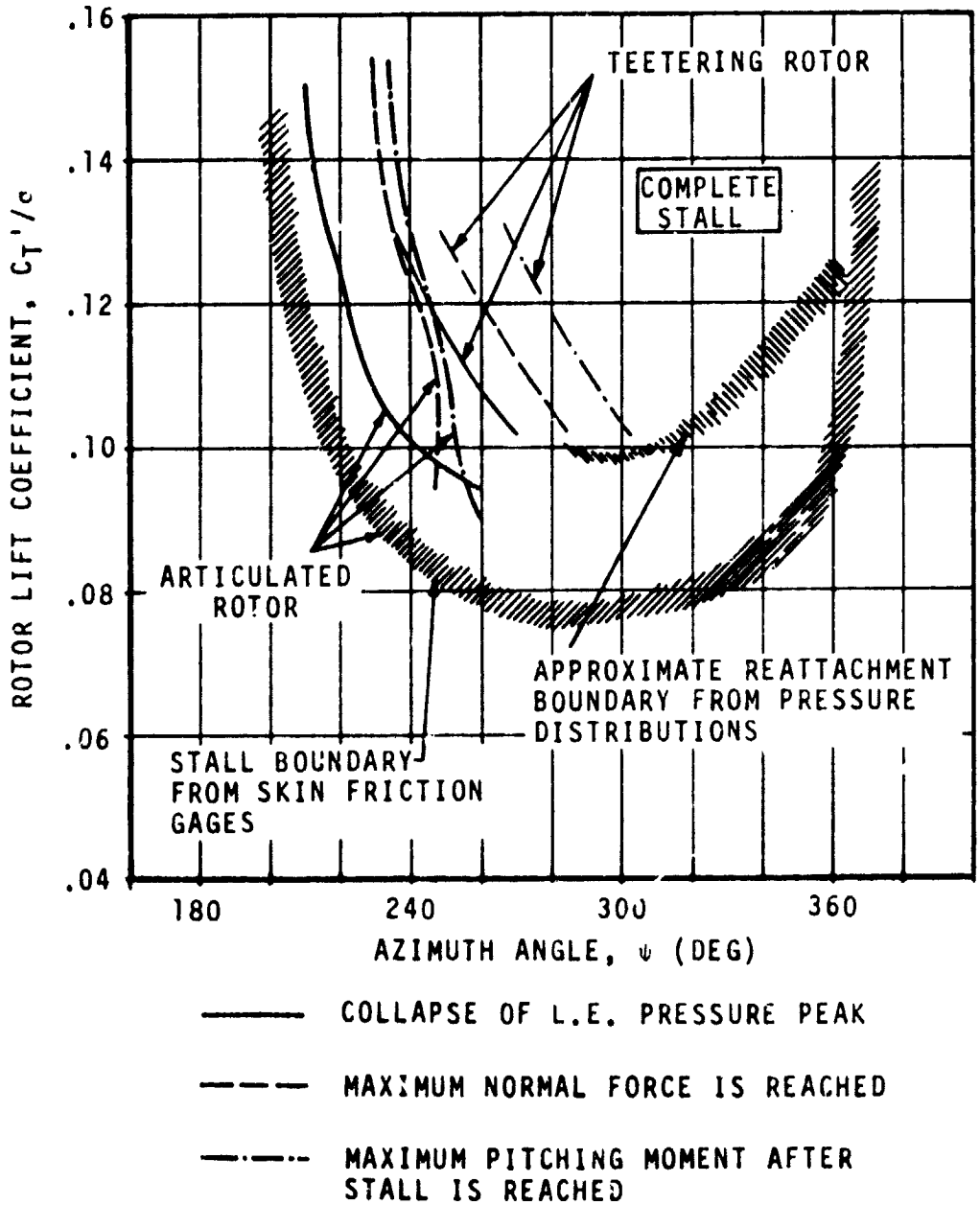

FIGURE 28 COMPARISON OF STALL BOUNDARIES OF TEETERING AND ARTICULATED ROTORS

DETERMINED:
A) FROM TIME HISTORIES OF MEASURED LOCAL PRESSURES
B) FOR THE PRIMARY STALL EVENT ONLY

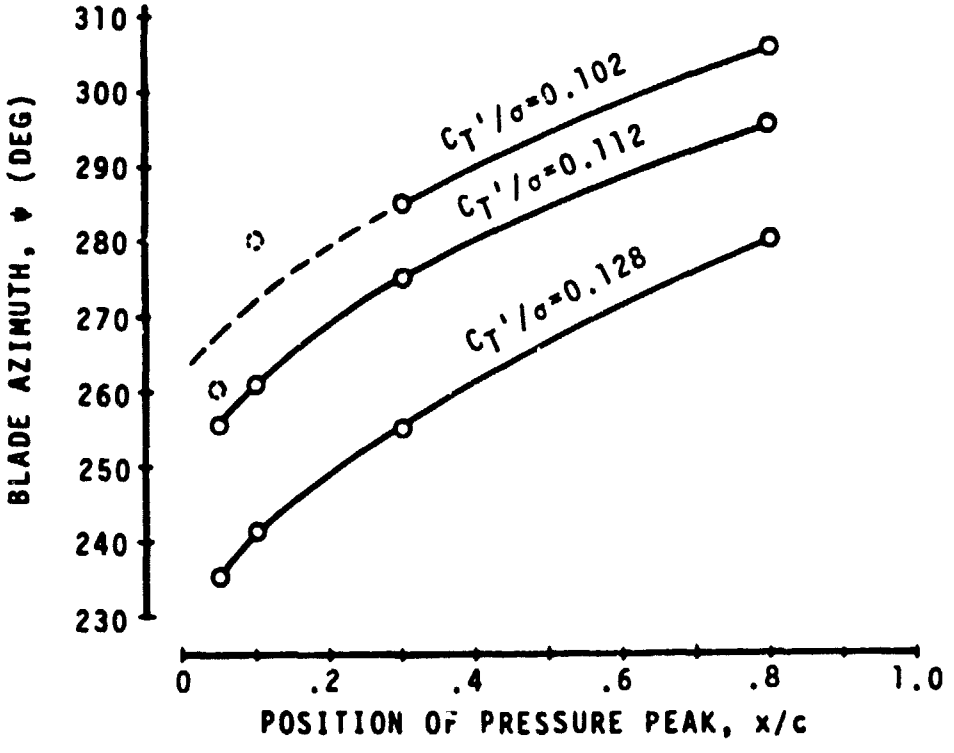

FIGURE 29 PATH OF PEAK PRESSURE COEFFICIENTS FOLLOWING THE COLLAPSE OF LEADING EDGE SUCTION.

3.6 Variation in Propulsive Force at Constant Lift

(Test Points 17.17 to 17.20, μ = .34, V_T = 500 fps, C_T'/σ = .075)

In this run the tip path plane was progressively tilted back from the position for highest propulsive force (T.P. 17.17) through nearly zero (T.P. 17.19) and finally a negative propulsive force level (T.P. 17.20).

Figure 30 shows performance data, Figure 31 flapping angles, Figures 32 through 35 the time history of the pressure coefficients at the .05, .10, .30 & .80 chordwise stations. The only notable event to be seen in the pressure time histories is the unstable behavior of the pressure coefficient at x/c = .10 over the retreating side.

The objective of this run was to observe the effect of variations in the rate of change of angle of attack ($d\alpha/dt$) in absence of stall. No such effect was visible in the data, but because of instrumentation problems too many transducers were out of order at the time these test points were taken, so that the integration for normal force and pitching moment could not be carried out.

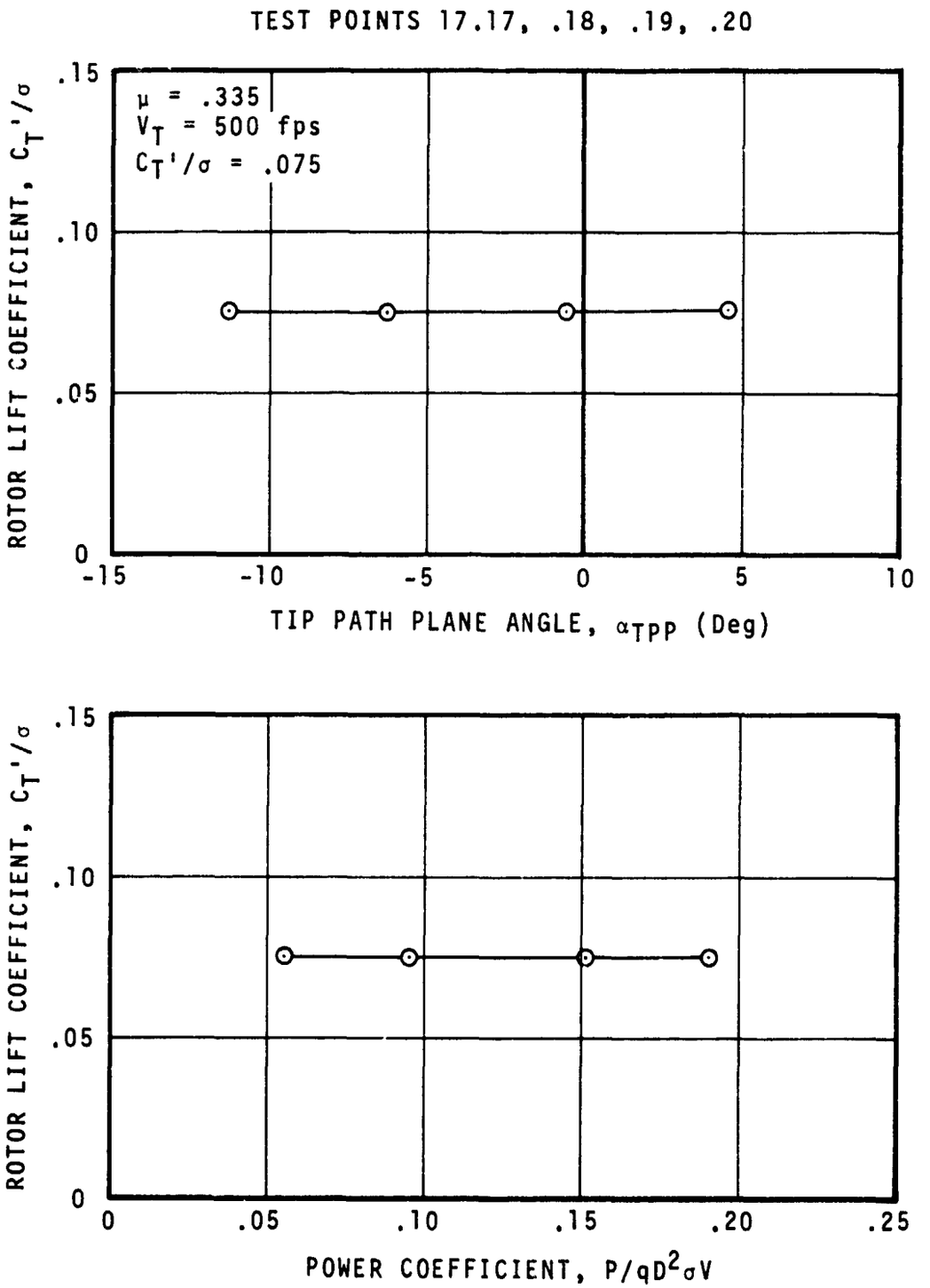

FIGURE 30 MODEL ROTOR PERFORMANCE DATA IN FORWARD FLIGHT. VARIATION IN PROPULSIVE FORCE AT CONSTANT LIFT.

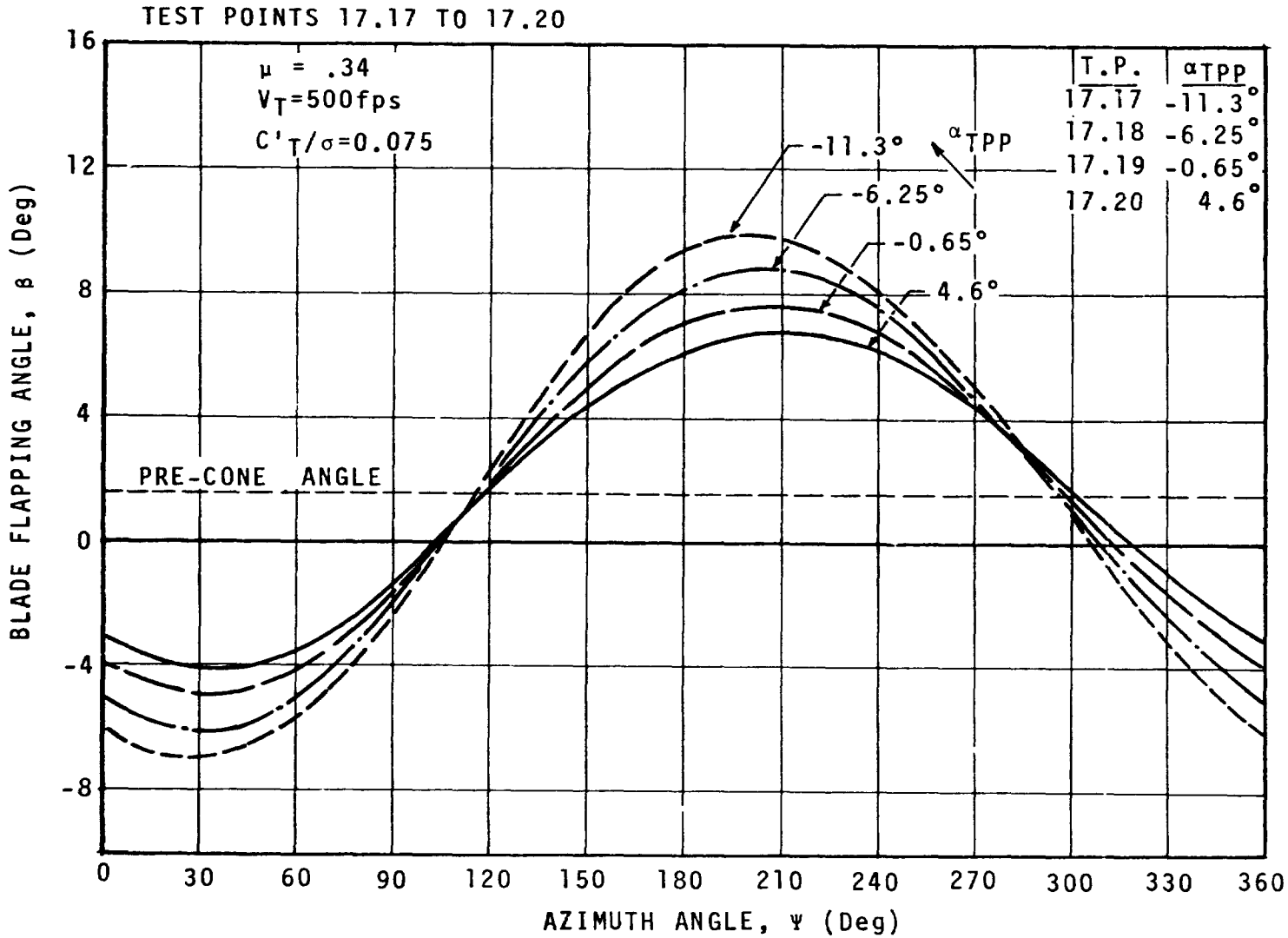

FIGURE 31 MEASURED ROOT FLAPPING ANGLE. VARIATION IN PROPULSIVE FORCE AT CONSTANT LIFT.

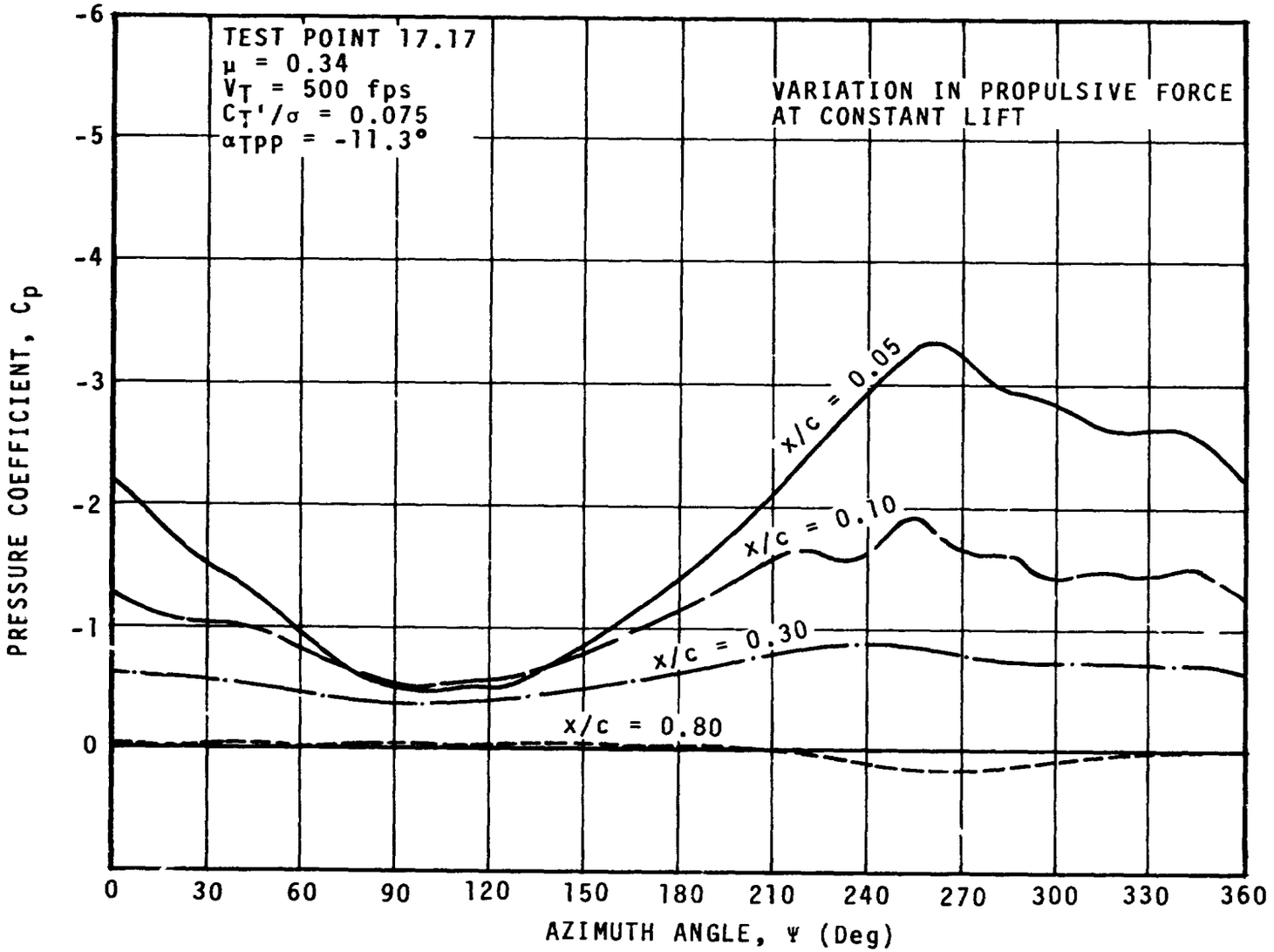

FIGURE 32 TIME HISTORIES OF UPPER SURFACE PRESSURES MEASURED AT r/R=0.75

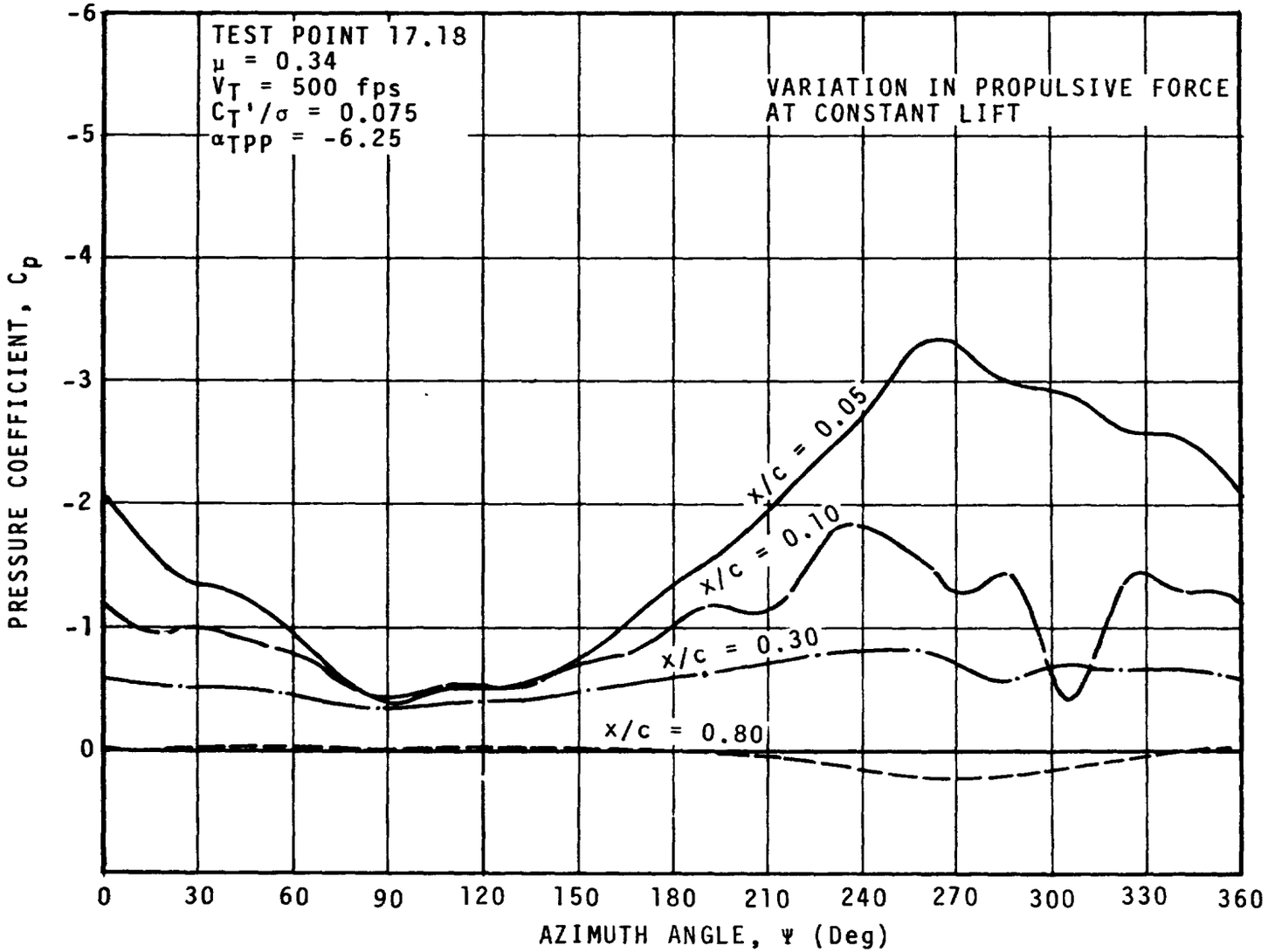

FIGURE 33 TIME HISTORIES OF UPPER SURFACE PRESSURES MEASURED AT r/R=0.75

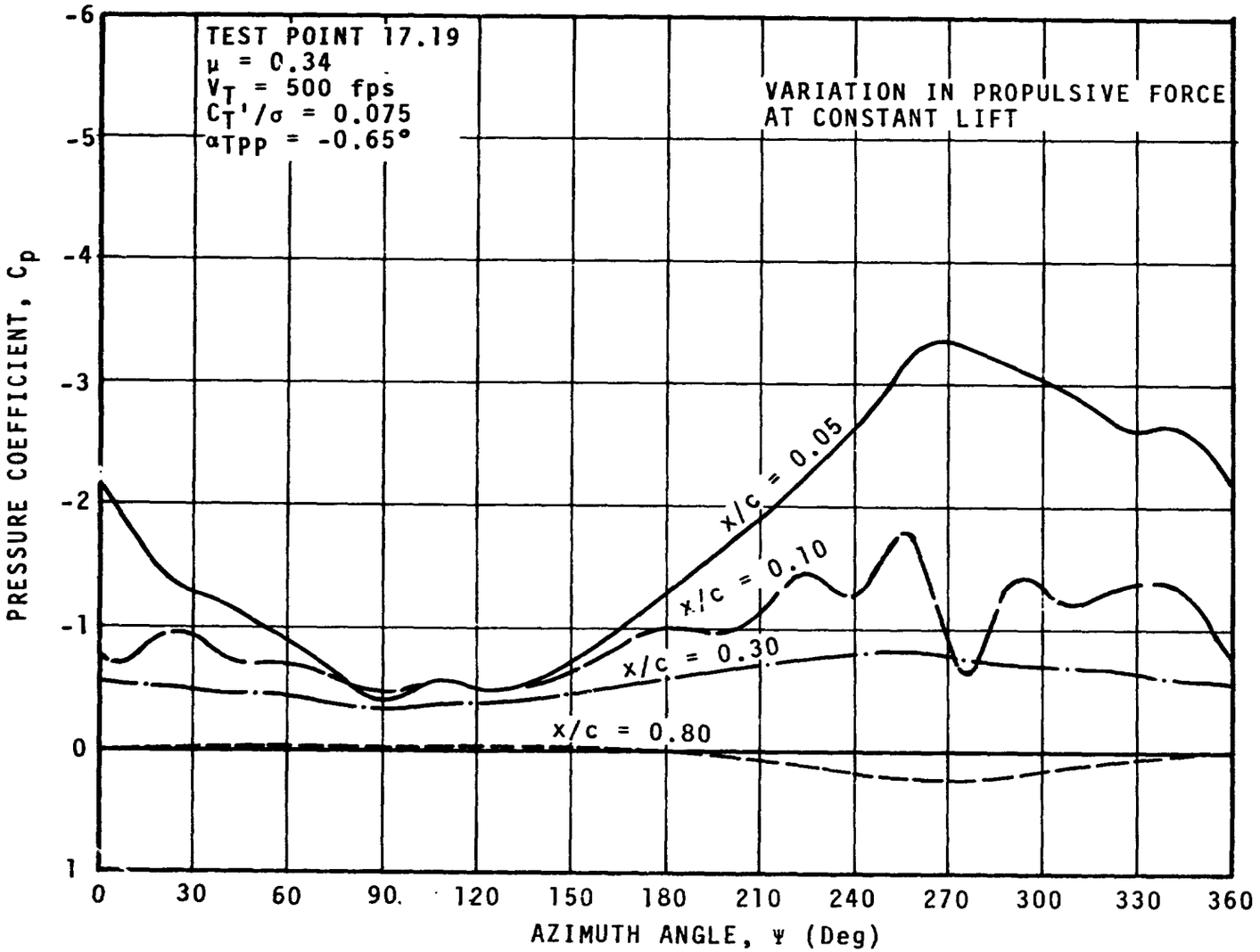

FIGURE 34 TIME HISTORIES OF UPPER SURFACE PRESSURES MEASURED AT r/R=0.75

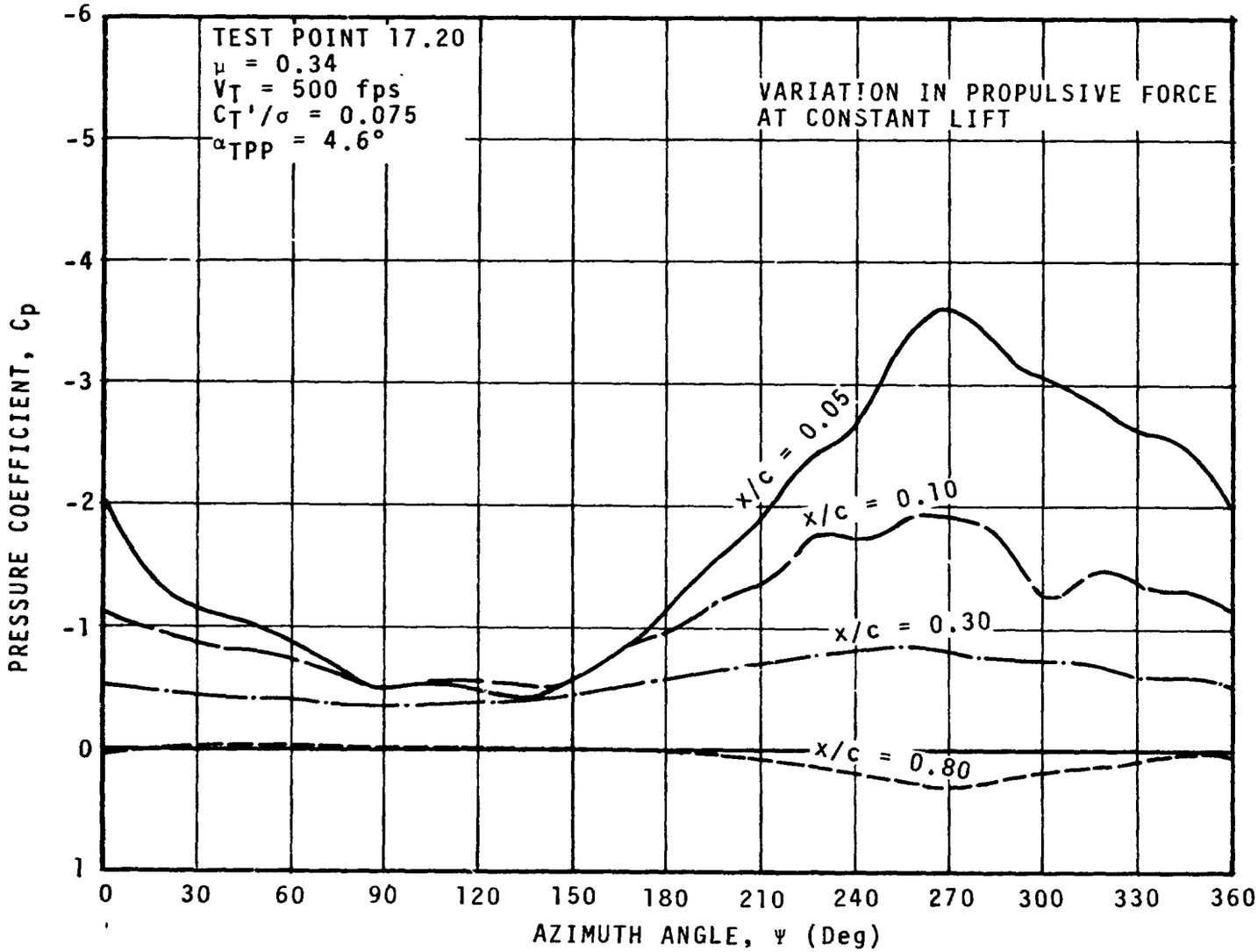

FIGURE 35 TIME HISTORIES OF UPPER SURFACE PRESSURES MEASURED AT r/R=0.75

3.7 Collective Pitch Variation of Constant Shaft Angle

(Test Points 18.07 to 18.11, μ = .143, V_T = 285 fps, α_S = -10.1°)

This test run covers T.P. 18.07 through 18.11. Part of the conditions selected was close to one set of conditions presented by Landgrebe in Reference 6. Conditions at much higher rotor lift were also included.

Again, because of instrumentation problems, no integrated loads are presented, but the time histories of selected upper surface pressures are sufficient to draw at least some conclusions. Performance data is shown in Figure 36, blade flapping in Figure 37, and the pressure time histories in Figures 39 through 43.

All the test points taken in this run include some degree of stall. The stall behavior ranges from simple stall, at the lower thrust levels, to a more complex series of fluctuations indicating three or four vortex shedding events. Such vortices sweep over the upper surface and cause substantial velocity fluctuations in the trailing edge region.

Actually we could divide the stall events into two categories, one indicating the shedding of several vortices, as evidenced by the velocity build up at the trailing edge, and the other characterized by a collapse in the leading edge pressures followed by the shedding of a very weak vortex, if it is a vortex at all and not just a separation "bubble" which is still fairly evident at 10% of chord, but the effect of which vanishes beyond the 30% chord station.

While the collapse of the leading edge velocities is a clear indication of stall, it is not clear what criteria should be used for complete reattachment. Other tests availed themselves of skin friction measurements for such purpose. At the lower thrust levels (T.P. 18.07 and 18.08, with C_T'/σ = .1014 and .1116 respectively) we can probably assume that the leading edge pressure peak following the collapse of the first peak is actually a sign of reattachment. This reattachment occurs later and later with increasing rotor lift, until, at the highest lift levels, it takes place only when the blade has moved into the first quadrant. The re-establishment of low velocities at the trailing edge (x/c = 0.80) qualitatively agrees with the re-establishment of high leading edge velocities, and it indicates that the flow is fully attached again. These events are shown in Figure 38, with a comparison to the

stall boundary measured by Landgrebe in Reference 6 at similar conditions. The one difference between this data and Landgrebe's data is that while in Landgrebe's data the most delayed reattachment was in the neighborhood of $\Psi = 20°$, the data for test point 18.11 shows reattachment somewhere between $40° < \Psi < 60°$, and for test point 18.10 at $\Psi \approx 30°$

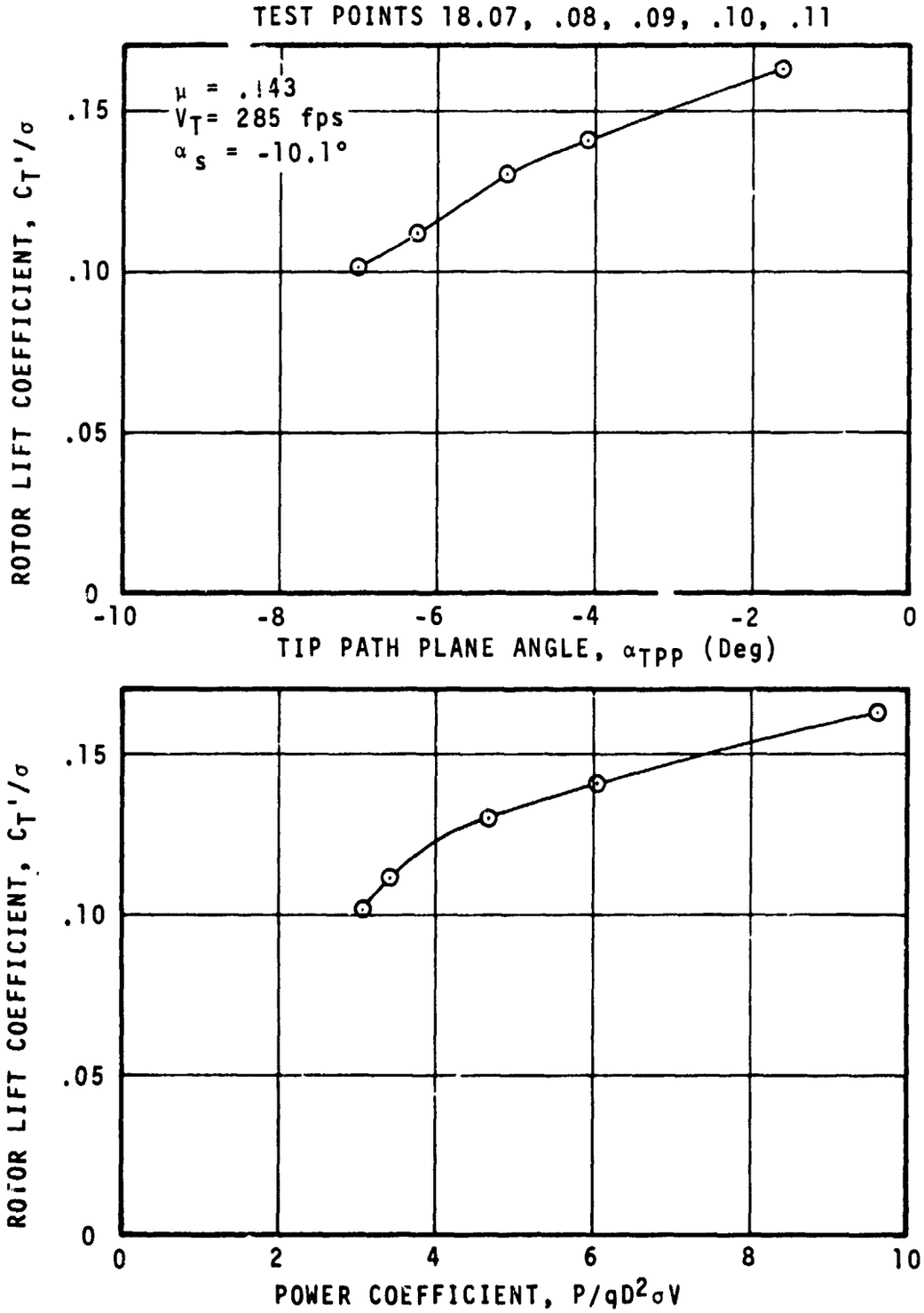

FIGURE 36 MODEL ROTOR PERFORMANCE DATA IN FORWARD FLIGHT. COLLECTIVE PITCH VARIATION AT CONSTANT SHAFT ANGLE.

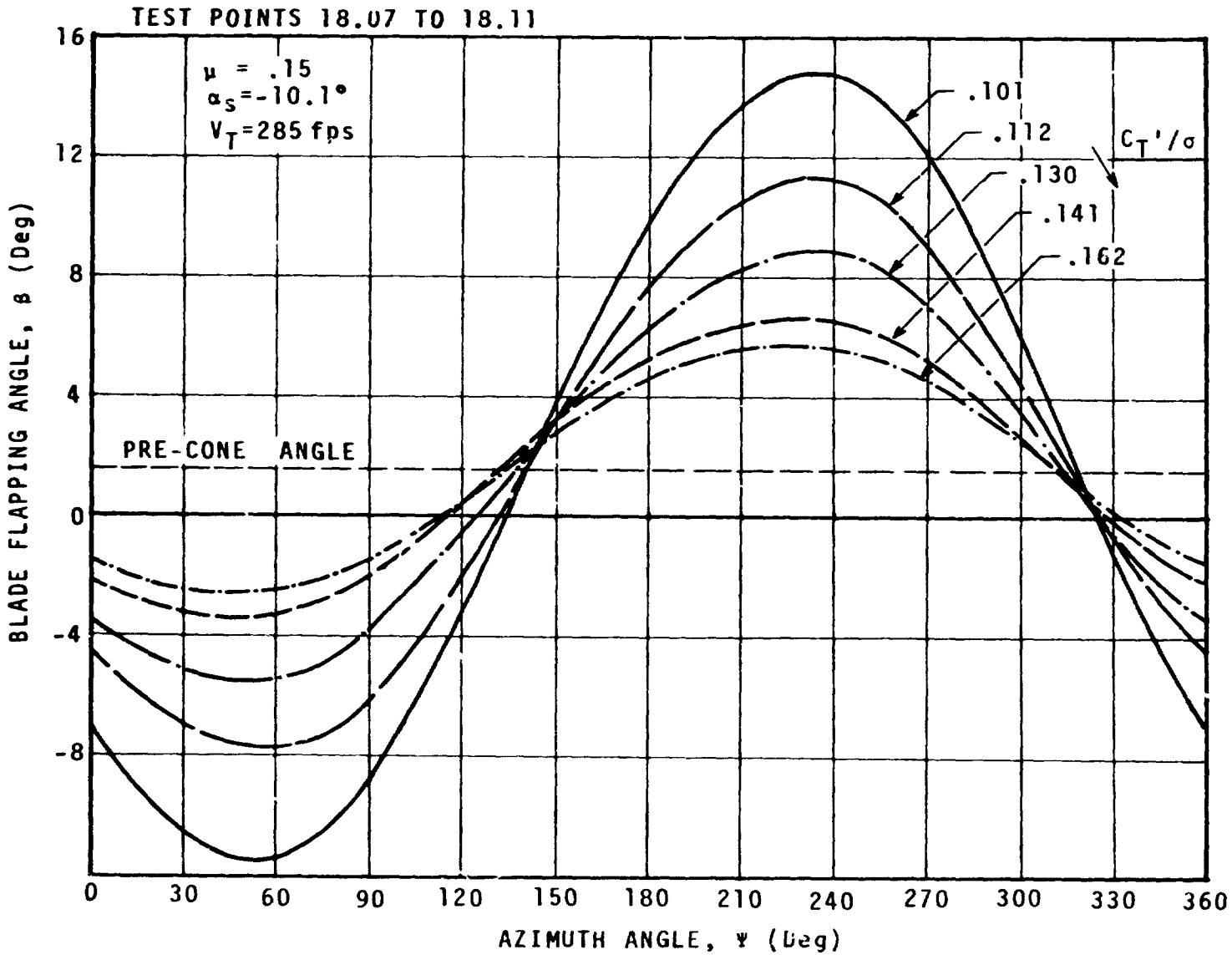

FIGURE 37 MEASURED ROOT FLAPPING ANGLE. COLLECTIVE PITCH VARIATION AT CONSTANT SHAFT ANGLE.

TEST POINTS 18.07 to 18.11
μ = 0.143
V_T = 285 fps
α_s = -10.1°

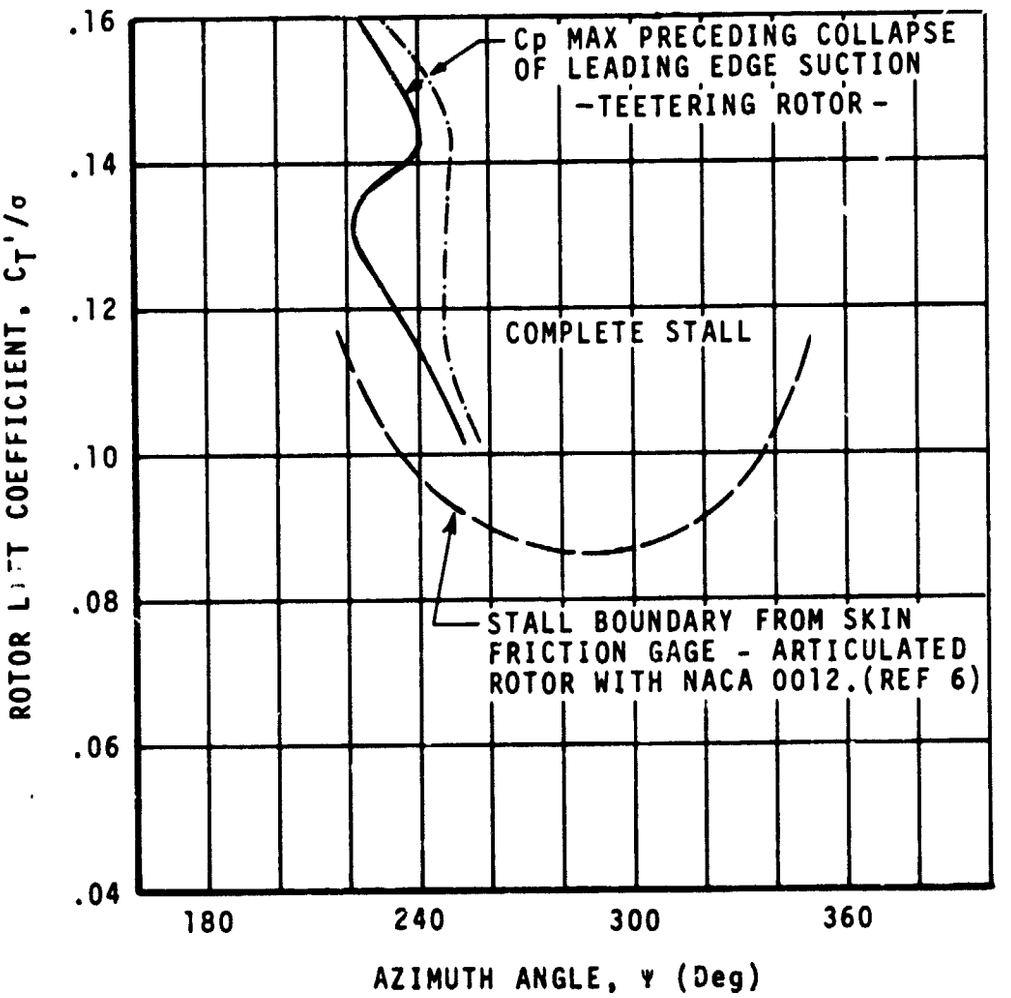

FIGURE 38 COLLECTIVE PITCH VARIATION AT CONSTANT SHAFT ANGLE. APPROXIMATE STALL BOUNDARIES.

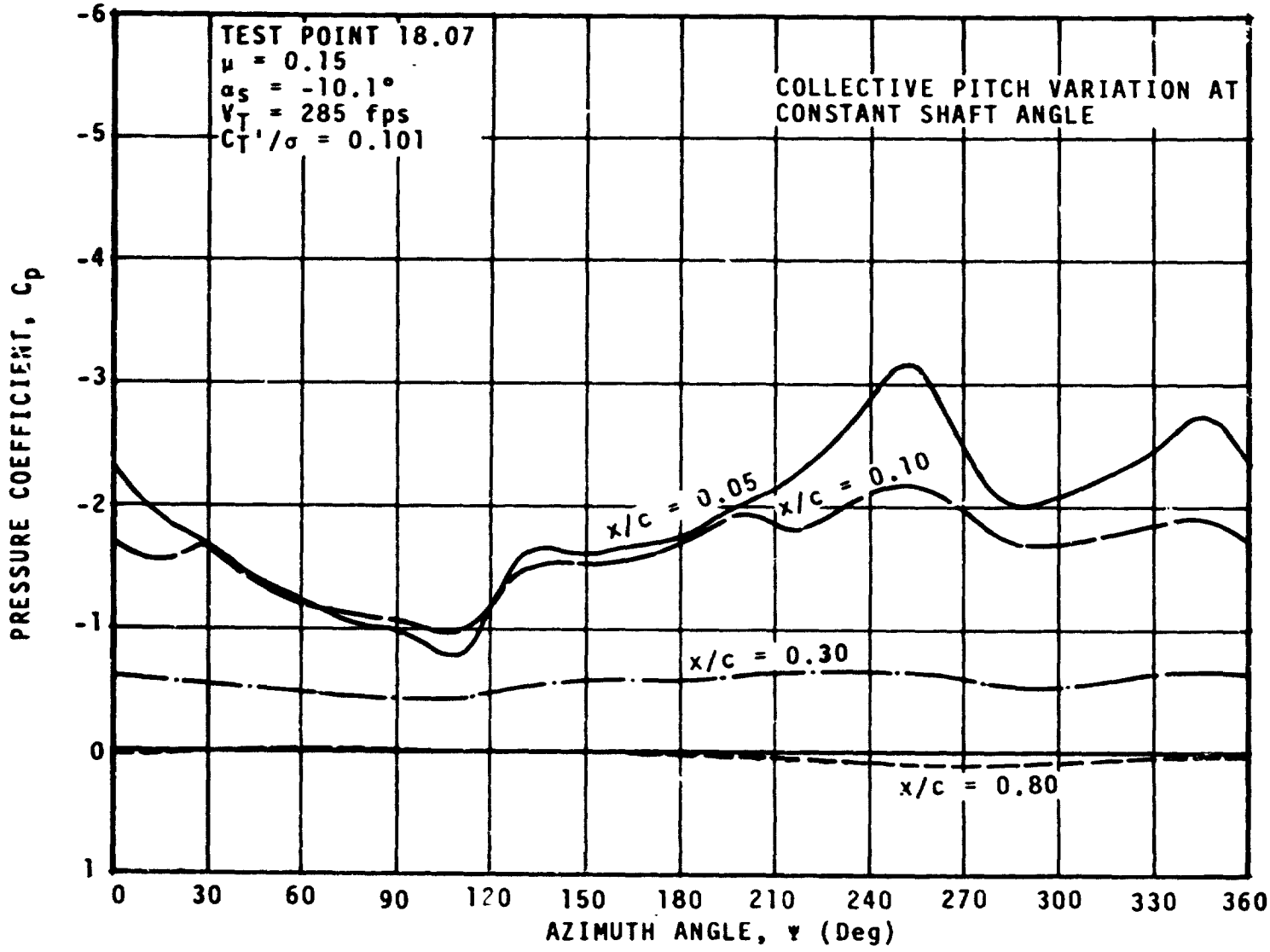

FIGURE 39 TIME HISTORIES OF UPPER SURFACE PRESSURES MEASURED AT r/R = 0.75

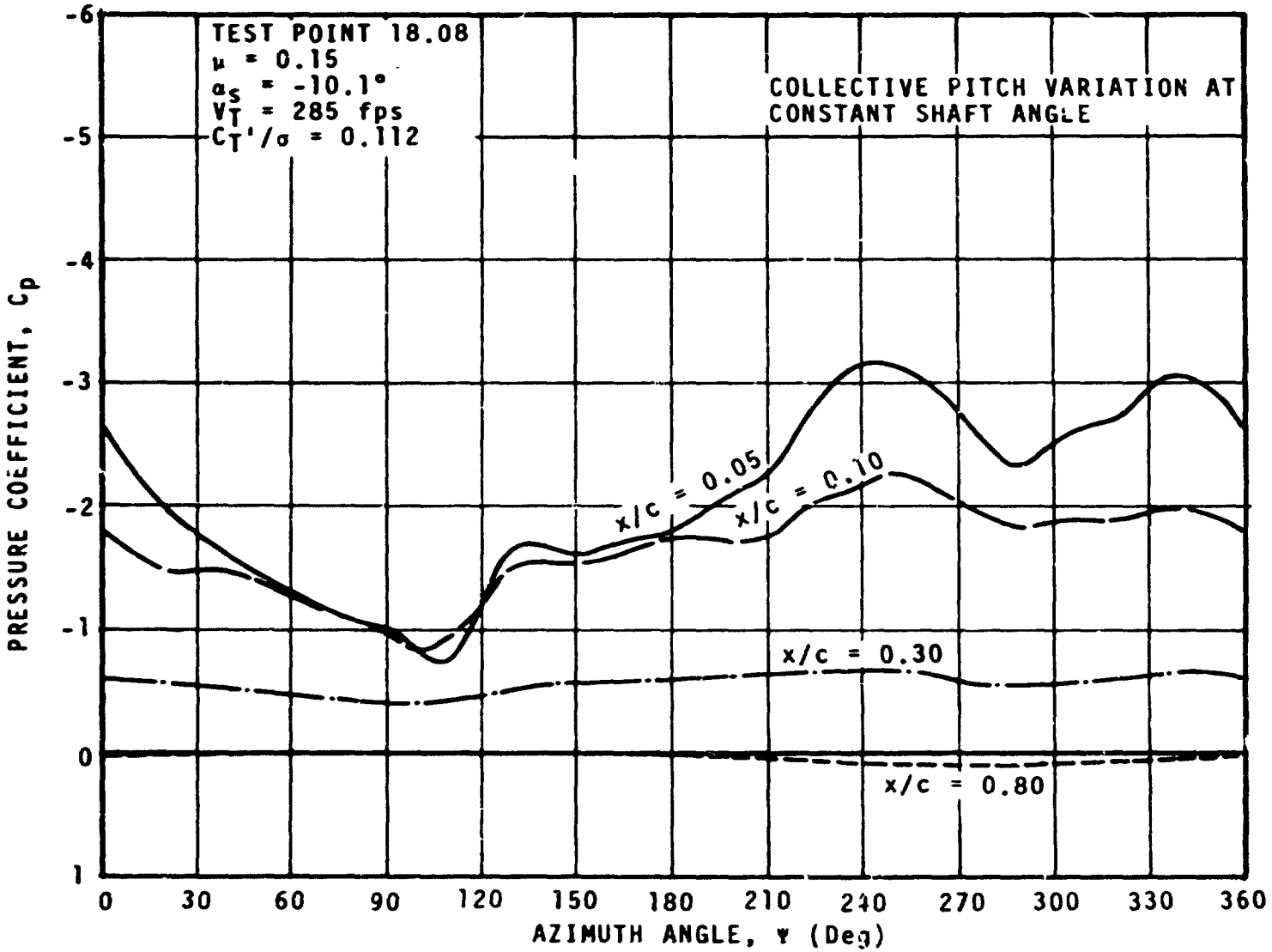

FIGURE 40 TIME HISTORIES OF UPPER SURFACE PRESSURES MEASURED AT r/R = 0.75

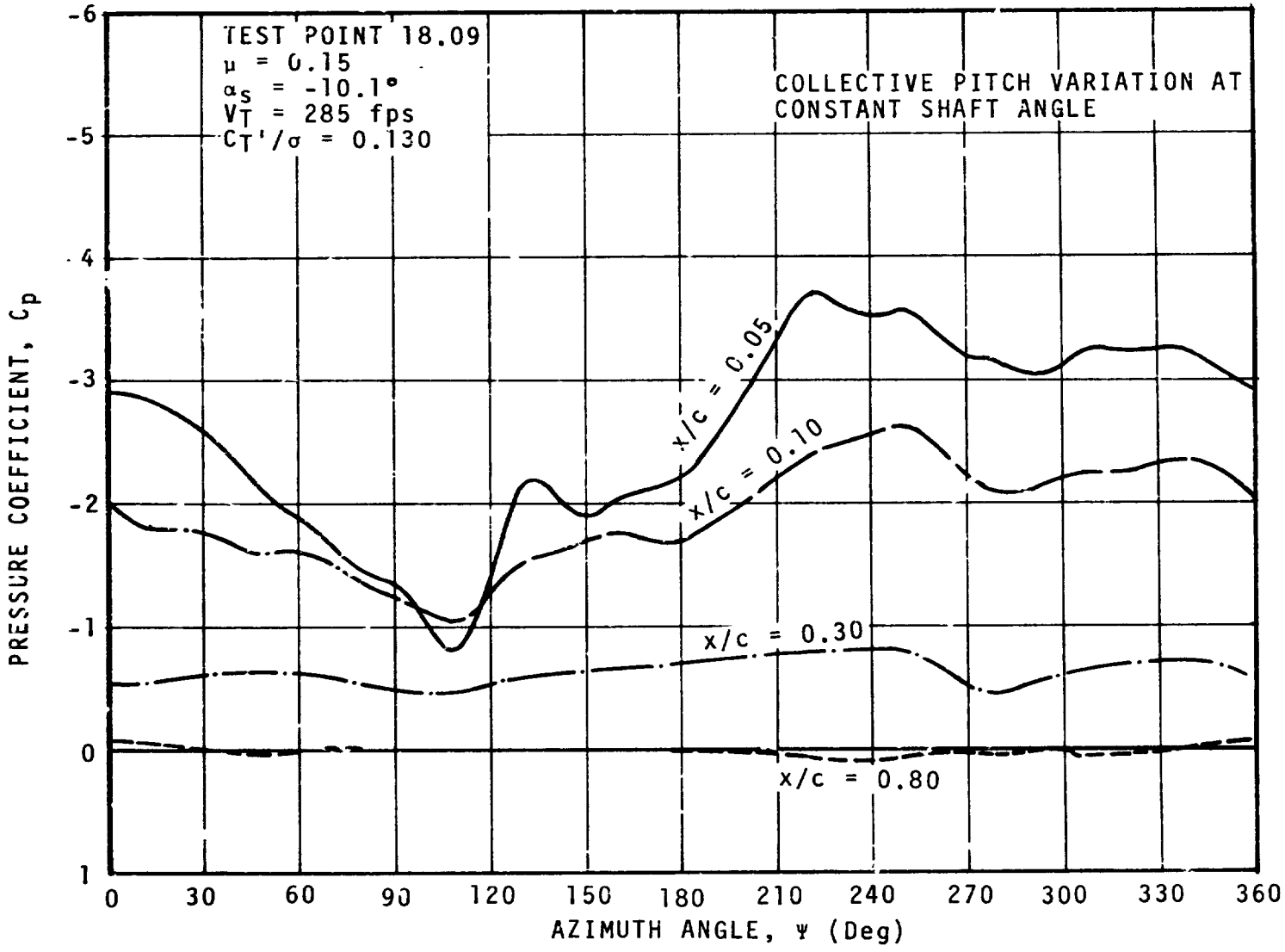

FIGURE 41 TIME HISTORIES OF UPPER SURFACE PRESSURES MEASURED AT r/R = 0.75

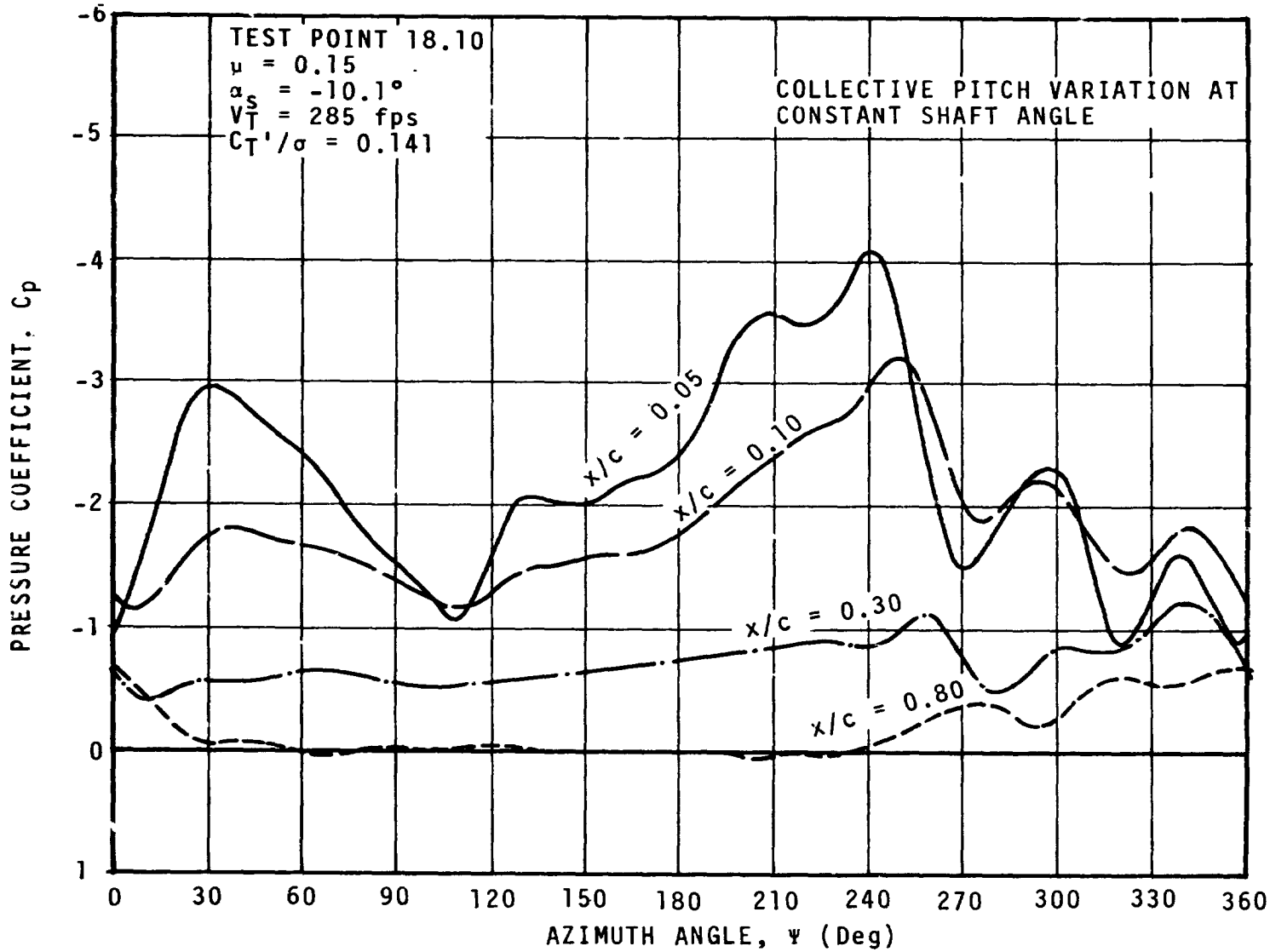

FIGURE 42 TIME HISTORIES OF UPPER SURFACE PRESSURES MEASURED AT r/R = 0.75

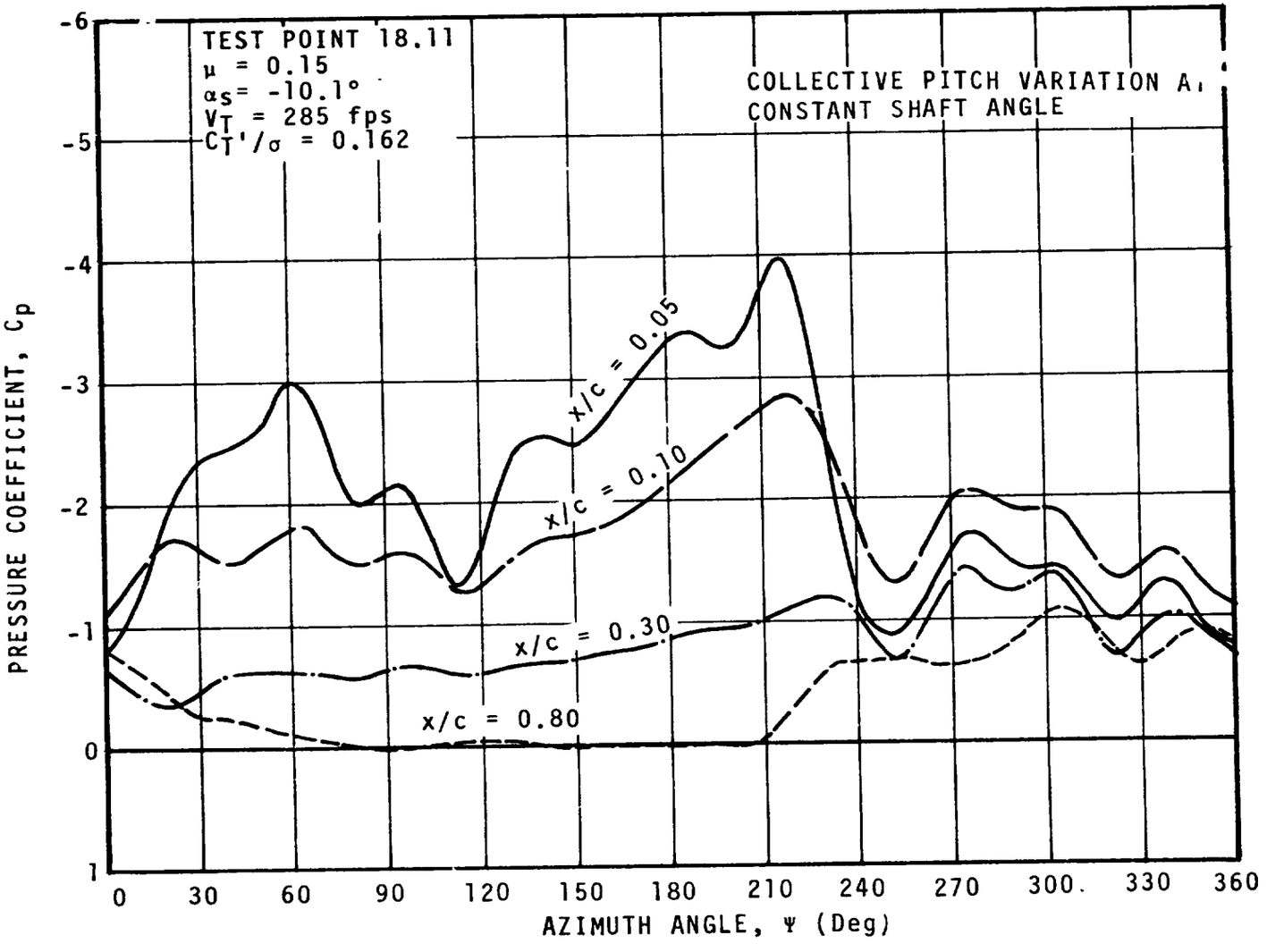

FIGURE 43 TIME HISTORIES OF UPPER SURFACE PRESSURES MEASURED AT r/R = 0.75

3.8 Shaft Angle Variation at Constant Collective Pitch

(Test Points 18.12 to 18.16, $\mu = 0.29$, $V_T = 285$ fps, $\Theta_{.75R} = 9°$)

This was the last run of the test series and at this time more instrumentation was lost.

The performance data is shown in Figure 44 and the measured root flapping angle in Figure 45. The approximate stall boundaries are shown in Figure 46, with little or no correlation with Landgrebe's data, from Reference 6. Time histories for the pressures measured at the 0.10c, 0.30c, and 0.80c stations are shown in Figures 47 through 51. At this time the transducer at the 0.05c station was no longer operating.

The test points taken at the lower thrust levels are of limited interest since they show little indication of stall and no sign of vortex shedding. However, at $C_T'/\sigma = 0.124$ (T.P. 18.15) and at $C_T'/\sigma = 0.140$ (T.P. 18.16) there are signs of secondary vortex shedding at $\alpha > 0$ around $\Psi = 210°$, with the main stall events occurring at $\Psi = 260°$ and $\Psi = 240°$ respectively. There appears to be a third vortex shed after $\Psi = 320°$. Actually, since there is no instrumentation at the 0.05c chord station, all the stall events snould be assumed to occur before they are detected at the .10c chord station.

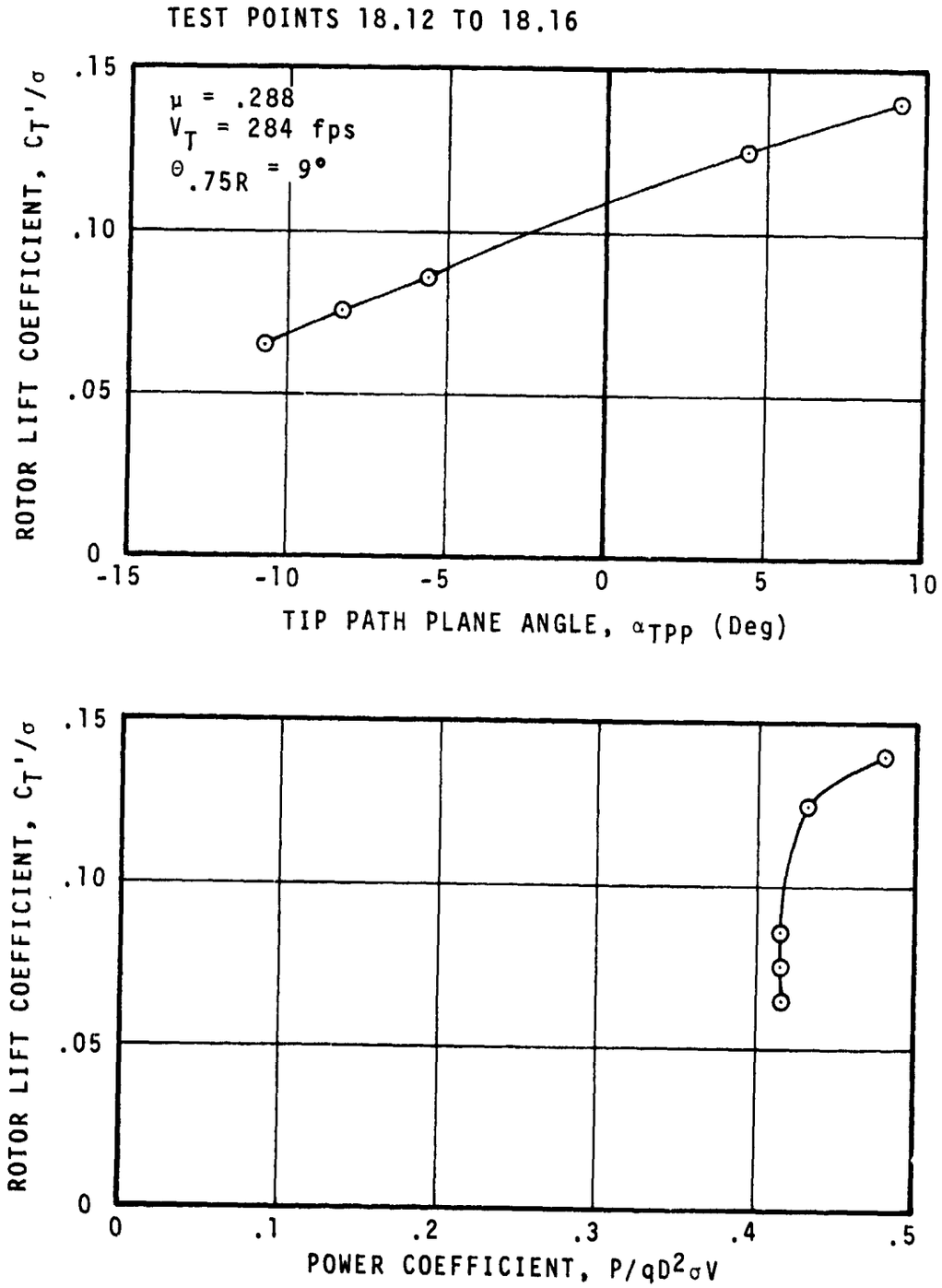

FIGURE 44 MODEL ROTOR PERFORMANCE DATA IN FORWARD FLIGHT. SHAFT ANGLE VARIATION AT CONSTANT COLLECTIVE PITCH.

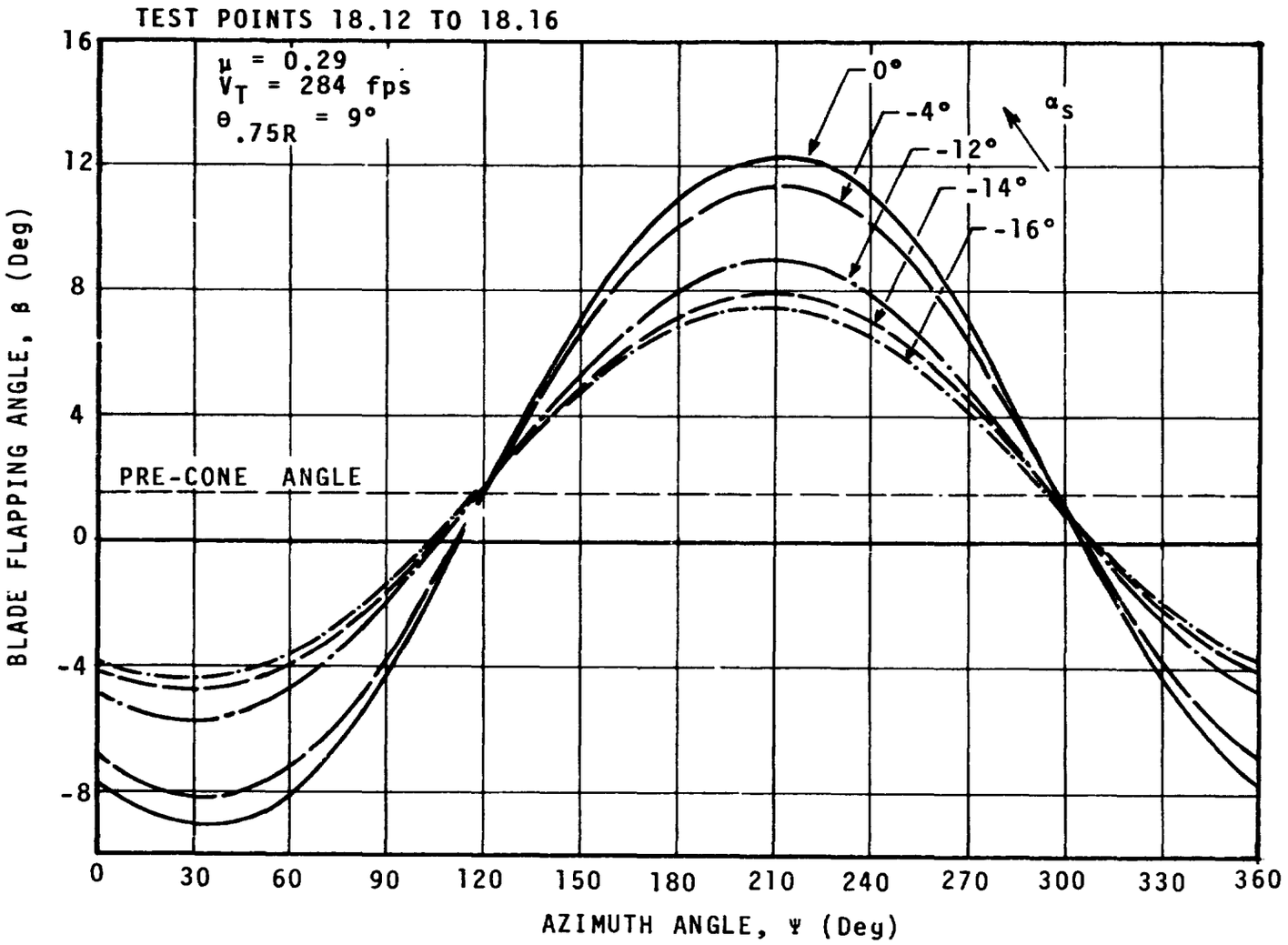

FIGURE 45 MEASURED ROOT FLAPPING ANGLE. SHAFT ANGLE VARIATION AT CONSTANT COLLECTIVE PITCH.

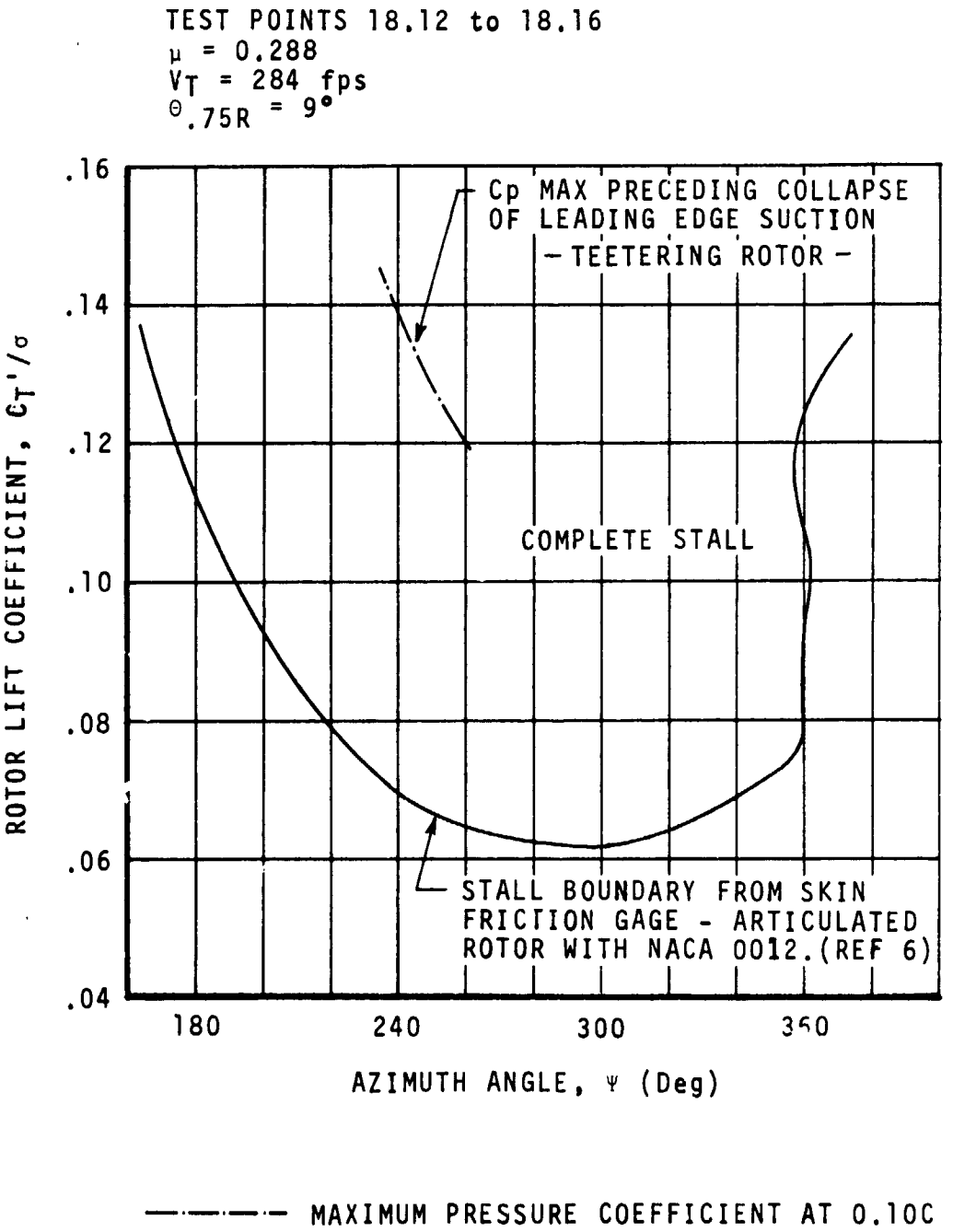

FIGURE 46 SHAFT ANGLE VARIATION AT CONSTANT COLLECTIVE PITCH. APPROXIMATE STALL BOUNDARIES.

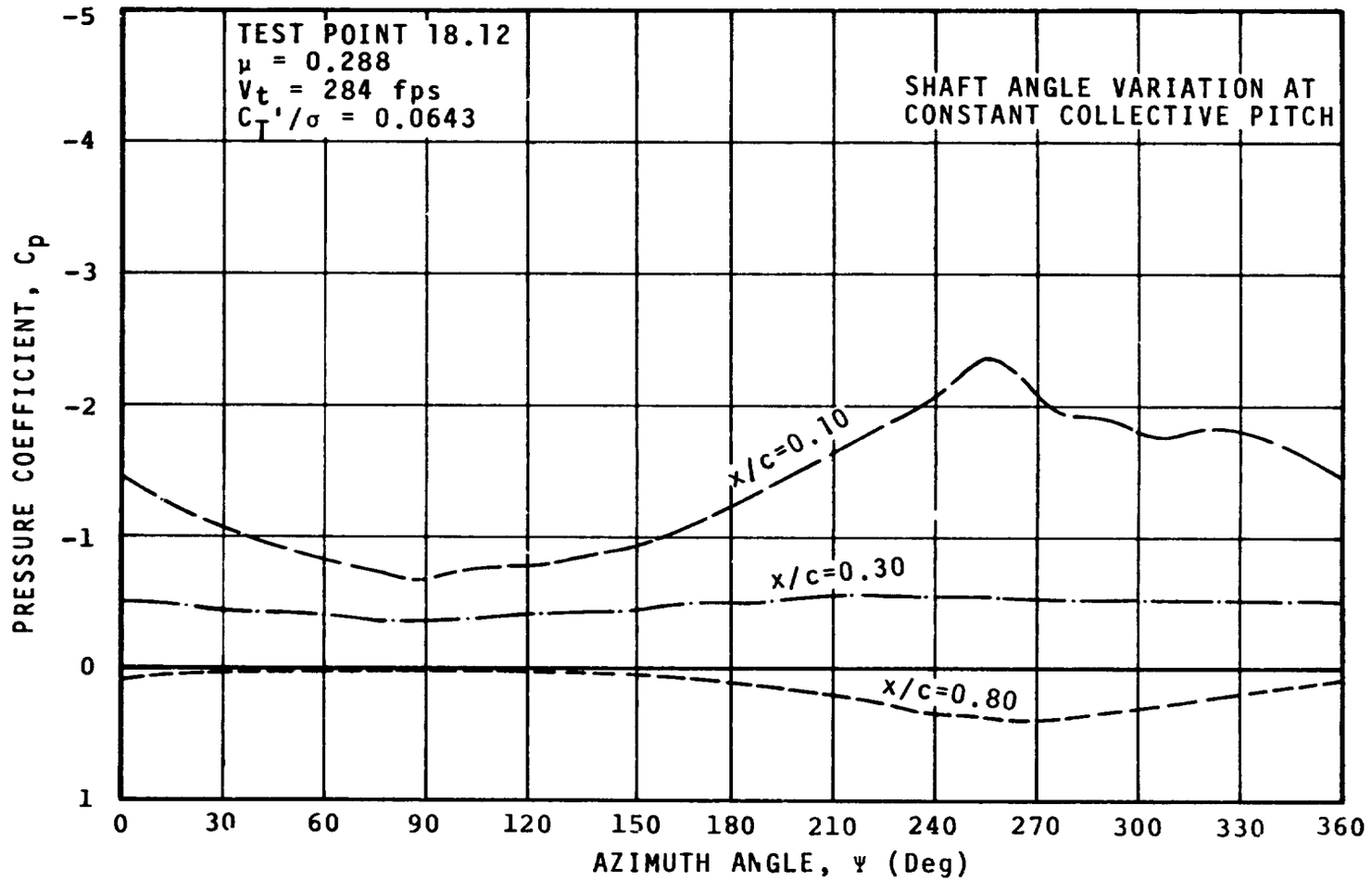

FIGURE 47 TIME HISTORIES OF UPPER SURFACE PRESSURES MEASURED AT r/R=0.75

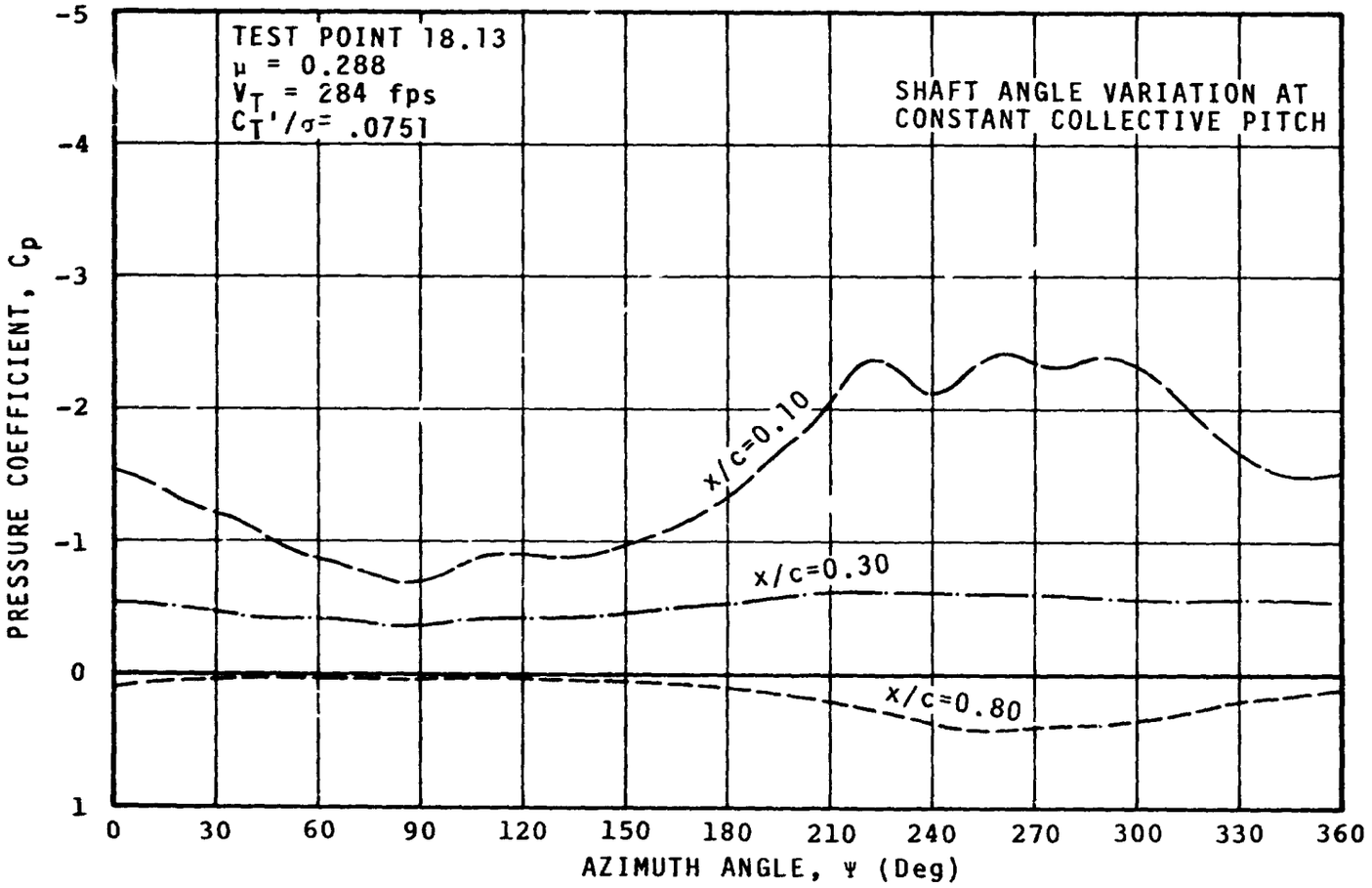

FIGURE 48 TIME HISTORIES OF UPPER SURFACE PRESSURES MEASURED AT r/R=0.75

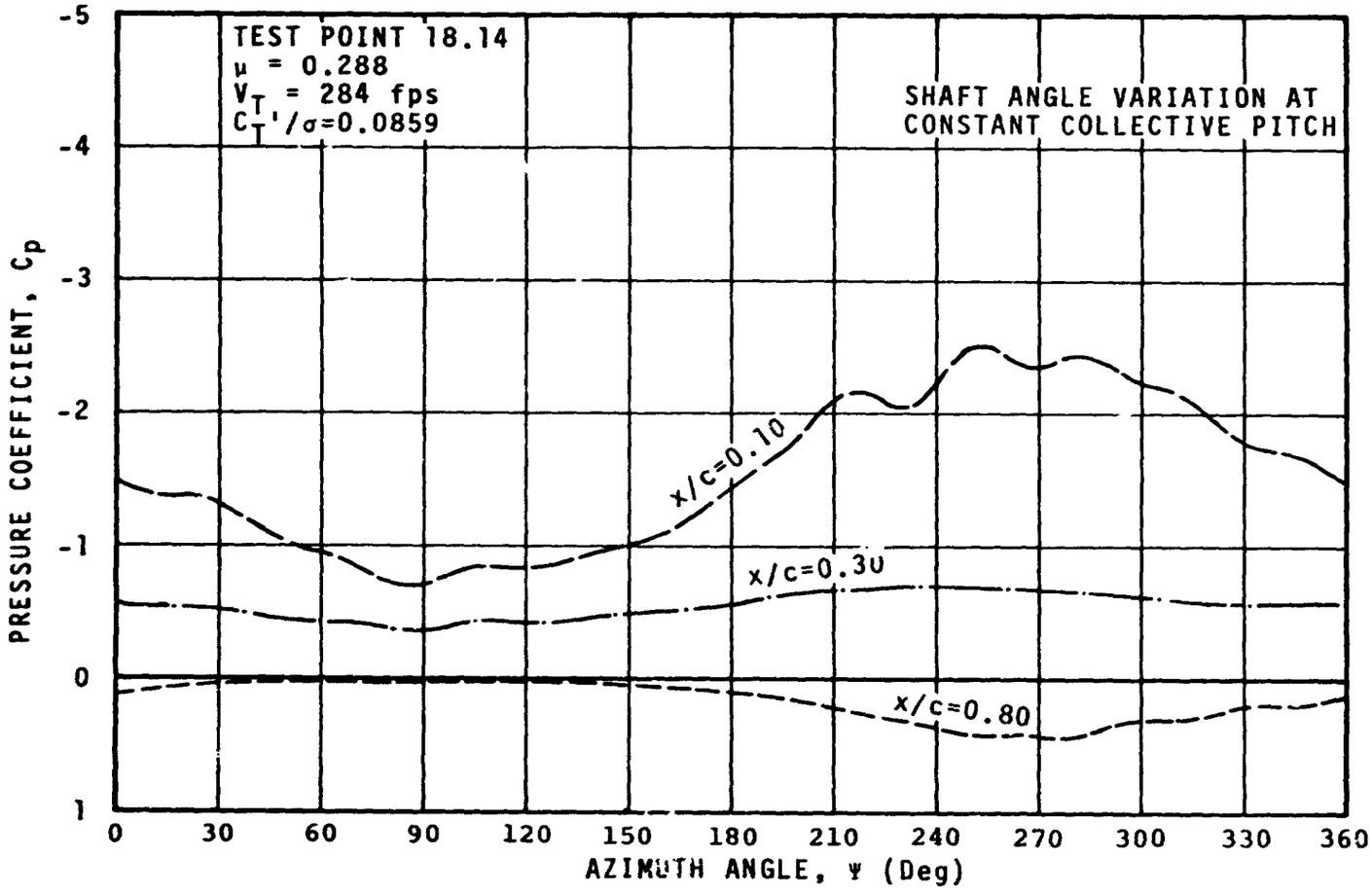

FIGURE 49 TIME HISTORIES OF UPPER SURFACE PRESSURES MEASURED AT r/R=0.75

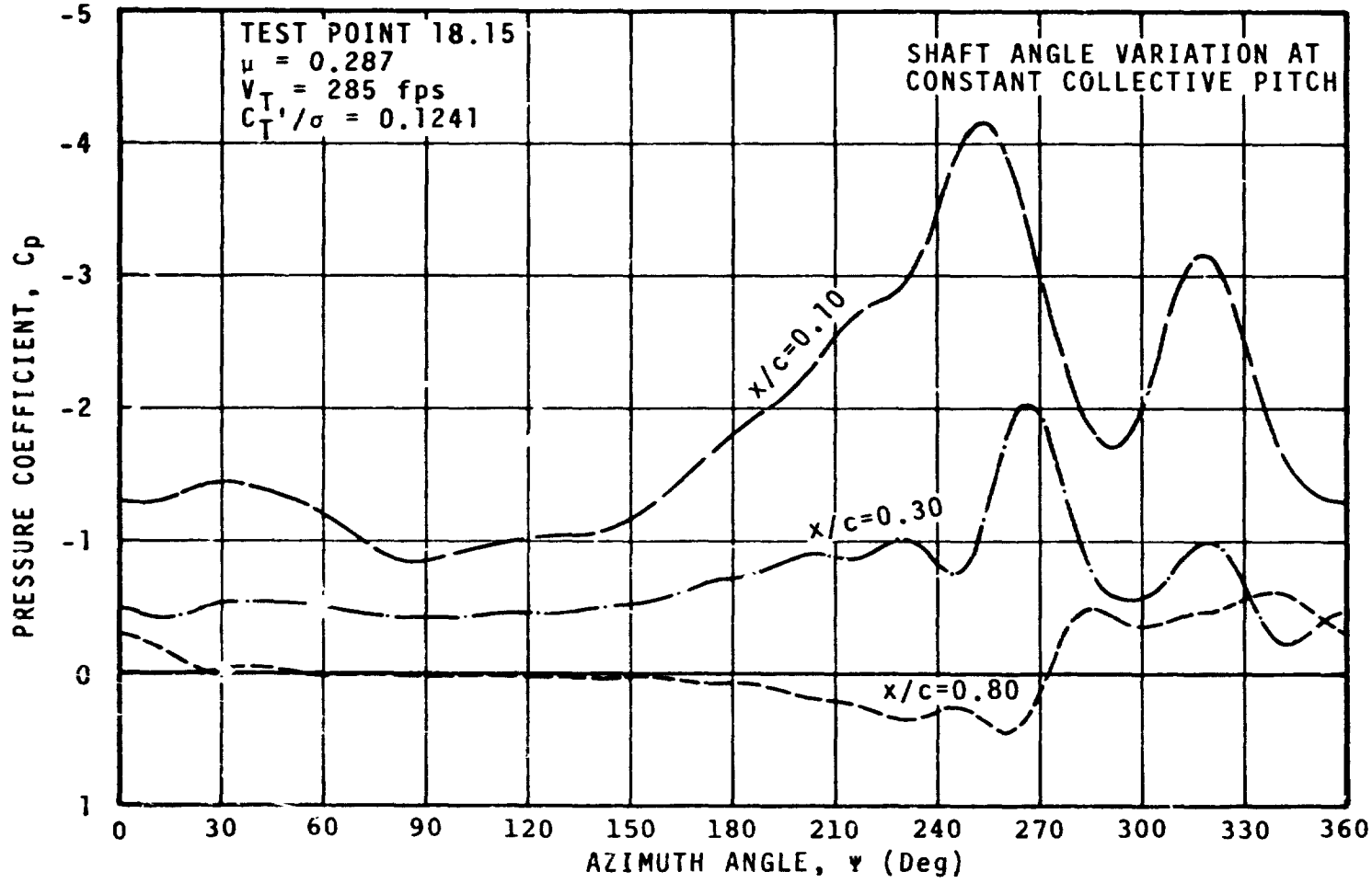

FIGURE 50 TIME HISTORIES OF UPPER SURFACE PRESSURES MEASURED AT r/R=0.75

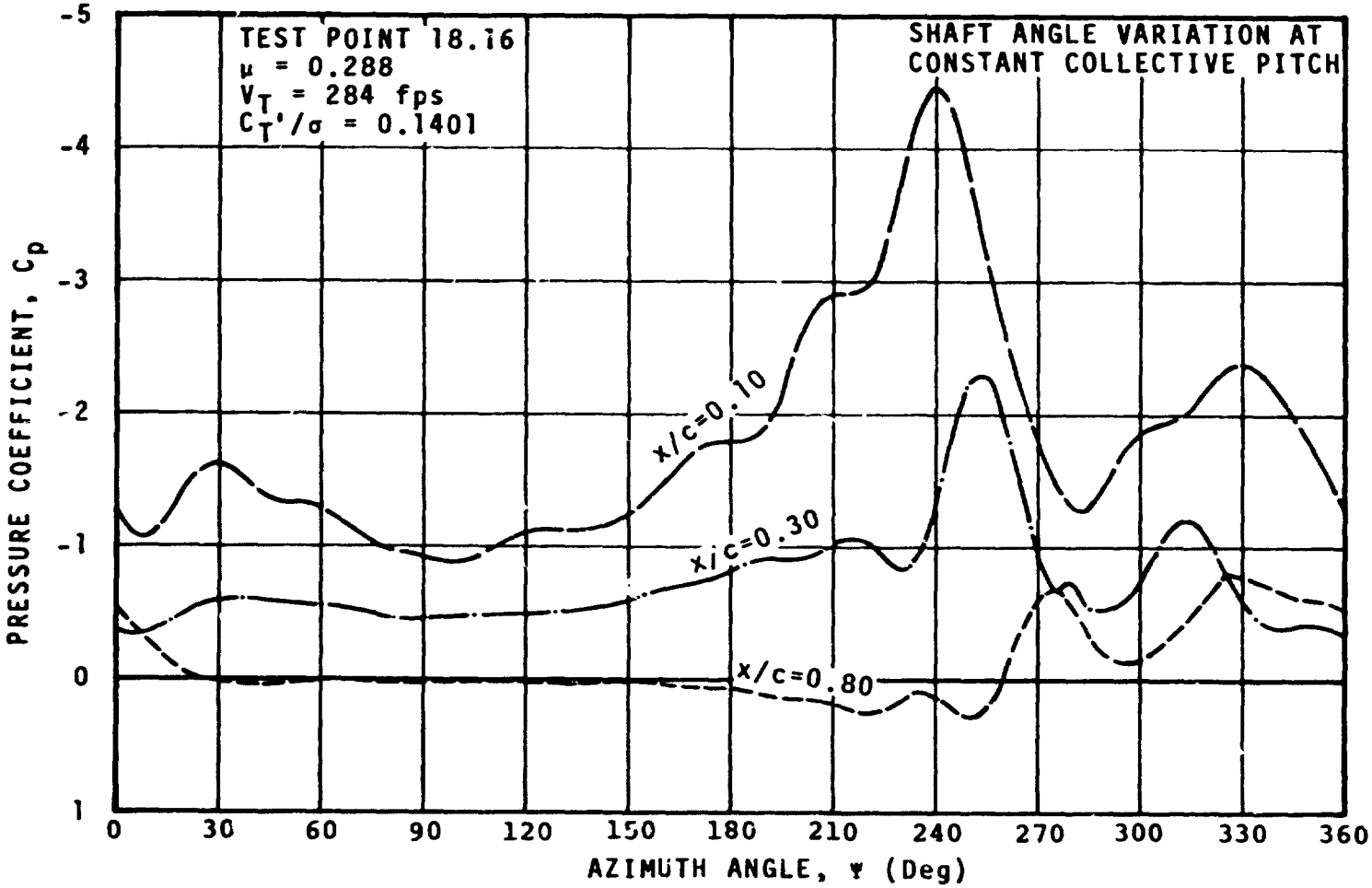

FIGURE 51 TIME HISTORIES OF UPPER SURFACE PRESSURES MEASURED AT r/R=0.75

3.9 Comparison with Theory

A comparison between test and theory was carried out for three test points:

(a) Test Point 17.03, with no stall detected at the 0.75R span station.

(b) Test Point 17.16, with incipient stall.

(c) Test Point 17.15, fully stalled.

Two tools were used for this comparison. The first is a modification of the Boeing Vertol B-67 articulated rotor analysis, B-14. The second is the C-81 analysis, developed by the Bell Helicopter Company.

Flapping and normal force comparisons between theory and test are shown in Figures 52 to 55 for test points 17.03 and 17.16. No data is shown for test point 17.15 because correlation and convergence were very poor. Some of the key performance parameters are compared below.

Test Point 17.03 (μ = 0.336, V_T = 500 fps)

QUANTITY	TEST	B-14	C-81
α_s	-19°	-19°	-18°
$\theta_{.75R}$	12.75°	13.01°	12.57°
α_{TPP}	-12°	-12°	-10°
C_T'/q	0.0675	0.0679	0.0806
$X/qD^2\sigma$	0.188	0.197	0.197

Test Point 17.16 (μ = 0.336, V_T = 500 fps)

QUANTITY	TEST	B-14	C-81
α_s	-11.5°	-11.5°	-11.5°
$\theta_{.75R}$	10.45°	11.72	10.45°
α_{TPP}	-3.02°	-3.16°	-3.20°
C_T'/q	0.0976	0.0995	0.0913
$X/qD^2\sigma$	0.0842	0.1026	0.0782

B-14 Analysis. A modified B-67 isolated rotor analysis, B-14 handles the constraints and flapping balance requirements of the teetering rotor, utilizing a well proven downwash formulation and blade strip analysis. The B-14 analysis does not include the elastic properties of the blade or any unsteady aerodynamic effects.

3.9 Comparison with Theory (Cont'd)

Past experience, as discussed in Reference 2, has indicated that in predicting model rotor performance data full scale sectional characteristics have to be used. The performance data has always been grossly underestimated when model scale sectional characteristics were used. For this reason the computations with the B-14 analysis were carried out with full scale (25 inch chord) sectional data.

As far as the performance data is concerned, the correlation between the B-14 theory and the test data was fairly good for the test points below stall and at incipient stall. The correlation at test conditions in full stall, however, was very poor, as it could be expected since no unsteady aerodynamic effects were taken into account. For test points 17.03 and 17.16 rotor lift, shaft angle, tip path plane angle and propulsive force were matched fairly closely. The amplitude of the flapping angle (at the root) was also matched quite well, and the only discrepancy with the measured flapping was a phase shift of 20° to 30° in azimuth, as shown in Figures 52 and 54, indicating a discrepancy in the side force.

The correlation between measured and calculated normal forces is shown in Figures 53 and 55. Such correlation was poor over the retreating side, and this raises the question of whether the B-14 analysis predicted the correct spanwise loading, or whether the integrated C_N values from the test are actually more in error than by the $\Delta C_N = 0.1$ to 0.2 values postulated in section 3.5. The B-14 analysis does not make use of pitching moment characteristics, and therefore no C_M correlation could be made.

The B-14 analysis also predicted the proximity of a tip vortex at the 0.75R station for $330° < \Psi < 360°$, and in fact the integrated loads for test point 17.16 show an increase in loading at $\Psi > 330°$ which would otherwise be attributed to unsteady aerodynamic effects.

C-81 Analysis. The C-81 program has been developed by the Bell Helicopter Company to predict the performance of complete helicopters. The analysis has been formulated to handle teetering rotors and the program has built-in tables of the sectional characteristics of the NACA 0012 airfoil. The analysis includes an approximation of unsteady aerodynamic effects. Reference 8 contains the programmer's, user's and engineer's manual for the C-81 analysis.

3.9 Comparison with Theory (Cont'd)

Two main obstacles were encountered in using this program to match the wind tunnel data in the present test. The first obstacle is that the program has not been formulated explicitly for isolated rotors, but rather for complete helicopter configurations. Simulating an isolated model rotor required assuming some kind of helicopter configuration and actually trimming this configuration for flight at conditions which would yield the desired rotor performance parameters. The second obstacle was the difficulty in achieving a convergent solution at the reduced load levels of the model rotor. The version of the C-81 program available at Vertol has the convergence criteria adjusted for full scale loads. Only after the study was completed we were advised that the step size for iteration convergence can be input.

Blade flapping angles from the C-81 program are compared to the B-14 estimates and to the measured values in Figures 52 and 54. The two programs predict fairly closely the flapping amplitude, but both display the phase shift already mentioned in discussing the correlation between B-14 and test data. Such phase shift could actually be a wind tunnel effect.

The match in performance data between C-81 and test was not as close as could be achieved with B-14 because of trim and convergence difficulties. As a result rotor lift was overestimated by 16% for test point 17.03 and underestimated by 7% for test point 17.16. The fact that lift was overestimated explains in part why in Figure 53 the normal force level from C-81 is higher than both B-14 and test data (Test Point 17.03). In Figure 55, however, although the overall C_N level is higher than the test data, the C-81 prediction reflects the loss in lift due to retreating blade stall.

C-2

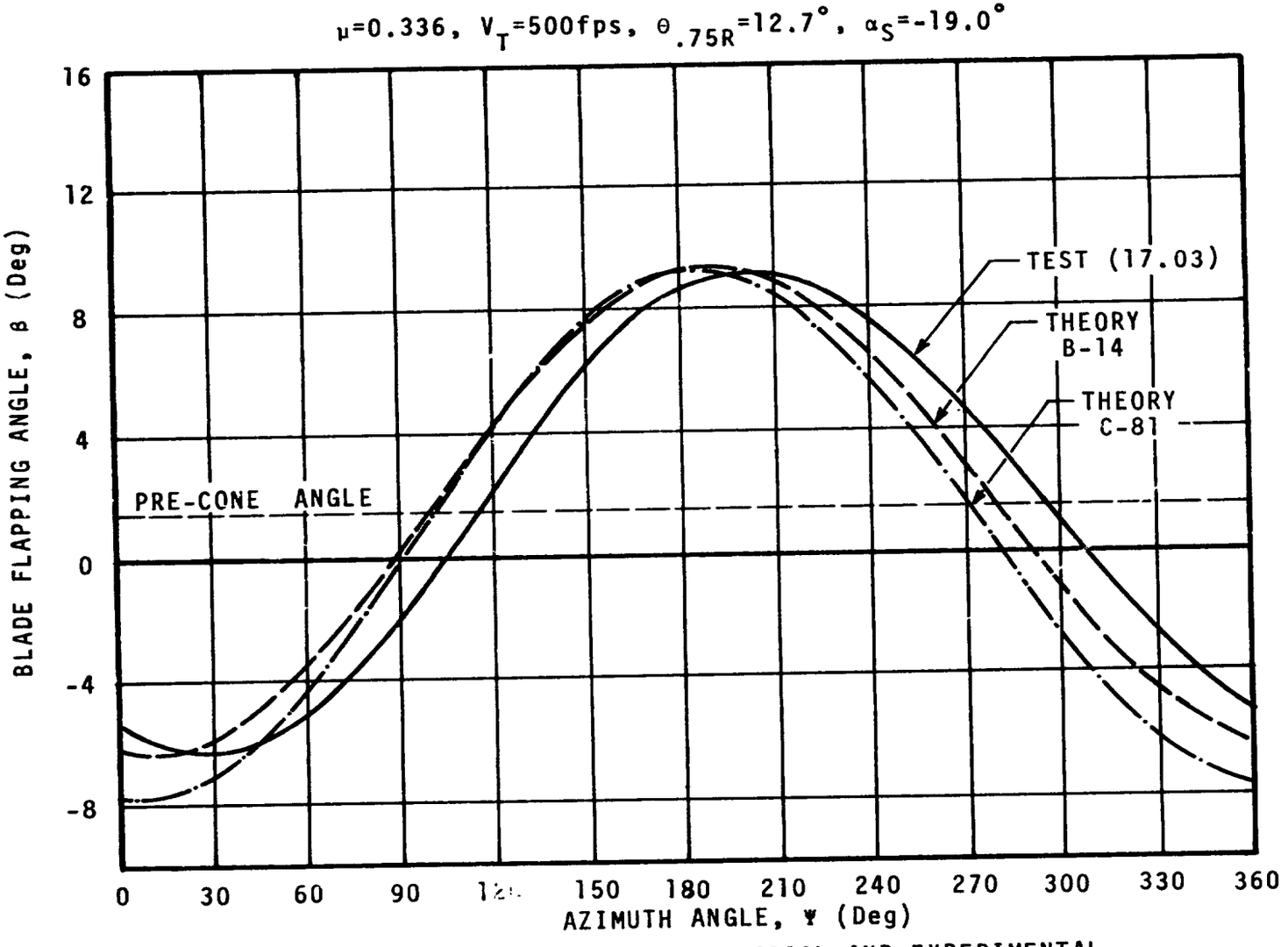

FIGURE 52 CORRELATION OF THEORETICAL AND EXPERIMENTAL BLADE FLAPPING ANGLES

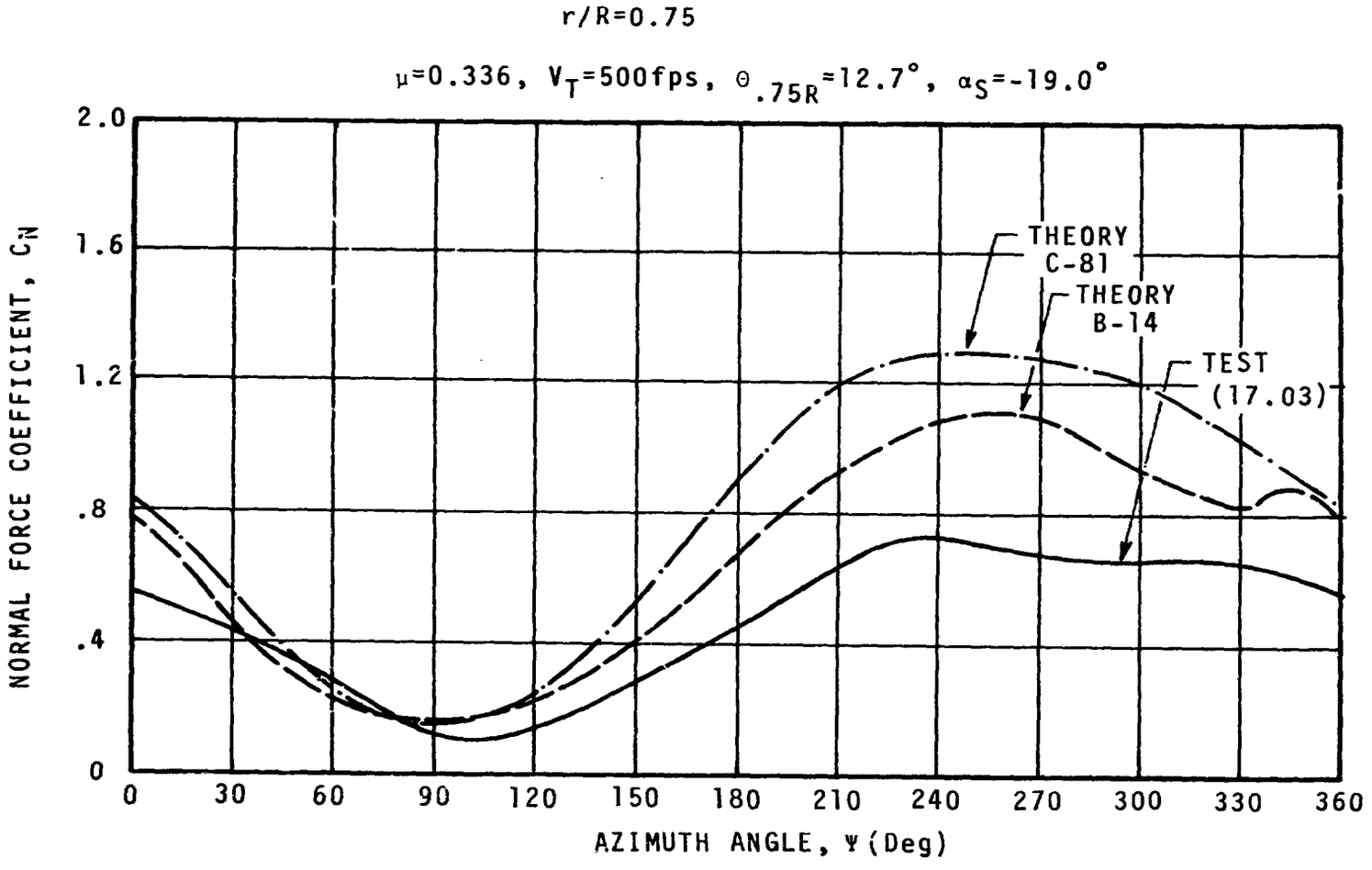

FIGURE 53 CORRELATION OF THEORETICAL AND EXPERIMENTAL NORMAL FORCE COEFFICIENTS

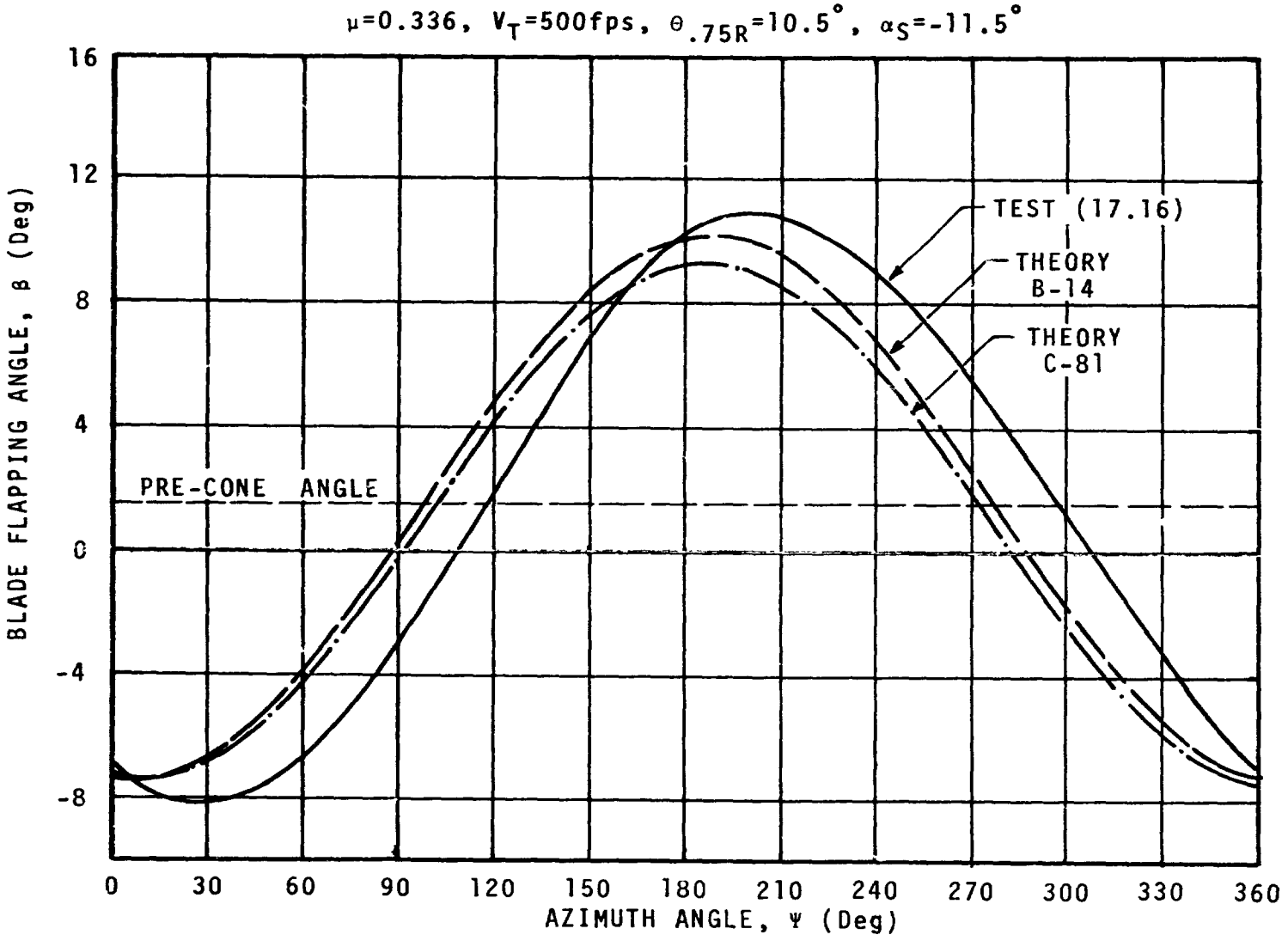

FIGURE 54 CORRELATION OF THEORETICAL AND EXPERIMENTAL BLADE FLAPPING ANGLES

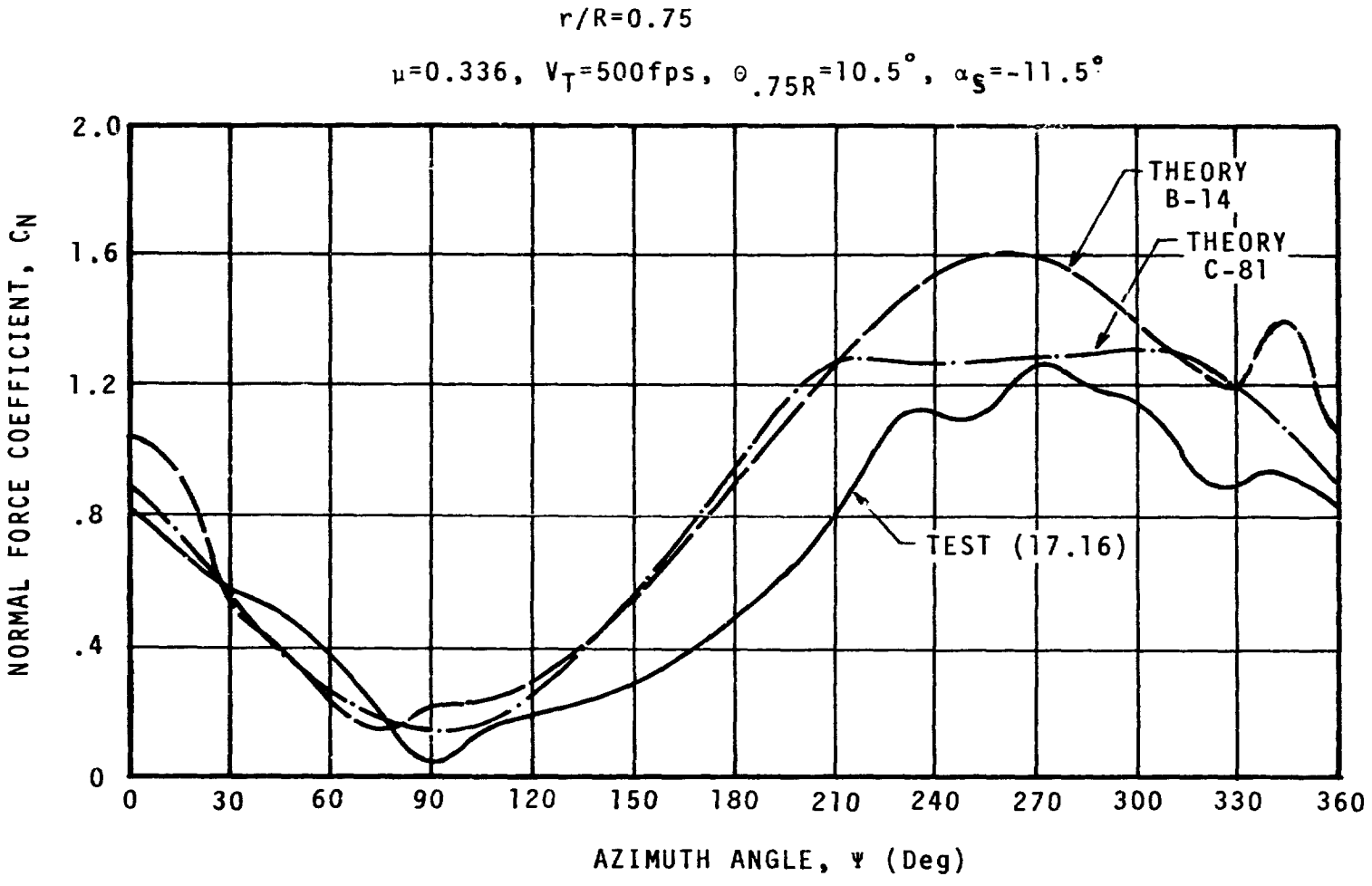

FIGURE 55 CORRELATION OF THEORETICAL AND EXPERIMENTAL NORMAL FORCE COEFFICIENTS

4.0 CONCLUSIONS AND RECOMMENDATIONS

- The present test reconfirmed the fact that the flow over a rotor blade both over the advancing and the retreating side is essentially two-dimensional even in presence of stall.

- This test reconfirmed also that unsteady aerodynamic effects produce fluctuations in the sectional pressure coefficients which are consistent with two-dimensional data obtained in oscillating airfoil tests.

- The pressure coefficients measured over the full scale Bell rotor blade in the NASA-Ames 40 x 80 ft. Wind Tunnel were influenced by transducer acceleration loads and were not in fact responding only to velocity fluctuations in the flow field of the rotor.

- As observed at the 0.75R station, retreating blade stall at low lift levels is characterized by a stall event dominated by a single vortex shed from the leading edge sweeping over the upper surface of the blade. At high lift levels a number of secondary stall events takes place before and after the main stall. Each stall event is associated with a separate shed vortex the influence of which can be followed separately along the upper surface. Up to four separate vortices have been observed.

- At the 0.75R span station, the teetering rotor in this test was subjected to less flow separation than articulated rotors at comparable performance levels.

- The teetering rotor compared to the articulated rotor was subjected to smaller excursions in angle of attack, which resulted in smaller load excursions.

- The sequence of stall events observed on the articulated rotor in Reference 2 seems to hold true for the teetering rotor as well.

- In estimating chordwise pressure distributions the pressure differential across the aft portion of the blade section is more important than the individual absolute pressures on each surface.

- Surface pressure measurements give a good indication of stall, but are not as effective as skin friction gages in detecting flow reattachment.

4.0 Conclusions and Recommendations (Cont'd)

- The transducer mounting system seems to be acceptable, but the measurement of absolute pressure distributions with blade mounted transducers remains to be done with completely satisfactory results.

- A considerable amount of work is still necessary to understand the role of Reynolds Numbers on unsteady aerodynamic effects.

- Additional testing will be necessary to determine stall effects in conjunction with the degradation in propulsive force both as a function of lift and advance ratio.

- A systematic investigation of tip vortex effects will be necessary to separate vortex intersection effects from pure unsteady aerodynamic effects.

- Because of the instrumentation problems encountered during the present test the conditions for which integrated data could not be obtained should be repeated.

5.0 APPENDIX

DATA REDUCTION PROGRAM Y-54

Y-54 is a computer program developed to reduce data obtained during tests involving the measurement of pressures over rotor blades. Data from pressure transducers, blade motion sensors, and blade loads gages are input to the program in harmonic coefficient form, along with data characterizing the rotor flight condition. These data are then operated on to provide time histories of the rotor blade environment, including: calculation of the blade element velocities, pressure coefficients, angle of attack, blade position, and blade motion. The integration of the pressure data utilizes a trapezoidal technique.

Computation

The following calculations are made based on the harmonic input data and the test run condition data. To simplify presentation of these computations, the following ground rules shall be used:

At any given test point, each piece of data can be represented by a series of harmonic coefficients.

Let the steady term of the harmonic series be associated with a subscript (o).

Let the remaining (i) terms of the sin (s) and cos (c) coefficients of the harmonic series have the (ic) and (is) subscripts.

Therefore, the test data can be characterized by the data harmonic coefficients,

$$d = d_o + \sum_{i=1}^{12} (d_{is} \sin i\psi + d_{ic} \cos i\psi)$$

Let each data type be represented by an identification symbol.

Root Flapping Angle	$= \beta$
Pressure	$= P_k$
Pitch Link Load	$= PLL$

k = subscript designating a particular x/c and y/c transducer location. k = 1 to 20

APPENDIX (Cont'd)

Additional data defining test conditions required in the calculations are input to the program along with the harmonic coefficients.

I. Flapping Deflection and Motion Normal to Disc Plane

$$\beta = \beta_0 + \sum_{i=1}^{n} (\beta_{is} \sin i\psi + \beta_{ic} \cos i\psi) \sim \text{Degrees}$$

$$\dot{\beta} = \frac{\pi}{180} \sum_{i=1}^{n} \Omega i \, (\beta_{is} \cos i\psi - \beta_{ic} \sin i\psi) \sim \text{Radians/Sec}$$

$$\ddot{\beta} = \frac{\pi}{180} \sum_{i=1}^{n} (\Omega i)^2 (-\beta_{is} \sin i\psi - \beta_{ic} \cos i\psi) \sim \text{Radians/Sec}^2$$

II. Pitch Link Loads

$$PLL = PLL_0 + \sum_{i=1}^{n} (PLL_{is} \sin i\psi + PLL_{ic} \cos i\psi)$$

III. Determination of Three-Quarter Radius Velocities and Mach No.

$$U_p = \Omega R \lambda_s - .75R\dot{\beta} - V_\infty (\cos\alpha_s)(\tfrac{\pi}{180}\beta)(\cos\psi) \sim \text{Ft./Sec.}$$

$$U_T = .75\Omega R + V_\infty (\sin\psi)(\cos\alpha_s) \sim \text{Feet/Sec.}$$

$$V_{LOC} = [U_p^2 + U_T^2]^{1/2} \sim \text{Feet/Sec.}$$

$$M^{\#} = V_{LOC}/a$$

$$\dot{U}_p = -.75R\ddot{\beta} - V_\infty (\cos\alpha_s)(\dot{\beta})(\cos\psi) + V_\infty (\cos\alpha_s)(\tfrac{\pi}{180}\beta)(\Omega)(\sin\psi) \sim \text{Feet/Sec.}$$

$$\dot{U}_T = \Omega (V_\infty)(\cos\psi)(\cos\alpha_s) \sim \text{Feet/Sec}^2$$

$$R_C^{\#} = \frac{\rho V_{LOC} C}{[340.8 + .584((\frac{\theta}{459.7})^2 - 459.6)] \times 10^{-9}}$$

IV. Determination of Reduced Frequency

$$K_1 = \frac{c\Omega}{2V_{LOC}}$$

V. Determination of Pressures

$$PTO1 = P_{o1_o} + \sum_{i=1}^{n} (P_{o1_{is}} \sin i\Psi + P_{o1_{ic}} \cos i\Psi) \quad \sim PSI.$$

$$PTO2 = P_{o2_o} + \sum_{i=1}^{n} (P_{o2_{is}} \sin i\Psi + P_{o2_{ic}} \cos i\Psi) \quad \sim PSI.$$

•

•

•

$$PT19 = P_{19_o} + \sum_{i=1}^{n} (P_{19_{is}} \sin i\Psi + P_{19_{ic}} \cos i\Psi) \quad \sim PSI.$$

VI. Determination of Pressure Coefficients

$$CP_K = (PT_K) \frac{1}{(\frac{1}{288})\rho V_{LOC}^2} \qquad K = 1, 20$$

VII. Determination of Angle of Attack

Calculated:

$$\alpha_{CALC} = \theta + TAN^{-1}(U_P/U_T)$$

$$\alpha_{m_2} = \frac{C_N - C_{N_o}}{(dC_N/d\alpha)_o}$$

$$C_{N_o} = C_N \text{ @ } \alpha = 0^\circ, \quad (dC_N/d\alpha)_o = \left.\frac{dC_N}{d\alpha}\right|_{\alpha=0^\circ}$$

Trapezoidal Integration

For the trapezoidal integration technique, the airfoil is divided into various regions.

a. For calculation of normal force and associated moments

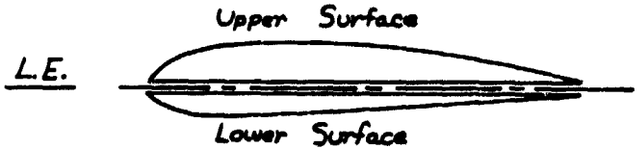

b. For calculation of chord force and associated moments

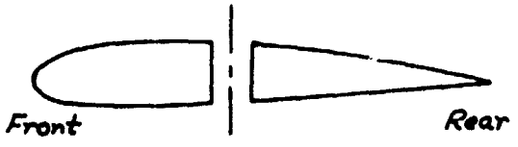

The integration takes place where data is reconstituted and uses the pressure coefficients of each transducer.

When the engineering approximation for missing data on the aft of the airfoil is utilized, the program makes a series of pressure coefficients as follows:

Program Instructions for Including Engineering Approximation

Make following pressure coefficients at the following (x/c, y/c) coordinates:

y/c	x/c	
-.0623	.3	Lower Surface
-.0554	.5	
-.0482	.6	
-.03925	.7	
-.0232	.85	
-.0107	.95	
.004	1.0	

$$C_{p_{y/c}} = C_{p_{x/c_{LOWER}}} = .30\sqrt{\frac{1-x/c}{.70}}$$

y/c	x/c	
.004	1.0	Upper Surface
.0107	.95	
.0232	.85	
.0288	.80	

$$C_{P_{y/c}} = C_{P_{x/c_{UPPER}}} = .80\sqrt{\frac{1-x/c}{.20}}$$

Include these pressure coefficients in the set for integration when the engineering approximation option is called.

Program Instructions for Doing Trapezoidal Integration

I. Upper Surface Program Instructions

(1) Sort transducers in ascending x/c order (y/c > 0): Include transducer at x/c = 0 made from the differential pressure at x/c = 0.05.

(2) Integrate (Cp) on upper surface from x/c = 0 to last available transducer.

(3) Integrate [(Cp)(x/c)] on the upper surface to get moment due to upper surface.

II. Lower Surface Program Instructions

(1) Sort transducers in ascending x/c order (y/c < 0): Include transducer at x/c = 0 made from differential pressure.

(2) Integrate (Cp) on lower surface from x/c = 0 to last available transducer.

(3) Integrate [(Cp)(x/c)] on the lower surface to get moment due to lower surface.

III. Front Surface Program Instructions

(1) Sort transducer into ascending order of y/c from (y/c < 0) to (y/c > 0) for x/c ≠ Card input #0012.

(2) Integrate (Cp) on front surface from -y/c to +y/c over all transducers.

(3) Integrate $[(Cp)(y/c)]$ on the front surface to get moment due to the front surface.

IV. Rear Surface Program Instructions

(1) Sort transducers into ascending order of y/c from (y/c < 0) to (y/c > 0) for x/c ≥ Card input #0012.

(2) Integrate (Cp) on rear surface from -y/c to +y/c over all transducers.

(3) Integrate $[(Cp)(y/c)]$ on rear surface to get moment due to rear surface.

Normal Force Coefficient Calculation

Subtract upper surface integrated pressure coefficients from lower surface integrated pressure coefficients.

$$C_N = C_{N_{LOWER}} - C_{N_{UPPER}}$$

Chord Force Coefficient Calculation

Subtract right hand surface integrated pressure coefficients from left hand surface integrated pressure coefficients.

$$C_C = C_{C_{FRONT}} - C_{C_{BACK}}$$

Moments About Leading Edge (Nose up +)

Subtract bottom surface integrated moment $\int C_p (x/c)\, d(x/c)$ coefficients from upper surface integrated moment coefficients.

Add the above to the difference between the right hand integrated moment from the left hand surface integrated moment.

$$C_{m_{L.E.}} = (C_{m_{L.E._{UPPER}}} - C_{m_{L.E._{LOWER}}}) + (C_{m_{L.E._{FRONT}}} - C_{m_{L.E._{BACK}}})$$

TABLE IV SUMMARY OF REDUCED DATA

TEST POINT	μ	V_T (fps)	α_{SHAFT}	$\theta_{.75R}$	C_T'/σ	$P/qD^2\sigma V$	$\overline{X}$	α_{TPP}
14.03	.195	284	-0.5°	3.13°	.0469		-.0649	0.7°
04	.194	286	0°	11.08°	.1377		-.4247	5.5°
06	.405	283	-0.3°	3.03°	.0570		-.0290	3.5°
07	.381	287	-0.3°	3.03°	.0546		-.0288	2.8°
08	.384	288	-0.3°	8.15°	.1234		-.1499	9.1°
11	.188	285	-0.5°	3.13°	.0519		-.0687	1.1°
13	.189	284	0°	11.29°	.1396		-.4371	5.6°
17.03	.336	500	-19°	12.75°	.0675	.18155	.1879	-11.69°
04	.335	500	-16°	12.85°	.0878	.19307	.1548	-7.7°
05	.337	499	-13°	12.80°	.1023	.21629	.1146	-3.96°
06	.336	500	-11°	12.75°	.1119	.23698	.0762	-1.263°
07	.337	499	-8°	12.75°	.1278	.25181	.0007	2.97°
08	.336	499	-8°	9.93°	.0977		.0128	-.21°
09	.335	501	-6°	10.03°	.1084		-.0390	2.4°
15	.335	501	-4°	8.78°	.1225	.1778	-.0986	5.8°
16	.336	498	-11.5°	10.45°	.0976	.18033	.0842	-3.1°
17	.335	501	-19°	12.44°	.0755	.18033	.2015	-11.3°
18	.335	500	-13°	9.51°	.0747	.15167	.1068	-6.25°
19	.335	500	-6°	3.03°	.0750	.09579	-.0134	-.65°
20	.336	499	0°	3.13°	.0757	.05637	-.1224	4.6°
18.04	.332	500	-11.5°	10.45°	.0977	.17774	.0812	-3.1°
05	.335	499	-13°	9.51°	.0754	.14932	.0981	-6.4°
06	.336	498	-6°	6.16°	.0760	.09776	-.0165	-.4°
07	.143	284	-10.1°	8.99°	.1014	3.0777	.8631	-7.0°
08	.143	284	-10.1°	9.93°	.1116	3.4083	.8793	-6.25°
09	.143	286	-10.1°	12.02°	.1301	4.6762	.989	-5.1°
10	.143	285	-10.1°	15.05°	.1407	6.0468	1.193	-4.07°
11	.143	284	-10.1°	21.00°	.1625	9.6037	1.235	-1.6°
12	.288	284	-16°	8.99°	.0643	.41679	.1985	-10.7°
13	.288	284	-14°	9.09°	.0751	.41633	.1745	-8.3°
14	.288	284	-12°	9.09°	.0859	.41596	.1334	-5.6°
15	.287	285	-4°	8.99°	.1241	.43216	-.1078	4.4°
16	.288	284	0°	8.99°	.1401	.4804	-.3201	9.2°

APPENDIX

TABLE V CONDITIONS FROM TEST BVWT 054, RUN 28

TEST POINT	μ	V_T (fps)	αSHAFT (DEG)	$\Theta_{.75R}$	C_T'/σ	$\frac{P}{qD^2\sigma V}$	$\bar{X}$	α_{TPP} (DEG)
3	0.35	500	-25.53	13.48	.010	.107	.034	-24.43
4	↓	↓	-23.66	13.48	.018	.157	.072	-22.16
5	↓	↓	-19.16	13.48	.044	.243	.145	-16.46
6	↓	↓	-16.18	13.49	.065	.275	.164	-12.68
7	↓	↓	-14.93	13.48	.073	.281	.159	-11.13
8	↓	↓	-10.96	13.49	.096	.283	.117	-5.76
9	↓	↓	-9.02	13.49	.105	.288	.083	-3.22
10	↓	↓	-6.95	13.49	.115	.294	.033	-0.35
11	↓	↓	-4.95	13.50	.124	.294	-.028	2.35
12	↓	↓	-2.97	13.50	.133	.296	-.104	4.90

6. References

1. Gray, L., and Liiva, J., Two-Dimensional Tests of Airfoils Oscillating Near Stall, USAAVLABS TR 68-13, 1968.

2. Fisher, R. K., Thompkins, J. E., Bobo, C. J., Child, R. F., An Experimental Investigation of the Helicopter Rotor Blade Element Airloads on a Model Rotor in the Blade Stall Regime, NASA CR-114424, September, 1971.

3. Bowden, T. H., Shockey, G. A., A Wind Tunnel Investigation of the Aerodynamic Environment of a Full-Scale Helicopter Rotor In Forward Flight, USAAVLABS TR 70-35, July, 1970.

4. Gessow, A., and Myers, G. C., Aerodynamics of the Helicopter, Frederick Ungar Publishing Co., New York, 1952.

5. Martin, J. M., Empey, R. W., McCroskey, W. J., and Caradonna, F. X., A Detailed Experimental Analysis of Dynamic Stall on an Unsteady Two-Dimensional Airfoil.

6. Landgrebe, A. J., Bellinger, E. D., A Systematic Study of Helicopter Rotor Stall Using Model Rotors, Presented at the 30th Annual National Forum of the American Helicopter Society in Washington, D. C., May, 1974, Preprint No. 804.

7. B. Van den Berg, Reynolds Number and Mach Number Effects on the Maximum Lift and the Stalling Characteristics of Wings at Low Speeds, NLR TR 69025U, March, 1969.

8. Bird, B. J. McLarty, T. Bennett, R. L., Rotorcraft Flight Simulation with Aeroelastic Representation, Bell Helicopter Company, Fort Worth, Texas, Report No. 299-099-595.

9. Bowden, T. H., Blankenship, B. L., Test-Theory Correlations of Aerodynamic Data of a Full-Scale Helicopter Rotor in Forward Flight, Bell Helicopter Company, Fort Worth, Texas, Report No. 576-099-056, January, 1972.